Manuscript Details

Manuscript number	EARTH_2018_481
Title	Intraplate magmatism at a convergent plate boundary, the case of the Cenozoic northern Adria magmatism
Article type	Review Article

Abstract

The complex European–Adria geodynamic framework, which led to the formation of the Alpine belt, is considered responsible for the orogenic magmatism that occurred in the Central Alps along the Periadriatic/Insubric Line (late Eocene–early Oligocene) and the anorogenic magmatism that occurred in the Southeastern Alps (late Paleocene–early Miocene). While subduction–related magmatic activities are expected near convergent margins, the presence of the intraplate–related magmatic products is still puzzling. Therefore, in this work new geochemical and geochronological data of magmatic products from the Veneto Volcanic Province (VVP, north–east Italy) are provided in order to constrain the Cenozoic intraplate magmatism of the Southeastern Alps. The VVP is formed by dominant basic–ultrabasic (from nephelinites to tholeiites) magmatic products and by localized acid (latitic, trachytic, and rhyolitic) volcanic and sub–volcanic bodies. Trace element patterns and ratios suggest that the mantle source of the basanitic magma types was a phlogopite–bearing garnet lherzolite, while those of the tholeiitic magma types was an anhydrous (i.e., without residual phlogopite and amphibole) garnet lherzolite. All the basic–ultrabasic VVP magmatic products exhibit enrichments in Ba, Sr, and P, indicating the mantle sources could be metasomatized by carbonatitic melts. According to the biostratigraphic records and our new 40Ar/39Ar ages, VVP eruptions occurred in several pulses, reflecting the extensional phases experienced by the Eastern Alpine domain. The volcanism started in the late Paleocene in the western sector of the VVP where activity was widespread also during the Eocene (45.21± 0.11 Ma – 38.73 ± 0.44 Ma). In the eastern sector eruptions took place only in the early Oligocene (32.35 ± 0.09 Ma – 32.09 ± 0.29 Ma) and in the early Miocene (~ 22 – 23 Ma). Previously, as suggested for neighboring orogenic magmatism, also the anorogenic magmatic activities were interpreted as resulting from mantle upwellings through slab window(s) following the European slab break–off occurred ~ 35 Ma. However, considering i) new tomographic images evidencing a continuous subvertical slab beneath the Central Alps, and ii) the onset of magmatic activity in the VVP in the late Paleocene (i.e., before the slab break–off) and its continuation until Miocene, we propose an alternative geodynamic scenario to explain the anorogenic magmatism. The westward rollback of the European slab caused the retreat and steepening of the sinking plate. As a consequence, the sub–slab mantle material escaped and upwelled from the front of the slab and created a poloidal mantle flow. The latter induced the breakdown of carbonates in calcareous metasediments and carbonated metabasics within the subducting oceanic slab, providing carbonatitic melts, which could be responsible for the metasomatism of the VVP mantle sources. After that, the poloidal mantle flow also induced i) the extensional deformation in the overriding Adria microplate and ii) the decompressional melting of VVP mantle sources, iii) triggering the magmatism with intraplate affinity. During these processes, the Adria microplate also rotated counterclockwise, allowing the poloidal mantle flow to affect different portions of the overlying lithosphere and generating up to five eruptive centers within the VVP.

Keywords	Intraplate magmatism; 40Ar/39Ar geochronology; Poloidal mantle flow; Southeastern Alps; Veneto Volcanic Province

Corresponding Author	Costanza Bonadiman
Corresponding Author's Institution	University of Ferrara, Department of Physics and Earth Sciences
Order of Authors	Valentina Brombin, Costanza Bonadiman, Fred Jourdan, Guido Roghi, Massimo Coltorti, Laura E. Webb, Sara Callegaro, Giuliano Bellieni, Giampaolo De Vecchi, Roberto Sedea, Andrea Marzoli
Suggested reviewers	Gilles Chazot, Marco Brenna, Maurizio Mazzucchelli, Alberto Zanetti

Submission Files Included in this PDF

File Name [File Type]

Brombin et al-cover letter.docx [Cover Letter]

Brombin et al. _ abstract.docx [Abstract]

Brombin et al-manuscript.docx [Manuscript File]

Fig. 01.jpg [Figure]

Fig. 02.jpg [Figure]

Fig. 03.jpg [Figure]

Fig. 04.jpg [Figure]

Fig. 05a.jpg [Figure]

Fig. 05b.jpg [Figure]

Fig. 06.jpg [Figure]

Fig. 07.jpg [Figure]

Fig. 08.jpg [Figure]

Fig. 09.jpg [Figure]

Fig. 10.jpg [Figure]

Brombin_On-line Supplementary material.docx [Supporting File]

To view all the submission files, including those not included in the PDF, click on the manuscript title on your EVISE Homepage, then click 'Download zip file'.

Research Data Related to this Submission

There are no linked research data sets for this submission. The following reason is given:
Data will be made available on request

Dear Editor,

Please find enclosed the manuscript: **Intraplate magmatism at a convergent plate boundary, the case of the Cenozoic northern Adria magmatism** by Valentina Brombin, Costanza Bonadiman, Fred Jourdan, Guido Roghi, Massimo Coltorti, Laura E. Webb, Sara Callegaro, Giuliano Bellieni, Giampaolo De Vecchi, Roberto Sedea, and Andrea Marzoli· for a potential publication in Earth-Science Reviews.

The manuscript presents new geochemical and geochronological data of Cenozoic intraplate–related ultrabasic, basic, and acid magmatic products from the Veneto Volcanic Province, a magmatic province of the Southeastern Alpine domain (north-east Italy). Such products were investigated in order to explain the occurrence of magmatic products with anorogenic signature in the Southeastern Alps domain, during the Alpine orogenesis.

The new major and trace element geochemical data of the Southeastern Alps magmatic products allowed to constrain the potential nature and evolution of their mantle source(s), while the combination of the biostratigraphic data and the new high–resolution $^{40}Ar/^{39}Ar$ ages allowed to reconstruct the temporal evolution of the Veneto Volcanic Province magmatism.

Finally, both geochemical and geochronological data were used to review the intriguing geodynamic scenario of the Alpine domain, to explain the occurrence of anorogenic magmatic events in a subduction-dominated geological setting.

For all these aspects, we believe this work may be considered for publication with Earth-Science Reviews. This manuscript is an original work, which has not been published and is not under consideration for publication elsewhere.

All the authors have seen the manuscript and agree about its submission to Earth-Science Reviews.

Even if we have no particular preferences about potential reviewers, we suggest the following scientists: Maurizio Muzzucchelli (University of Modena and Reggio Emilia, Italy); Marco

Brenna (Univesity of Otago, New Zealand); Gilles Chazot (Université de Bretagne Occidentale, UBO, France); Alberto Zanetti (IGG-CNR, Pavia, Italy).

Thank you very much for your consideration and handling.

For the authors,

Costanza Bonadiman

Intraplate magmatism at a convergent plate boundary, the case of the Cenozoic northern Adria magmatism

Valentina Brombin[a], Costanza Bonadiman[a]*, Fred Jourdan[b], Guido Roghi[c], Massimo Coltorti[a], Laura E. Webb[d], Sara Callegaro[e], Giuliano Bellieni[f], Giampaolo De Vecchi[f], Roberto Sedea[f] Andrea Marzoli[c,f]

[a] *Dipartimento di Fisica e Scienze della Terra, Università di Ferrara, Italy*

[b] *Western Australian Argon Isotope Facility, School of Earth and Planetary Sciences & JdL Centre, Curtin University, Perth, Western Australia, Australia;*

[c] *Istituto di Geoscienze e Georisorse, CNR, Padova, Italy*

[d] *Department of Geology, University of Vermont, Vermont, USA;*

[e] *Centre for Earth Evolution and Dynamics, University of Oslo, Norway;*

[f] *Dipartimento di Geoscienze, Università di Padova, Italy*

* Corresponding author: bdc@unife.it

ABSTRACT

The complex European–Adria geodynamic framework, which led to the formation of the Alpine belt, is considered responsible for the orogenic magmatism that occurred in the Central Alps along the Periadriatic/Insubric Line (late Eocene–early Oligocene) and the anorogenic magmatism that occurred in the Southeastern Alps (late Paleocene–early Miocene). While subduction–related magmatic activities are expected near convergent margins, the presence of the intraplate–related magmatic products is still puzzling. Therefore, in this work new geochemical and geochronological data of magmatic products from the Veneto Volcanic Province (VVP, north–east Italy) are provided in order to constrain the Cenozoic intraplate magmatism of the Southeastern Alps. The VVP is formed by dominant basic–ultrabasic (from nephelinites to tholeiites) magmatic products and by localized acid (latitic, trachytic, and rhyolitic) volcanic and sub–volcanic bodies. Trace element patterns and ratios suggest that the mantle source of the basanitic magma types was a phlogopite–bearing garnet lherzolite, while those of the tholeiitic magma types was an anhydrous (i.e., without residual phlogopite and amphibole) garnet lherzolite. All the basic–ultrabasic VVP magmatic products exhibit enrichments in Ba, Sr, and P, indicating the mantle sources could be metasomatized by carbonatitic melts.

According to the biostratigraphic records and our new $^{40}Ar/^{39}Ar$ ages, VVP eruptions occurred in several pulses, reflecting the extensional phases experienced by the Eastern Alpine domain. The volcanism started in the late Paleocene in the western sector of the VVP where activity was widespread also during the Eocene (45.21± 0.11 Ma – 38.73 ± 0.44 Ma). In the eastern sector eruptions took place only in the early Oligocene (32.35 ± 0.09 Ma – 32.09 ± 0.29 Ma) and in the early Miocene (~ 22 – 23 Ma).

Previously, as suggested for neighboring orogenic magmatism, also the anorogenic magmatic activities were interpreted as resulting from mantle upwellings through slab window(s) following the European slab break–off occurred ~ 35 Ma. However, considering i) new tomographic images evidencing a continuous subvertical slab beneath the Central Alps, and ii) the onset of magmatic activity in the VVP in the late Paleocene (i.e., before the slab break–off) and its continuation until Miocene, we propose an alternative geodynamic scenario to explain the anorogenic magmatism. The westward rollback of the European slab caused the retreat and steepening of the sinking plate. As a consequence, the sub–slab mantle material escaped and upwelled from the front of the slab and created a poloidal mantle flow. The latter induced the breakdown of carbonates in calcareous metasediments and carbonated metabasics within the subducting oceanic slab, providing

carbonatitic melts, which could be responsible for the metasomatism of the VVP mantle sources. After that, the poloidal mantle flow also induced i) the extensional deformation in the overriding Adria microplate and ii) the decompressional melting of VVP mantle sources, iii) triggering the magmatism with intraplate affinity. During these processes, the Adria microplate also rotated counterclockwise, allowing the poloidal mantle flow to affect different portions of the overlying lithosphere and generating up to five eruptive centers within the VVP.

Intraplate magmatism at a convergent plate boundary, the case of the Cenozoic northern Adria magmatism

Valentina Brombin[a], Costanza Bonadiman[a]*, Fred Jourdan[b], Guido Roghi[c], Massimo Coltorti[a], Laura E. Webb[d], Sara Callegaro[e], Giuliano Bellieni[f], Giampaolo De Vecchi[f], Roberto Sedea[f] Andrea Marzoli[c,f]

[a] *Dipartimento di Fisica e Scienze della Terra, Università di Ferrara, Italy*

[b] *Western Australian Argon Isotope Facility, School of Earth and Planetary Sciences & JdL Centre, Curtin University, Perth, Western Australia, Australia;*

[c] *Istituto di Geoscienze e Georisorse, CNR, Padova, Italy*

[d] *Department of Geology, University of Vermont, Vermont, USA;*

[e] *Centre for Earth Evolution and Dynamics, University of Oslo, Norway;*

[f] *Dipartimento di Geoscienze, Università di Padova, Italy*

* Corresponding author: bdc@unife.it

ABSTRACT

The complex European–Adria geodynamic framework, which led to the formation of the Alpine belt, is considered responsible for the orogenic magmatism that occurred in the Central Alps along the Periadriatic/Insubric Line (late Eocene–early Oligocene) and the anorogenic magmatism that occurred in the Southeastern Alps (late Paleocene–early Miocene). While subduction–related magmatic activities are expected near convergent margins, the presence of the intraplate–related magmatic products is still puzzling. Therefore, in this work new geochemical and geochronological data of magmatic products from the Veneto Volcanic Province (VVP, north–east Italy) are provided in order to constrain the Cenozoic intraplate magmatism of the Southeastern Alps. The VVP is formed by dominant basic–ultrabasic (from nephelinites to tholeiites) magmatic products and by localized acid (latitic, trachytic, and rhyolitic) volcanic and sub–volcanic bodies. Trace element patterns and ratios suggest that the mantle source of the basanitic magma types was a phlogopite–bearing garnet lherzolite, while those of the tholeiitic magma types was an anhydrous (i.e., without residual phlogopite and amphibole) garnet lherzolite. All the basic–ultrabasic VVP magmatic products exhibit enrichments in Ba, Sr, and P, indicating the mantle sources could be metasomatized by carbonatitic melts.

According to the biostratigraphic records and our new $^{40}Ar/^{39}Ar$ ages, VVP eruptions occurred in several pulses, reflecting the extensional phases experienced by the Eastern Alpine domain. The volcanism started in the late Paleocene in the western sector of the VVP where activity was widespread also during the Eocene (45.21± 0.11 Ma – 38.73 ± 0.44 Ma). In the eastern sector eruptions took place only in the early Oligocene (32.35 ± 0.09 Ma – 32.09 ± 0.29 Ma) and in the early Miocene (~ 22 – 23 Ma).

Previously, as suggested for neighboring orogenic magmatism, also the anorogenic magmatic activities were interpreted as resulting from mantle upwellings through slab window(s) following the European slab break–off occurred ~ 35 Ma. However, considering i) new tomographic images evidencing a continuous subvertical slab beneath the Central Alps, and ii) the onset of magmatic activity in the VVP in the late Paleocene (i.e., before the slab break–off) and its continuation until Miocene, we propose an alternative geodynamic scenario to explain the anorogenic magmatism. The westward rollback of the European slab caused the retreat and steepening of the sinking plate. As a consequence, the sub–slab mantle material escaped and upwelled from the front of the slab and created a poloidal mantle flow. The latter induced the breakdown of carbonates in calcareous metasediments and carbonated metabasics within the subducting oceanic slab, providing carbonatitic melts, which could be responsible for the metasomatism of the VVP mantle sources. After that, the poloidal mantle flow also induced i) the extensional deformation in the overriding Adria microplate and ii) the decompressional melting of VVP mantle sources, iii) triggering the magmatism with intraplate affinity. During these processes, the Adria microplate also rotated counterclockwise, allowing the poloidal mantle flow to affect different portions of the overlying lithosphere and generating up to five eruptive centers within the VVP.

KEYWORDS

Intraplate magmatism; $^{40}Ar/^{39}Ar$ geochronology; Poloidal mantle flow; Southeastern Alps; Veneto Volcanic Province

1. INTRODUCTION

Synchronous orogenic (or subduction–related) and anorogenic (or intraplate–like) magmatic events can occur near subductive zones (*e.g.*, Okete–Alexandra Volcanic Province in New Zealand, Briggs and McDonough 1990; Cook et al., 2005; Faccini et al., 2018; north–west Turkey, Aldanmaz et al., 2006; Perşani volcanic field and South Harghita, in south-east Carpathian, Seghedi et al., 2011; Faccini et al., 2018; Kurdistan Province, western Iran, Allen et al., 2013; Trans–Mexican Volcanic Belt, Neumann et al., 2016; Payenia Volcanic Province in Argentina, Pallares et al., 2016). Calc–alkaline volcanism is expected at convergent margins (*e.g.*, Fytikas et al., 1984; de Boer et al., 1988; Bradley et al., 2003; Kay et al., 2007; Aragón et al., 2013), whereas many interpretations have been proposed to explain the apparently unusual occurrence of magmatism with intraplate geochemical signatures in collisional settings. These magmas have been related to i) upwelling of a mantle plume through a slab window after a slab detachment (*e.g.*, Ferrari, 2004); ii) activation of extensional faulting in the foreland after a collisional event (*e.g.*, Verma, 2002; Aldanmaz et al., 2006); and iii) lateral and frontal ingress of asthenosphere into the mantle wedge region induced by sinking and rollback of the slab (*e.g.*, Ferrari et al., 2001; Faccenna et al., 2011; Neumann et al., 2016).

In order to contribute to this (global scale) debate we investigated the relationship between the Alpine regional tectonic evolution and the alkaline to tholeiitic magmatic activity that affected the Southeastern Alps from Paleocene to Miocene. Such activity generated the Veneto Volcanic Province (VVP), one of the widest magmatic districts of the Adria microplate (Fig. 1). The VVP magmas are characterized by an intraplate geochemical signature, whereas contemporaneous middle Eocene-early Oligocene sub–alkaline to calc–alkaline basic plutons and dikes along the Periadriatic/Insubric Line in the Central Alps display a subduction fingerprint (i.e., Bergell, Triangia, Adamello; Brack, 1981, 1984; Kagami et al., 1991; von Blanckenburg, 1992; Callegari and Brack, 2002; Oberli et al., 2004; Harangi et al., 2006; Conticelli et al., 2009; Schaltegger et al., 2009; Alagna et al., 2010; Bergomi et al., 2015; Fig. 1a). The Periadriatic Cenozoic subduction–related magmatism of the Central Alps is generally related to upwelling of asthenospheric mantle material through a slab window after the late

Eocene Adria–Europe continental collision (~ 35 Ma; Stampfli et al., 1998, 2002; Rosenbaum and Lister, 2005). The mantle flow heated the supra-subduction hydrated mantle wedge, causing melting of the subcontinental lithosphere (Bergomi et al., 2015). According to the literature, the slab break–off occurrence may explain also the alkaline magmatism in the Southeastern Alps: mantle diapirs were sucked into the slab window and upwelled towards shallower levels heating the overriding lithospheric plate to the point of triggering partial melting (Macera et al., 2003; Bergomi et al., 2015). However, this interpretation is not consistent with the late Paleocene onset of the Southeastern Alps magmatism, *i.e.* before the supposed slab break–off, as suggested by biostratigraphic data. Aiming to unravel the interaction between the alkaline magmatism and the Alpine orogenesis, we combine the literature biostratigraphic data with new high–resolution $^{40}Ar/^{39}Ar$ ages of magmatic products from the Southeastern Alps. In doing this, we also present new major and trace element geochemical data of the Southeastern Alps magmatic products to constrain the potential nature and evolution of their mantle source(s).

2. A BRIEF DESCRIPTION OF GEOLOGICAL EVOLUTION OF THE ALPS

Both orogenic and anorogenic igneous activities within the Alpine realm are connected with the relative movements of the European plate and Adria microplate, which are still debated after a century of detailed structural work. Convergence of the two plates is considered to have started in the Early Cretaceous as a result of the final closure of the Meliata Ocean, a back–arc basin, which separated the two continental plates since the early Permian (Stampfli et al., 1998, 2002; Rosenbaum et al., 2002; Dézes et al., 2004; Schmid et al., 2004, Rosenbaum and Lister, 2005). The convergence of the Adria microplate and European plate marks the onset of the Alpine orogenesis, which occurred along the northern margin of the Adria microplate (Stampfli et al., 1998, 2002; Rosenbaum et al., 2002; Schmid et al., 2004, Rosenbaum and Lister, 2005). In particular, orogenic processes took place first in the Eastern Alps (peak of high–pressure metamorphism at ~ 100–90 Ma) and then in the Western Alps (peak of high–pressure metamorphism at ~ 85–60 Ma) (Manzotti et al., 2014 and references therein). During the Paleocene (at ~ 65–55 Ma), convergence ceased for a period of 10 My due to Adria–Europe continental collision in the Eastern Alps after the subduction of the easternmost portion of Piedmont–Liguria Ocean beneath the advancing orogenic wedge (Stampfli et al., 1998, 2002; Rosenbaum et al., 2002; Dézes et al., 2004; Schmid et al., 2004; Rosenbaum and Lister, 2005). Since the early Eocene the reprise of the Adria–Europe convergence led to the subduction and final closure of the Piedmont–Liguria Ocean and Valais Ocean in the Western Alps domain at ~ 45 Ma and ~ 35 Ma, respectively (Rubatto et al., 1998; Stampfli et al., 1998, 2002; Rosenbaum and Lister, 2005). According to literature, the subducted oceanic lithospheric slab of the Central and Eastern Alps detached from the European foreland lithosphere after closure of the Valais Ocean (*e.g.*, von Blanckenburg and Davies, 1995; Stampfli et al., 1998, 2002; Dézes et al., 2004). During the Eocene with the ongoing Adria–Europe collision, E–W extension developed parallel to the belt in the Eastern Alps (Ratschbacher et al., 1989; Zampieri et al., 1995). Such rifting phase extended also into the Central Alps, in the Oligocene from ~ 34 to ~ 28 Ma (Ring, 1994; Nievergelt et al., 1996; Challandes et al., 2003; Glodny et al., 2008; Pleuger et al., 2008; Steck, 2008; Beltrando et al. 2010; Ring and Gerdens, 2016; Schmid et al., 2017). This extensional phase of the overriding plate was probably induced by the rollback of the retreating SE–dipping slab (Rosenbaum and Lister, 2005). From ~ 30 Ma until the Oligocene–Miocene boundary (~ 23 Ma), the extensional processes stopped and large-scale coarse clastic sedimentation occurred in the Eastern Alps in response to an accretionary event (Frisch et al., 2000; Rosenbaum and Lister, 2005). Another phase of extension occurred during the early and middle Miocene due to the onset of lateral tectonic extrusion at the Oligocene–Miocene boundary, which rearranged the structural pattern and created the present elongated shape of the Eastern Alps (Ratschbacher et al., 1991; Frisch et al., 2000). This lateral tectonic extrusion is ascribed to a combination of gravity–driven orogenic collapse because of an over–thickened lithosphere, and tectonic escape along conjugate fault zones driven by tangential forces due to continuing N–S convergence between the Adriatic microplate and the European plate (Ratschbacher et al., 1991; Frish et al., 2000). However, the amount of Oligocene extension was limited, focused in the eastern Tauern

Window (Fig. 1a) and to the east of it, whereas Miocene extension occurred at a larger scale (Ratschbacher et al., 1991).

3. THE CENOZOIC CENTRAL AND SOUTHEASTERN ALPINE MAGMATISM

Cenozoic magmatism within the Alpine realm is variable in time and space reflecting the changing geodynamic framework during the convergence of the Adria microplate and the European plate (Bassi et al., 2008). In the Central Alps, the magmatic activity was orogenic and essentialy intrusive along the Periadriatic/Insubric line (Fig. 1a), represented by sub–alkaline and calc–alkaline basic intrusive bodies and basaltic and andesitic dikes with calc–alkaline to shoshonitic affinity. Based on radioisotopic ages, the climax of such magmatism ranged from ~ 34 to ~ 28 Ma (von Blancknburg and Davis, 1995; Rosenberg, 2004). However, the first evidence of igneous activity dates back at ~ 42 Ma with the emplacement of the southern Adamello batholith and coeval dikes (Schaltegger et al., 2009; Schoene et al., 2012; Bergomi et al., 2015). On the contrary, in the Southeastern Alps the magmatic activity was anorogenic with effusive to subvolcanic character. It occurred in an elongated NNW–SSE area of about 1500 km^2, defining from north–west to south–east five main volcanic districts: Val d'Adige, Lessini Mts., Marosticano, Berici Hills, and Euganean Hills (Beccaluva et al., 2007). Together, these districts constituted a Cenozoic magmatic province in the Southeastern alpine domain known in literature as Veneto Volcanic Province (VVP; *e.g.*, De Vecchi and Sedea, 1995; Beccaluva et al., 2001, 2007; Macera et al., 2003, 2008; Visonà et al., 2007; Fig. 1, 1a).

Figure 1. Simplified geological map of the Veneto Volcanic Province (VVP; De Vecchi and Sedea, 1995), showing the locations of the samples collected for this work. Ages (in Ma) of the magmatic rocks occuring in the VVP are framed with blue dashed line (literature data) and red continuous line (this work). Ages in italics are derived from mini–plateaus (50–70% ^{39}Ar released) and are considered minimum ages (see explanation in section 9, and in section S2 of Supplementary materials). Red stars are $^{40}Ar/^{39}Ar$ ages, blue diamonds are U–Pb ages, blue triangles are Rb–Sr ages, blue circles are K–Ar dates, and black squares are samples of this work for which $^{40}Ar/^{39}Ar$ analyses were not performed. Previously published ages for Lessini Mts. are from Savelli and Lipparini (1979) and Visonà et al. (2007); ages for Euganean Hills are from Zantendeschi (1994) and Bartoli et al. (2014); ages for Marosticano area are from Savelli and Lipparini (1979). Inset a) present–day location of VVP in the Italian peninsula, in relation to European, African plates and Adria microplate (modified from Carminati and Doglioni, 2012) and locations of Periadriatic basic and acid plutons, in blue and in black, respectively, along the Periadriatic/Insubric line. For comparative purpose, in this work only the Periadriatic basic plutons of the Central Alps were considered. Abbreviation for plutons: B = Bergell, T = Trigia, A = Adamello, R = Rensen, VdR = Vedrette di Ries. **[2 columns fitting]**

3.1 Geological outline

Magmatic activity started in the VVP already in the Paleocene (Beccaluva et al., 2007; Bassi et al., 2008), along the Jurassic Trento carbonate platform, which encompassed the Val d'Adige and Lessini Mts. areas (Winterer and Bosellini, 1981; Dewey et al., 1989; Zampieri et al., 1995). After the Adria–Europe collision in the Eastern Alps (~ 65 Ma; Stampfli et al., 1998, 2002; Rosenbaum et al., 2002; Dézes et al., 2004; Schmid et al., 2004; Rosenbaum and Lister, 2005), extension developed (Ratschbacher et al., 1989). As a consequence in the Southeastern Alpine domain the rigid Trento platform block–faulted forming a horst and graben structure, called the Alpone–Agno Graben (Zampieri, 1995). Until the middle Eocene the extensional tectonics of the new NNW–SSE transtensional fault systems and the Alpone–Agno Graben controlled the deposition of limestone and the volcanic activity, which manifested with short–lived pulses (Barbieri et al., 1991) in the Monte Baldo area for the Val d'Adige district and along the Lessini Mts. district (Luciani, 1989). Therefore, in the troughs of the horst and graben structure basic–ultrabasic hyaloclastites, volcanoclastics, subaqueous, and subaerial lava flows were accumulated and interbedded between the Scaglia Rossa (Upper Cretaceous–late Paleocene) and the Eocene limestones, or within the latter (Fig. 2).

According to biostratigraphic data the magmatic activity occurred later in the eastern VVP districts (*i.e.*, Euganean Hills and Marosticano areas; Piccoli et al., 1976, 1981; Luciani, 1989; Savelli and Lipparini, 1979). From the late Eocene to early Oligocene basic volcanic deposits were interbedded with marls of the Euganean Hills pelagic environment (De Vecchi et al., 1976; Piccoli et al., 1976, 1981; Fig. 2). In the early Oligocene, the Euganean magmatism changed and was dominated by rhyolites, trachytes and subordinately by trachyandesites (latites) and basalts, which formed mainly subvolcanic bodies and less abundant lava flows (De Vecchi et al., 1976; Piccoli et al., 1976, 1981). In the middle Oligocene, the magmatic activity resumed in the Marosticano (Fig. 2) and Lessini Mts. districts in a subaqueous environment as testified by the marine sediments (sandstones, calcarenites and limestones; Gavioli, 1972; Savelli and Lipparini, 1979) interbedded with the volcanic deposits (Fig. 2). Sparse Oligocene explosive and effusive volcanic activity is documented also in the Berici

Hills (west of the Euganean Hills; Bassi et al., 2008). At the end of the late Oligocene, the Marosticano and Lessini Mts. areas emerged (Frascari Ritondale Spano and Bassani, 1973) shortly before eruption of the last subaerial volcanic products at the beginning of the Miocene (Savelli and Lipparini, 1979). These volcanic deposits are overlain by coralline calcarenites of early Miocene age (Frascari Ritondale Spano, 1969; Savelli and Lipparini, 1979; Fig. 2), testifying to a new transgression event.

Figure 2. Simplified Upper Cretaceous to lower Miocene stratigraphy of the studied areas: Monte Baldo northern sector (Val d'Adige district; Luciani, 1989; De Vecchi and Sedea, 1995), Eastern Lessini Mts. (De Vecchi and Sedea, 1995; Bassi et al., 2008), Euganean Hills (Piccoli et al., 1976, 1981), and Marosticano (Frascari Ritondale Spano and Bassani, 1973; De Vecchi and Sedea, 1995; Bassi et al., 2008). Ages and uncertainties are reported in Ma. Ages in italics are derived from mini–plateaus (50–70% ^{39}Ar released) and are considered minimum ages only (see explanation in section 9 and in the section S2 of Supplementary materials). Ages derived from pre–erupted zircons from Lessini Mts. and Euganean Hills districts are considered maximum ages (see explanation in section 4). Previously published geochronological data for eastern Lessini Mts. are from Borsi et al. (1969), Savelli and Lipparini (1979), and Visonà et al. (2007), for Euganean Hills are from Borsi et al. (1969), Zantendeschi (1994), and Bartoli et al. (2014), and for Marosticano are from Savelli and Lipparini (1979). In the figure the main geodynamic events, extension phases, and coarse clastic sedimentation occurred in Central and Eastern Alps are reported, as well as the climax of the orogenic Periadriatic Central Alps magmatism. **[2 columns fitting]**

4. PREVIOUS GEOCHRONOLOGICAL STUDIES OF VVP

The integration of stratigraphic records with reliable radioisotopic ages allows to i) better constrain the distribution and the timeframe of such highly variable, but temporally short, magmatic activity and ii) infer the geodynamic evolution of this magmatic province. Previously obtained geochronological data are mainly K–Ar ages on basic–ultrabasic whole–rocks (Borsi et al., 1969; Savelli and Lipparini, 1979; Fig. 1). These K–Ar data yielded eruption ages of 42.5 ± 1.5 to 20.4 ± 0.8 Ma for the Lessini Mts., 42.0 ± 1.5 Ma for the Euganean Hills, and from 33.7 ± 1.2 to 20.4 ± 0.8 Ma for the Marosticano district. However, the reliability of such ages is questionable, as the K–Ar dating technique is not able to recognize (and correct for) non–atmospheric $^{40}Ar/^{36}Ar$ ratios and alteration effects (Oostingh et al., 2017). Zantendeschi (1994) dated Euganean trachytes and rhyolites using the whole–rock Rb–Sr method (Fig. 1), the obtained eruption ages span from 34 ± 2 to 28 ± 1 Ma. These ages also must be treated with caution, as the ^{87}Rb decay constant is still poorly defined and Rb/Sr isotopic system is prone to secondary alteration (Begemann et al., 2001; Schmitz et al., 2003). The most recent radioisotopic data available (Fig. 1) are U–Pb ages obtained using a sensitive high–resolution ion microprobe (SHRIMP) on zircons hosted i) in a porphyritic basanite lava and in two altered dykes of the Lessini Mts. (Visonà et al., 2007) and ii) in magmatic enclaves within trachytes of the Euganean Hills (Bartoli et al., 2014). These ages may be interpreted as maximum ages of eruptions as the analysed zircons were not crystallized directly from the erupted magma. The Lessini Mts. zircons yielded Eocene ages spanning from 51.1 ± 1.5 to 44.9 ± 2.8 Ma (Visonà et al., 2007), even if it should be considered that these data are not concordant. Zircons from the Euganean Hills xenoliths yielded Oligocenic ages of 31.9 ± 1.3 Ma and 30.6 ± 1.5 Ma (Bartoli et al., 2014).

From this overview on the currently available geochronological data and related uncertainties, it is clear that more accurate age data are essential for the temporal reconstruction of the VVP magmatism. In this work, new high–resolution ages were obtained using the $^{40}Ar/^{39}Ar$ systematic on groundmass samples on mineral separates, which is currently widely accepted as an accurate dating technique (McDougall and Harrison, 1999).

5. SAMPLING

Following biostratigraphic information we selected our samples in order to encompass most of the time range of the VVP magmatism. From Val d'Adige and Lessini Mts., the two oldest magmatic districts, samples were collected from basic–ultrabasic lava flows and volcanic necks. BAL1 and BAL7, two out of three samples of Val d'Adige district, are from the northeastern part of Monte Baldo (Table 1; Fig. 1). BAL1 was collected nearly at the top of a subaqueous lava flow interbedded between middle and late Eocene limestones (Calcare di Torbole and Calcare di Nago; Fig. 2), whereas BAL7 was sampled from a thin sill between Cretaceous–Paleocene (Scaglia Rossa) and middle Eocene limestones (Calcare di Torbole; Fig. 2). The third sample from Val d'Adige district, BI14, was collected from a volcanic neck exposed in a quarry near Rovereto (Table 1; Fig. 1). The sampling for Lessini Mts. district was focused near the famous Bolca Fossil–Lagerstätte area (Papazzoni et al., 2014, and references therein). Sample TER1 (Table 1; Fig. 1) was collected from a lava flow interbedded with red clays of unknown age, whereas sample BOL1 (Table 1; Fig. 1) was collected from the volcanic neck preserved near the mentioned fossiliferous area. This neck cuts 10–20 m of freshwater–brackish sediments of probable Ypresian age (Barbieri and Medizza, 1969; Medizza, 1980; Sorbini, 1989; Giusberti, et al., 2014).

The Euganean Hills are the only VVP magmatic district where basic, intermediate, and acid magmas erupted or intruded at shallow–depth forming lava flows and subvolcanic bodies (mainly laccoliths) during late Eocene–Oligocene (Fig. 2). We have sampled and analysed rocks in order to investigate the entire range of the lithologies. Samples EU1AB, EU53, EU52, EU8B, and EU13A represent the least differentiated products of the Euganean sample suite. The basaltic andesite lava flow EU1AB was collected from an outcrop in the western part of the Euganean Hills (Table 1; Fig. 1). The basaltic andesite sample EU53 was collected from a subvolcanic body at the center of the Euganean Hills, and basaltic trachyandesite EU52 from an intrusion cutting this basaltic andesite body (Table 1; Fig. 1). The basaltic trachyandesite EU8B and the latite EU13A were collected from subvolcanic bodies

(Monte Oliveto and Monte Cecilia), in the eastern and southern sectors of the Euganean Hills, respectively (Table 1; Fig. 1). Samples EU4, EU5B, and EU9 represent the most acid products available for the Euganean Hills. The trachyte EU4 (Monte Merlo quarry, northern sector of the Euganean Hills; Table 1; Fig. 1), the rhyolite EU5B (Monte Alto, eastern sector; Table 1; Fig. 1), and the rhyolite EU9 (Monte Ricco, southeastern sector; Table 1; Fig. 1), were collected from laccoliths intruded in the Euganean Marls Formation (Oligocene; Piccoli et al., 1976, 1981; Fig. 2).

Finally, for the Marosticano district, where one of the last VVP magmatic events occurred, we sampled two specimens (LB1 and 25B). These samples were collected from the ultrabasic volcanic neck cutting the middle Oligocene marine sediments of the Salcedo formation at Monte Gloso (Savelli and Lipparini, 1979; Table 1; Figs. 1, 2).

6. ANALYTICAL METHODS

Whole–rock major and trace elements were determined by Wavelength Dispersive X–Ray Fluorescence Spectrometry (WDXRF) at the University of Ferrara (IT; ARL Advant–XP spectrometer) and at the University of Padova (IT; Philips PW1404). Rb, Sr, Y, Zr, Nb, Hf, Ta, Th, U, and rare–earth elements (REEs) were performed with Inductively Coupled Plasma–Mass Spectrometry (ICP–MS) at the University of Ferrara (Thermo Series X–I spectrometer) and at the University of Bretagne Occidentale, Brest (FR; Thermo Element2). Clinopyroxene compositions were determined by means of a CAMECA SX50 electron microprobe at the IGG–CNR of Padova.

For $^{40}Ar/^{39}Ar$ geochronological analyses, after irradiation in TRIGA Reactor at the Oregon State University (USA) or US Geological Survey nuclear reactor (Denver, USA), groundmass and mineral separates were analysed by laser step–heating with i) ARGUS VI (samples BAL1, BAL7, TER1, BOL1, LB1, and EU52) and ii) MAP 215–50 (samples EU4, EU5B, EU8B, and EU13A) mass spectrometers at Curtin University within the Western Australian Argon Isotope Facility (WAAIF) of the John de Laeter Centre and iii) Nu Instruments Noblesse magnetic sector noble gas mass spectrometer (samples BI14 and 25B) at the Noble Gas Lab of the University of Vermont. Extended analytical procedures and details are reported in section S1 of the Supplementary materials.

7. PETROGRAPHY AND ROCK CLASSIFICATION

Samples BAL7, BI14 (Val d'Adige district), BOL1 (Lessini Mts. district), LB1, and 25B (Marosticano district) are classified as basanites in the total alkali *vs.* silica (TAS) diagram (Le Maitre et al., 2002; Fig. 3) and they are nepheline-normative (Table 1). These rocks show porphyritic texture with large (up to 1 mm across) phenocrysts of euhedral olivine and smaller clinopyroxene (prevalently diopside; up to 0.5 mm across) as dominant phenocrysts set in a microcrystalline groundmass constituted by acicular plagioclase, clinopyroxene, and oxides. Interestingly, BOL1, LB1, and 25B host small (3–4 mm) spinel peridotite xenoliths, probably fragments of the bigger (5–15 cm) counterparts already discovered in alkaline basalts of the Val d'Adige, Lessini Mts., and Marosticano districts (Morten et al., 1989; Siena and Coltorti, 1989, 1993; Beccaluva et al., 2001; Gasperini et al., 2006; Brombin et al., 2018). These fragments were extracted from the samples before proceeding with the chemical analyses.

BAL1 (Val d'Adige district) and TER1 (Lessini Mts. district) are two basalts according to the TAS classification (Fig. 3), in particular the first sample is olivine/hyperstene normative, while the second one is quartz-normative (Table 1). They have intergranular texture characterized by elongated and euhedral plagioclase (up to 2 mm across) and subhedral–anhedral clinopyroxene, olivine and oxides filling spaces between plagioclase crystals. The presence of scarce iddingsite (substituting for olivine) and amygdules of secondary hydrothermal minerals are indicative of slight alteration. According to the TAS diagram, EU1AB and EU53 (Euganean Hills district) are classified as basaltic andesites (Fig. 3). Both samples are quartz-normative (Table 1) and they have clinopyroxene, plagioclase, and oxides as phenocrysts and in the groundmass.

EU52 and EU8B (Euganean Hills district) are classified as basaltic trachyandesites in the TAS diagram (Fig. 3). EU52 is nepheline-normative, while EU8B is quartz-normative (Table 1). The phenocrysts of these two samples are plagioclase, amphibole and clinopyroxene in a microcrystalline groundmass of plagioclase and oxides. The plagioclase phenocrysts (up to 2 mm across in EU8B and up to 5 mm across in EU52) are generally euhedral with occasional sieved–textured centers (EU8B). The clinopyroxene phenocrysts (up to 1 mm across) are subhedral with rounded edges. Only EU52 exhibits large (up to 5 mm across) euhedral amphibole without any sign of alteration.

Sample EU13A (Euganean Hills district) is classified as latite (Fig. 3) and it is quartz-normative (Table 1). It contains medium–grained (0.5–1.5 mm across) plagioclase, biotite, and clinopyroxene in a microcrystalline groundmass of plagioclase feldspar, and oxides. The plagioclase phenocrysts (up to 1.5 mm across) are generally euhedral; a sieved–textured core is also present. The clinopyroxene crystals (1 mm across) are subhedral with rounded edges. Biotite (1 mm across) is subhedral and partly replaced by oxides along the rims.

EU4, EU5B, and EU9 (Euganean Hills district) are the most felsic samples of the entire suite. According to the TAS diagram, EU4 is a trachyte, whereas EU5B and EU9 are rhyolites (Fig. 3). All of them are quartz-normative (Table 1). They exhibit glomeroporphyritic texture and the phenocrysts are predominantly alkali feldspar (sanidine, up to 5 mm across), plagioclase (up to 5 mm across), and biotite (1–2 mm across) in a microcrystalline groundmass consisting of alkali feldspar and Fe–Ti oxides. Only in EU4 phenocrysts of amphibole (1–2 mm across) are present. The glomerocrysts, up to 1 cm in diameter, are both monomineralic (alkali feldspar) or formed by plagioclase and alkali feldspar in the same cluster. Crystals within these glomerocrysts are subhedral with rounded corners on the edges of grains.

Figure 3. Total Alkali *vs.* Silica (TAS) classification diagram (Le Maitre et al., 2002) of the magmatic products from Val d'Adige, Lessini Mts., Marosticano, and Euganean Hills studied in this work (large symbols) and in literature (small symbols). Val d'Adige compositions are from Beccaluva et al. (2007); Lessini Mts., and Marosticano compositions are from Macera et al. (2003) and Beccaluva et al. (2007); Euganean Hills compositions are from Milani et al. (1999) and Macera et al. (2003). The fields for trachybasalt and trachyandesite are labelled here "potassic trachybasalt" and "latite", respectively, as most of the samples of this study display ($Na_2O - K_2O$) $\leq$ 2.0 and are therefore potassic, as defined by Le Maitre (2002). The alkaline–tholeiitic discrimination line is from Irvine and Baragar (1971). **[1 column fitting]**

8. GEOCHEMISTRY

Bulk major and trace element compositions of the analysed magmatic rocks are reported in Tables 1 and 2. On the TAS diagram (Fig. 3) this group of magmatic rocks overlaps with those previously published for the VVP (Milani et al., 1999; Macera et al., 2003; Beccaluva et al., 2007), spanning a wide range of compositions from alkaline to subalkaline and encompassing ultrabasic, basic, intermediate, and acid rocks.

The basic–ultrabasic rocks span a relatively wide range in terms of SiO_2 (42.01 to 53.22 wt.%; Table 1), MgO (12.26 to 3.85 wt.%; Table 1), and mg# [69.64 to 43.06, where mg# is defined as 100 x $Mg/(Mg + Fe^{2+})_{mol}$, Fe^{3+}/Fe^{2+} being 0.15; Table 1] reflecting the different degree of evolution for the VVP lithologies (*i.e.*, from basanites to basaltic trachyandesites). The analysed samples have predominantly alkaline affinities with the majority of the samples having potassic affinity [$(Na_2O - K_2O) \leq 2.0$ wt.%] with $(Na_2O - K_2O)$ ranging from 0 to 1.72 wt.%. Only BI14, EU53, and EU1AB have sodic affinity [$(Na_2O - K_2O) = 2.51 - 3.48$ wt.%]. Chondrite–normalized rare earth element (REE) patterns are generally parallel for all basic–ultrabasic rocks (Fig. 4a). These patterns are strongly light REE (LREE) enriched with a significant LREE to heavy REE (HREE) fractionation [$(La/Yb)_N = 5.5$ to 24.3; $(Dy/Lu)_N = 1.8$ to 2.4; Fig. 4a]. Irrespective to the lithology, samples from Val d'Adige, Lessini Mts., Euganean Hills (EU1AB and EU53), and Marosticano exhibit negative Rb and K anomalies and spikes for Ba, Sr, and P in the primitive mantle–normalized incompatible trace element diagram (Fig. 4b). Basaltic trachyandesite EU52 (Euganean Hills) mimics the general trace element features of the basic–ultrabasic samples. However, it lacks significant Sr and P spikes and it is depleted in Ba, consistently with its more evolved character and with possible feldspar and apatite fractionation (Fig. 4b).

The intermediate–acid rocks have higher SiO_2 (55.63 to 72.00 wt.%; Table 1) and lower MgO (3.14 to 0.14 wt.%; Table 1) contents with respect to the previous group, consistent with their more evolved nature. All the samples of this group have potassic affinity [$(Na_2O - K_2O) = 0 - 1.55$]. No trace element analyses were performed for this group, as in this work we preferred to focus on the geochemistry of basic–ultrabasic samples that can shed light on their mantle sources, while more evolved rocks may be significantly affected by fractional crystallization.

Sample	**BAL1**	**BAL7**	**BI14**	**TER1**	**BOL1**	**EU1AB**	**EU53**	**EU52**	**EU8B**
Rock	Basalt	Basanite	Basanite	Basalt	Basanite	Basaltic andesite	Basaltic andesite	Basaltic trachyandesite	Basaltic trachyandesite
District	Val d'Adige	Val d'Adige	Val d'Adige	Lessini Mts.	Lessini Mts.	Euganean Hills	Euganean Hills	Euganean Hills	Euganean Hills
Coordinates	45°47’02.12”N 10°54’18.26”E	45°44’37.00”N 10°53’04.00”E	45°47’02.12”N 10°54’18.26”E	45°35’34.05”N 11°12’58.89”E	45°35’51.84”N 11°12’31.34”E	45°19’40.08”N 11°38’58.00”E	45°32’87.00”N 11°68’48.00”E	45°32’87.88”N 11°68’48.75”E	45°19’07.08”N 11°46’31.04”E
SiO_2	46.83	42.62	42.01	48.72	43.00	52.00	53.22	51.70	55.63
TiO_2	2.75	3.71	3.22	2.80	3.44	2.45	2.37	2.75	2.01
Al_2O_3	14.59	13.04	14.65	13.53	13.21	14.85	14.83	16.29	15.53
Fe_2O_3	14.61	14.56	13.11	11.00	14.35	10.02	11.24	10.43	8.82
MnO	0.20	0.19	0.17	0.36	0.19	0.12	0.12	0.12	0.13
MgO	6.94	8.96	8.28	10.77	9.55	6.25	6.22	3.85	3.41
CaO	10.39	11.03	10.34	9.93	10.23	9.50	8.66	6.12	6.47
Na_2O	2.24	3.09	4.98	1.09	3.06	3.10	3.24	4.35	4.23
K_2O	0.75	1.37	1.42	1.17	1.45	0.59	0.43	3.23	2.68
P_2O_5	0.70	1.53	1.81	0.64	0.97	0.35	0.26	0.97	0.59
Tot	100.01	100.10	100.00	100.00	99.45	99.23	100.59	99.81	99.50
LOI	3.02	1.10	2.17	3.30	0.55	3.69	3.11	0.83	2.34
mg#	49.32	55.77	56.40	66.72	57.69	56.10	53.13	43.06	44.20
Quartz	-	-	-	1.4	-	2.6	4.4	-	2.6
Nepheline	-	7.9	18.3	-	8.2	-	-	0.43	-
Diopside	16.2	22.3	21.6	13.4	21.8	16.5	13.6	7.2	10.6
Hyperstene	16.1	-	-	30.9	-	18.1	19.6	-	11.6
Olivine	6.0	18.0	15.3	-	19.5	-	-	11.2	0-

mg# = 100 x Mg/(Mg+Fe^{2+})$_{mol}$ considering Fe^{3+}/Fe^{2+} 0.15

Table 1. Whole–rock major element compositions (wt.%) and CIPW normative compositions of magmatic products from Val d'Adige, Lessini Mts., Euganean Hills, and Marosticano.

Sample	**EU13A**	**EU4**	**EU5B**	**EU9**	**LB1**	**25B**
Rock	Latite	Trachyte	Rhyolite	Rhyolite	Basanite	Basanite
District	Euganean Hills	Euganean Hills	Euganean Hills	Euganean Hills	Marosticano	Marosticano
Coordinates	45°15’07.02”N 11°41’27.00”E	45°20’20.09”N 11°39’06.09”E	45°19’16.00”N 11°45’24.00”E	45°14’57.02”N 11°44’28.07”E	45°76’72.83”N 11°67’78.97”E	45°76’72.00”N 11°67’78.00”E
SiO_2	56.90	65.52	69.86	72.00	43.22	44.02
TiO_2	2.00	0.69	0.39	0.32	3.47	3.12
Al_2O_3	15.68	16.51	15.41	14.81	11.52	12.80
Fe_2O_3	7.27	3.71	2.05	1.26	13.12	10.95
MnO	0.09	0.06	0.09	0.03	0.19	0.16
MgO	3.14	0.72	0.17	0.14	11.29	12.26
CaO	5.68	1.59	0.65	0.49	11.85	10.89
Na_2O	4.11	5.23	4.80	4.63	3.06	3.22
K_2O	3.59	5.11	5.77	5.56	1.36	1.53
P_2O_5	0.57	0.30	0.07	0.03	0.97	1.06
Tot	99.03	99.44	99.26	99.27	100.05	100.00
LOI	1.64	0.35	0.66	0.14	1.17	1.08
mg#	46.95	28.45	14.52	18.54	63.81	69.64
Quartz	3.5	10.3	17.6	22.3	-	-
Nepheline	-	-	-	-	11.0	10.4
Diopside	9.0	-	-	-	31.5	25.1
Hyperstene	9.8	5.6	2.6	1.5	-	-
Olivine	-	-	-	-	17.9	20.1

mg# = 100 x $Mg/(Mg+Fe^{2+})_{mol}$ considering Fe^{3+}/Fe^{2+} 0.15

Table 1 (continued). Whole–rock major element compositions (wt.%) of magmatic products from Val d'Adige, Lessini Mts., Euganean Hills, and Marosticano.

Sample	**BAL7**	**TER1**	**BOL1**	**EU1AB**	**EU53**	**EU52**	**LB1**
Rock	Basanite	Basalt	Basanite	Basaltic andesite	Basaltic andesite	Basaltic trachyandesite	Basanite
District	Val d'Adige	Lessini Mts.	Lessini Mts.	Euganean Hills	Euganean Hills	Euganean Hills	Marosticano
Rb	29.6	27.8	37.4	17.0	15.0	71.0	46.6
Ba	860	664	553	348	264	777	777
Th	6.80	5.87	5.99	2.95	2.85	10.1	6.85
U	1.77	1.34	1.42	0.83	0.82	2.56	2.00
Nb	124	74.3	91.4	28.0	21.0	96.6	118
Ta	4.47	2.52	3.74	1.38	1.43	4.64	4.67
La	66.6	39.0	47.0	18.4	13.7	72.4	57.5
Ce	131	75.8	96.1	38.5	28.5	128	109
Pr	15.5	8.37	11.5	4.68	3.71	14.4	12.1
Sr	1744	736	1060	473	349	929	1071
Nd	67.4	35.6	52.0	20.4	16.9	55.9	53.3
Zr	413	235	354	175	168	456	382
Hf	8.29	5.01	7.58	3.93	4.03	9.11	7.91
Sm	12.6	6.73	10.1	5.36	4.85	10.9	9.68
Eu	3.86	2.16	3.13	1.83	1.75	3.25	2.91
Gd	11.7	6.66	9.32	5.55	5.47	8.82	8.92
Tb	1.64	0.99	1.38	0.83	0.85	1.19	1.27
Dy	7.20	4.63	6.23	4.48	4.77	6.15	5.61
Y	40.8	28.7	35.4	24.1	24.0	34.6	31.5
Ho	1.28	0.88	1.10	0.83	0.88	1.10	1.00
Er	3.05	2.22	2.62	1.97	2.20	2.64	2.42
Yb	2.21	1.84	1.93	1.56	1.70	2.03	1.78
Lu	0.31	0.27	0.27	0.21	0.23	0.27	0.25

All trace elements (ppm) were analysed by ICP–MS except Ba (XRF).

Table 2. Trace element (ppm) compositions of magmatic products from Val d'Adige, Lessini Mts., Euganean Hills, and Marosticano.

Figure 4. Chondrite–normalized rare earth elements (a) and primitive mantle–normalized trace element patterns (b) for basic–ultrabasic rocks from Val d'Adige, Lessini Mts., Euganean Hills, and Marosticano. The least evolved Euganean Hills samples are also shown for comparison. Previously published trace element compositions for basic–ultrabasic rocks from Val d'Adige, Lessini Mts., Euganean Hills, and Marosticano (Macera et al., 2003; Beccaluva et al., 2007) are reported as a shaded area. Ocean Island Basalt composition (OIB; Sun and McDonough, 1989) is shown with a black dashed line. The average trace element compositions of orogenic calc–alkaline and sub–alkaline magmas of the Periadriatic Central Alps magmatism are from Bergomi et al. (2015) and are shown with a black continuous line. Normalizing factors are from McDonough and Sun (1995).

9. $^{40}Ar/^{39}Ar$ GEOCHRONOLOGICAL RESULTS

Detailed $^{40}Ar/^{39}Ar$ results of the analysed magmatic rocks are reported in Tables 3, 4. Groundmass samples of BAL1, BAL7, TER1, BOL1, and LB1 as well as amphibole and plagioclase separates of EU52 were analysed with a new generation noble gas multicollector mass spectrometer (ARGUS VI). Instead, mineral separates (*i.e.*, biotite, feldspar, sanidine) from EU8B, EU13A, EU4, EU5B, and EU9 were analysed with the MAP215–50 mass spectrometer. EU1AB and EU53, two basaltic andesites from the Euganean Hills district, could not be dated due to the lack of fresh K–rich minerals. Many analysed samples are characterized by $^{40}Ar/^{36}Ar$ ratios, which are above or below the atmospheric value (298.56 ± 0.31; Lee et al., 2006). Supra-atmospheric intercepts are indicative of excess ^{40}Ar whereas sub-atmospheric ratios are too low to be due to isotopic fractionation (Oostingh et al., 2017) and are rather interpreted in term of hydrothermal alteration signature (Baksi, 2006). In addition, many samples yielded only mini–plateaus (50–70% cumulative ^{39}Ar; Jourdan et al., 2007). The latter are less robust than their plateau counterparts and should be treated with caution. They might indicate the true crystallization age, but they might equally represent minimum age values, not too far from the crystallization age (Oostingh et al., 2017). The complete description of the dating result is reported in section S2 of Supplementary materials.

For Val d'Adige, the basalt BAL1 and basanite BAL7 $^{40}Ar/^{36}Ar$ intercepts are similar and slightly sub–atmospheric (BAL1 = 266 ± 23 and BAL7 = 264 ± 15; Table 3; Fig. 5 a, c), which allow equally calculating a plateau age of 41.69 ± 0.37 Ma (Table 3; Fig. 5b) and a mini–plateau age of 41.98 ± 0.20 Ma (Table 3; Fig. 5d), respectively.

TER1 and BOL1 were analysed for the Lessini Mts. district and yielded different $^{40}Ar/^{36}Ar$ and intercept ages. The basalt TER1 shows sub–atmospheric $^{40}Ar/^{36}Ar$ intercept (253± 25; Table 3; Fig. 5e) defining a mini–plateau age of 45.21 ± 0.11 Ma (Fig. 5f). The $^{40}Ar/^{36}Ar$ intercept of basanite BOL1 is 278 ± 19 (Table 3; Fig. 5g), close to the atmospheric $^{40}Ar/^{36}Ar$ ratio. This sample yielded a mini–plateau age of 38.73 ± 0.44 Ma (Table 3; Fig. 5h).

For the basaltic trachyandesite EU52 both amphibole and plagioclase were analysed. The amphibole is characterized by a $^{40}Ar/^{36}Ar$ intercept (295 ± 14; Table 3; Fig. 5i) indistinguishable from atmosphere, and yielded a mini–plateau age of 32.35 ± 0.09 Ma (Fig. 5j). The plagioclase $^{40}Ar/^{36}Ar$ intercept value is supra–atmospheric (397 ± 19; Table 3; Fig. 5k), indicating excess ^{40}Ar. Using the latter value, we obtained a plateau age of 32.16 ± 0.06 Ma (Table 3; Fig. 5l). The alkali–feldspar separate of the basaltic trachyandesite EU8B shows a value of 305 ± 99 (Table 3; Fig. 5m) for the $^{40}Ar/^{36}Ar$ intercept, which is indistinguishable from the atmospheric ratio and allows calculating a plateau age of 32.17 ± 0.32 Ma (Table 3; Fig. 5n). The feldspar separate of the latite EU13A yielded a $^{40}Ar/^{36}Ar$ intercept of 349 ± 136 (Fig. 5o) and a plateau age of 32.34 ± 0.51 Ma (Fig. 5p). The $^{40}Ar/^{36}Ar$ intercept age for the biotite separate of trachyte EU4 is 328 ± 43 (Table 3; Fig. 5q) and defines a plateau age of 32.09 ± 0.29 Ma (Fig. 5r). Also for the sanidine separate of rhyolite EU5B the $^{40}Ar/^{36}Ar$ intercept is slightly supra–atmospheric (343 ± 58; Fig. 5s); the calculated plateau age is 32.30 ± 0.52 Ma (Table 3; Fig. 5t). The sanidine separate of rhyolite EU9 shows a $^{40}Ar/^{36}Ar$ intercept value (315 ± 68; Table 3; Fig. 5u) indistinguishable from atmosphere and we obtained a plateau age of 32.17 ± 0.27 Ma (Table 3; Fig. 5v). It is clear that irrespective to the lithology all analysed Euganean samples yielded nearly indistinguishable ages, allowing to calculate a mean weighted age of 32.21 ± 0.09 Ma.

The basanite from the Marosticano district, LB1, yielded the youngest integrated age of the VVP samples analysed at WAAIF using the ARGUS VI mass spectrometer. It did not return isochron and plateau age, but almost all the steps indicate apparent ages between 20.5 and 23.2 Ma (Table 3; Fig. 5w, x).

Two additional basanites BI14 and 25B, from Val d'Adige and Marosticano, respectively, were analysed at the Noble Gas Geochronology Laboratory of the University of Vermont using the Nu Instruments Noblesse magnetic sector noble gas mass spectrometer with the purpose to expand the VVP geochronological dataset. Sample BI14 yielded a $^{40}Ar/^{36}Ar$ intercept of 207 ± 138 and a mini–plateau age of 40.73 ± 0.48 Ma (Table 4; Fig. 6a, b). This age is similar to those recorded by BAL1 and BAL7. As occurred for LB1, also the Marosticano basanite 25B did not provide ages (Table 4; Fig. 6c, d). However, for both Marosticano samples almost all the steps indicate apparent ages of ~ 22 – 23 Ma (Fig. 6d).

General characteristics				Isochron characteristics					Plateau characteristics			
Sample	**Lithology**	**Instrument**	**Separate**	**Inverse isochron age (Ma, ±2σ)**	**n**	**$^{40}Ar/^{36}Ar$ intercept (±2σ)**	**MSWD**	**P (%)**	**Plateau age (Ma, ±2σ)**	**Total ^{39}Ar released (%)**	**MSWD**	**P (%)**
Val d'Adige												
BAL1	Basalt	ARGUS VI	Groundmass	**41.70 ± 0.82**	16	266 ± 23	0.78	69	**41.69 ± 0.37**	75	0.39	98
BAL7	Basanite	ARGUS VI	Groundmass	*41.95 ± 0.46*	15	264 ± 15	0.82	64	*41.98 ± 0.20*	60	0.25	100
Lessini Mts.												
TER1	Basalt	ARGUS VI	Groundmass	*45.21 ± 0.15*	12	253 ± 25	1.00	44	*45.21 ± 0.11*	57	0.83	61
BOL1	Basanite	ARGUS VI	Groundmass	*40.60 ± 1.76*	17	278 ± 19	0.75	74	*38.73 ± 0.44*	62	0.99	46
Euganean Hills												
EU52	Basaltic trachyandesite	ARGUS VI	Amphibole	*32.37 ± 0.12*	10	295 ± 14	0.52	85	*32.35 ± 0.09*	67	0.48	89
			Plagioclase	**32.16 ± 0.08**	21	397 ± 19	0.65	87	**32.16 ± 0.06**	100	0.58	93
EU8B	Basaltic trachyandesite	MAP 215–50	Feldspar	**32.11 ± 0.98**	15	305 ± 99	0.85	61	**32.17 ± 0.32**	100	0.79	68
EU13A	Latite	MAP 215–50	Feldspar	**31.96 ± 1.13**	14	349 ± 136	0.52	91	**32.34 ± 0.51**	88	0.53	91
EU4	Trachyte	MAP 215–50	Biotite	**31.83 ± 0.50**	14	328 ± 43	0.88	57	**32.09 ± 0.29**	100	0.97	48
EU5B	Rhyolite	MAP 215–50	Sanidine	**31.87 ± 0.79**	15	343 ± 58	0.86	59	**32.30 ± 0.52**	100	1.00	45
EU9	Rhyolite	MAP 215–50	Sanidine	**32.02 ± 0.67**	14	315 ± 68	0.51	91	**32.17 ± 0.27**	100	0.48	94
Marosticano												
LB1	Basanite	ARGUS VI	Groundmass	No isochron age					No plateau age			

Data in italics are derived from mini–plateaus (50–70% ^{39}Ar released) and are considered minimum ages only, bold font represents statistically significant plateau ages. Mean square weighted deviation (MSWD) for isochron, plateau, and mini–plateau, number of analyses included in the isochron, $^{40}Ar/^{36}Ar$ intercept, percentage of ^{39}Ar degassed used in the plateau calculation, probability (P) for isochron, plateau and mini–plateau are indicate. Analytical uncertainties on the ages and $^{40}Ar/^{36}Ar$ intercepts are quoted at 2 sigma (2σ) confidence levels.

Table 3. Summary table of $^{40}Ar/^{39}Ar$ results for Val d'Adige, Lessini Mts., Euganean Hills, and Marosticano samples analysed at Western Australian Argon Isotope Facility (WAAIF).

General characteristics			**Isochron characteristics**				**Plateau characteristics**			
Sample	**Lithology**	**Separate**	**Inverse isochron age (Ma, ±2σ)**	**n**	**$^{40}Ar/^{36}Ar$ intercept (±2σ)**	**MSWD**	**Plateau age (Ma, ±2σ)**	**Total ^{39}Ar released (%)**	**MSWD**	**P (%)**
Val d'Adige										
BI14	Basanite	Groudmass	*42.2 ± 8.2*	7	207 ± 138	11.3	*40.73 ± 0.48*	57	0.8	45
Marosticano										
25B	Basanite	Groudmass	No isochron age				No plateau age			

Data in italics are derived from mini–plateau (50–70% ^{39}Ar released) and are considered minimum ages only. Mean square weighted deviation (MSWD) for isochron and mini–plateau, number of analyses included in the isochron, $^{40}Ar/^{36}Ar$ intercept, percentage of ^{39}Ar degassed used in the plateau calculation and probability (P) for mini–plateau are indicated. Analytical uncertainties on the ages and $^{40}Ar/^{36}Ar$ intercept are quoted at 2 sigma (2σ) confidence levels.

Table 4. Summary table of $^{40}Ar/^{39}Ar$ results for Val d'Adige, and Marosticano samples analysed at the Noble Gas Geochronology Laboratory of the University of Vermont with Nu Instruments Noblesse magnetic sector noble gas mass spectrometer.

Figure 5. $^{39}Ar/^{40}Ar$ *vs.* $^{36}Ar/^{40}Ar$ inverse isochrons and $^{40}Ar/^{39}Ar$ apparent age and K/Ca spectra, plotted against the cumulative percentage of ^{39}Ar released for VVP rocks analysed at Curtin University. Plateau ages (bold) are inverse isochron intercept corrected. Mini–plateaus (50–70% cumulative ^{39}Ar) are indicated in italics. Mean square weighted deviation (MSWD) and probability of fit (P) are indicated. Errors on plateau ages are quoted at 2σ and do not include systematic errors (*i.e.*, uncertainties on the age of the monitor and on the decay constant). These plots are obtained at Curtin University within the Western Australian Argon Isotope Facility (WAAIF) of the John de Laeter Centre using ARGUS VI and MAP 215–50 mass spectrometers.
Abbreviations: gm = groundmass; bt = biotite; san = sanidine; fsp = feldspar; pl = plagioclase; amph = amphibole. **[2 pages, 2 columns fitting]**

Figure 6. $^{39}Ar/^{40}Ar$ *vs.* $^{36}Ar/^{40}Ar$ plot and $^{40}Ar/^{39}Ar$ apparent age and K/Ca spectra, plotted against the cumulative percentage of ^{39}Ar released for VVP rocks analysed at University of Vermont. The mini–plateau age is inverse isochron intercept ($^{40}Ar/^{39}Ar$) corrected and indicated in italics. Mean square weighted deviation (MSWD) and probability of fit (P) are reported. Error on the plateau age is quoted at 2σ. These plots are obtained at the Noble Gas Geochronology Laboratory of the University of Vermont with Nu Instruments Noblesse magnetic sector noble gas mass spectrometer.
Abbreviations: gm = groundmass. **[1 column fitting]**

10. DISCUSSION

10.1 Temperature and pressure of mineral crystallization

Crystallization temperature and pressure are calculated mainly through analysis of mineral and whole rock pairs using the recent Fe–Mg cation exchange reaction [$Kd_{Fe-Mg} = (Fe^{clinopyroxene}/Fe^{melt}) \times (Mg^{melt}/Mg^{clinopyroxene})$; Table 5] (Putirka, 2008; Neave and Putirka, 2017). For each VVP district, we used equilibrium clinopyroxene–melt pairs having pyroxene–melt Kd_{Fe-Mg} close to 0.27 ± 0.03, as indicated by Putirka et al. (2003). Futhermore, the difference between predicted and observed diopside+hedenbergite (DiHd) values should approach zero as indicated by Neave and Putirka (2017; see also Putirka et al., 2009) and Mollo et al. (2013; 2017). Calculated clinopyroxene crystallization temperatures and pressure for all VVP districts are reported in Table 5 and in Figure 7. For Val d'Adige, Lessini Mts, and Marosticano calculated temperature ranges are similar (Val d'Adige: T = 1142°C – 1174°C; Lessini Mts. T = 1148 – 1204 °C; Marosticano: T = 1209 – 1219°C; Table 5; Fig. 7) and higher than those for Euganean Hills (T = 1129 – 1162°C; Table 5; Fig. 7). Lessini Mts. clinopyroxene-melt pairs record the highest pressure values (P = 0.4 – 0.8 GPa; Table 5; Fig. 7), while those from the Euganean Hills are the lowest (P = 0.1 – 0.4 GPa; Table 5; Fig. 7). Val d'Adige and Marosticano clinopyroxenes record narrow pressure ranges (Val d'Adige: P = 0.3 – 0.6 GPa; Marosticano: P = 0.5 – 0.6; Table 5; Fig. 7)

It is interesting to note that several of the investigated rocks (*e.g.*, samples BOL1, LB1, and 25B) contain small fragments of mantle peridotite xenoliths, implying that magmas rose rapidly from the mantle to the surface. Therefore, it can be proposed that the highest calculated pressure, measured in Lessini Mts. (~ 0.8 GPa) likely corresponds to the topmost mantle and can be used to infer the depth of the Moho during the VVP activity. Hence, the estimated depth of the Moho under the magmatic region is ~ 26 km, in accordance with geophysical data indicating relatively thin continental crust of ~ 28 km under the VVP (Ansorge et al., 1992; Giese and Buness, 1992; Grad et al., 2009).

	Sample	Lithology	Cpx		Clinopyroxene compositions											Determined pressures and temperatures			
					SiO_2 (wt.%)	TiO_2	Al_2O_3	FeO_{tot}	MnO	MgO	CaO	Na_2O	K_2O	Cr_2O_3	Tot	T (°C) Eqn. 33	P (GPa)	DiHd error	Kd (Fe–Mg)
Val d'Adige																			
	BAL7	Basanite	cpx 1	point 1	47.93	2.25	4.73	6.57	0.06	14.22	22.62	0.36	0.00	0.02	98.76	1142	0.3	0.02	0.28
				point 2	48.20	2.26	4.64	6.39	0.14	14.50	22.50	0.38	0.00	0.03	98.70	1150	0.4	0.01	0.28
			cpx 2	point 1	48.64	2.23	4.35	6.55	0.10	14.46	22.48	0.42	0.00	0.00	99.23	1137	0.3	0.05	0.28
				point 2	47.77	2.34	4.96	6.61	0.12	14.38	22.01	0.37	0.01	0.00	98.57	1167	0.5	–0.01	0.29
				point 3	48.02	2.14	4.91	6.45	0.11	14.46	22.01	0.39	0.01	0.02	98.51	1174	0.6	–0.03	0.29
				point 4	48.49	2.12	4.43	6.22	0.09	14.59	22.42	0.35	0.00	0.00	98.71	1151	0.4	0.00	0.28
Lessini Mts.																			
	TER1	Basalt	cpx 1	point 1	50.29	1.07	3.36	5.15	0.11	15.87	22.73	0.31	0.00	0.39	99.28	1195	0.6	–0.15	0.30
				point 2	50.38	1.12	3.47	5.10	0.11	15.79	23.20	0.31	0.01	0.35	99.83	1185	0.5	–0.14	0.30
				point 3	49.47	1.60	4.26	6.10	0.13	14.92	22.74	0.29	0.00	0.02	99.53	1204	0.7	–0.16	0.30
	BOL1	Basanite	cpx 1	point 1	47.88	1.98	5.32	6.56	0.10	14.35	22.02	0.55	0.00	0.08	98.84	1190	0.8	–0.08	0.30
				point 2	47.92	1.99	4.88	6.14	0.07	14.51	22.58	0.71	0.00	0.00	98.80	1148	0.4	–0.01	0.29
Euganean Hills																			
	EU1AB	Basaltic andesite	cpx 1	point 1	49.14	2.11	4.12	8.65	0.15	14.85	19.88	0.32	0.02	0.49	99.73	1136	0.2	0.03	0.28
			cpx 2	point 1	50.23	1.95	3.18	10.48	0.20	13.16	19.60	0.33	0.01	0.05	99.20	1143	0.3	–0.01	0.28
				point 2	49.68	1.87	2.88	13.71	0.22	11.99	19.18	0.37	0.01	0.05	99.95	1132	0.1	0.02	0.27
			cpx 3	point 1	50.93	1.19	3.61	7.64	0.11	15.40	19.77	0.42	0.01	0.74	99.81	1162	0.4	–0.03	0.28
				point 2	50.09	1.33	3.44	7.45	0.20	15.34	20.23	0.32	0.02	0.73	99.15	1141	0.2	–0.01	0.28
				point 3	50.58	1.43	3.18	8.17	0.14	15.43	20.00	0.31	0.01	0.33	99.58	1141	0.2	0.04	0.27
				point 4	50.34	1.96	3.77	8.85	0.13	14.22	20.34	0.34	0.01	0.22	100.18	1142	0.3	–0.01	0.28

				point 5	49.49	1.88	3.69	9.43	0.17	14.34	19.75	0.30	0.03	0.18	99.26	1140	0.2	–0.01	0.28
				point 6	49.31	2.12	3.65	9.71	0.17	14.08	19.93	0.32	0.00	0.13	99.44	1129	0.1	0.01	0.28
Marosticano																			
	LB1	Basanite	cpx 1	point 1	44.47	3.44	7.56	7.12	0.12	13.08	22.13	0.43	0.00	0.22	98.57	1219	0.6	0.00	0.30
			cpx 2	point 1	49.64	1.08	3.87	5.17	0.08	15.87	22.14	0.52	0.00	0.24	98.61	1209	0.5	–0.05	0.30

Table 5. Clinopyroxene compositions in wt.% from Val d'Adige, Lessini Mts., Euganean Hills, and Marosticano magmatic products and calculated temperatures and pressures using the equation 33 from Putirka (2008) and the equation from Neave and Putirka (2017), respectively. Only clinopyroxenes with the appropriate range in ${}^{cpx/melt}Kd_{Fe–Mg}$ values ($Kd_{Fe–Mg}$ =0.27±0.03; Putirka et al., 2003; Putirka, 2008) and DiHd error ($DiHd_{predicted–observed}$; Neave and Putirka, 2017; Mollo et al., 2013, 2017) approaching zero are presented.
The corresponding whole rock compositions are in Table 1.
Abbreviations: cpx = clinopyroxene; DiHd = Diopside+Hedenbergite solid solution.

Figure 7. Clinopyroxene/melt equilibrium temperatures (°C) and pressures (GPa) of Val d'Adige, Lessini Mts., Euganean Hills, and Marosticano magmatic products calculated from equation 33 of Putirka (2008) and the equation from Neave and Putirka (2017), respectively.

10.2 The mantle source of VVP magmatism

Most analysed magmatic products of the VVP show mg# significantly lower than typical primary magmas (Table 1), *i.e.*, they have undergone at least some fractional crystallization before being erupted to the surface. However, at least a few rocks have mg# higher than 60 and, as mentioned before, host millimeter to centimeter–sized fragments of peridotite xenoliths, which point to fast transport of magma from mantle depths to the surface. Conservatively, we consider only the trace elements contents of the less evolved VVP samples exhibiting MgO > 8 wt.% and mg# > 55 (BAL7, TER1, BOL1, and LB1) to constrain the nature and evolution of their mantle source. The selected samples are characterized by low LILE/HFSE, LREE/HFSE ratios, and high–Nb contents (Fig. 4a, b). Notably, also slightly more evolved basic samples, including those from the Euganean Hills, display similar trace element features. These trace element and REE patterns are clearly distinct from those of the Periadriatic Central Alps calc–alkaline and sub–alkaline products with arc signature (Bergomi et al., 2015; Fig. 4a, b) and are instead consistent with the within–plate signature already noticed by previous studies on the VVP (Milani et al., 1999; Beccaluva et al., 2007; Macera et al., 2008; Fig. 4a, b). In fact, Beccaluva et al., (2001, 2007) invoked an Ocean Island Basalts (OIB)–like mantle source (Sun and McDonough, 1989) for these magmas, justifying the deviations of VVP samples from typical OIB trace element patterns (Fig. 4b), with the identification of a spinel lherzolite enriched with hydrated-carbonated components as potential source. However, large uncertainties were attributed to the mantle region where melting occurred.

Using the geochemical features of the sample suite of this study we determined i) the depth of partial melting; ii) the mineralogical and geochemical features of melting mantle; and iii) the geodynamic evolution that may be responsible for the enrichment/depletion processes in the VVP mantle source region.

10.2.1 The depth of the VVP mantle partial melting

The trace elements patterns and ratios of the selected VVP basic–ultrabasic rocks were at first used to constrain the depth of the VVP mantle source, *i.e.*, if it was in the garnet or in the spinel stability field. The steep middle (M)–HREE profiles of the selected VVP samples suggest a possible presence of garnet in the mantle source, as this mineral progressively takes up the HREE over MREE ($^{garnet/melt}Kd_{Sm}/^{garnet/melt}Kd_{Yb} \sim 10^{-3}$; *e.g.*, van Westrenen et al., 2001; Niu et al., 2011). When garnet is no longer stable, clinopyroxene becomes the sole peridotitic phase that can accommodate REE (Hellebrand et al., 2002). This mineral has an almost equal partition coefficient for MREE and HREE during melting ($^{clinopyroxene/melt}Kd_{Sm}/^{clinopyroxene/melt}Kd_{Yb}$ close 1.0; Green et al., 2000; Niu et al., 2011), imposing melt REE profiles with almost flat M–HREE patterns. Taking this into account, values of $(Sm/Yb)_N$ higher than 1.0 are considered evidence for garnet signature in OIBs (Niu et al., 2011). Such consideration may apply also to VVP basic–ultrabasic samples [$(Sm/Yb)_N$ = 3.9 to 6.1]. Lanthanum is highly incompatible during melting and difficult to accommodate in both garnet and clinopyroxene. This implies that any fertile or moderately fertile mantle source in the early stages of melting, produces melts with positive fractionated REE pattern [$(La/Yb)_N >>1$] in both garnet or spinel stability fields. However, by combining REE ratios such as La/Yb and Dy/Yb, it is possible to constrain the presence or absence of garnet in the mantle source and consequently inferring the melting depth (*e.g.*, Thirlwall et al., 1994). In fact, Dy/Yb is fractionated in the presence of residual garnet and this effect is seen for relatively high degrees of melting (Bogaard and Wörner, 2003). On the contrary, the presence of spinel in the source does not significantly fractionate La, Dy, and Yb as these elements are all moderately incompatible in this mineral. Therefore, in the spinel stability field, La/Yb is only slightly fractionated for small degrees of melting, and Dy/Yb is not fractionated at all (Bogaard and Wörner, 2003).

La/Yb *vs.* Dy/Yb of melts calculated for non-modal batch melting model (Shaw, 1970) are compared to the selected basic–ultrabasic VVP magmatic products (Fig. 8) to confine the chemical composition and mineralogy of the VVP magma source(s), as well as to estimate the degree of partial melting. The calculated melts were obtained for fertile and/or moderately fertile lherzolites (modal clinopyroxene 15–20%; Table 6) with garnet or spinel in the peridotite assemblage. In addition, we modelled also the possible presence of metasomatic phases (i.e, phlogopite and amphibole) in the lherzolitic source. The relative starting and melting modes of (phlogopite-bearing) garnet and (phlogopite-bearing) spinel lherzolites are reported in Table 6. In Figure 8 the selected VVP samples as well as basic–ultrabasic magmatic products from previous studies (Beccaluva et al., 2007) lie closer to the melting curves of the garnet peridotites rather than of the spinel peridotites. In particular, the basanitic samples and the majority of the alkaline primary lavas from Lessini Mts. (data from Beccaluva et al., 2007) cluster around 3–4% of melting of a phlogopite enriched-garnet mantle source. On the other hand, the basalt TER1, which can be classified as tholeiite for its normative character (see Table 1), and the tholeiitic samples from the Lessini Mts. (data from Beccaluva et al., 2007) require slightly higher melting degrees (about 5–6%), and perhaps an anhydrous (*i.e.*, phlogopite and amphibole–free) source.

This melting model and the REE patterns clearly indicate that for the selected samples partial melting occurred dominantly within the garnet–peridotite stability field, i.e., at depths higher than about 70 km (*e.g.*, Green and Ringwood, 1970; Frost, 2008; Ziberna et al., 2013). Geophysical data indicate the depth of lithosphere–asthenosphere boundary under the VVP at ~100km (Panza and Suhaldoc, 1990), therefore we infer that melting occurred within the deep lithosphere. This is also consistent with the inferred presence in the VVP mantle source of phlogopite (see section 10.2.2), a mineral that would rapidly melt out in the asthenospheric mantle wedge (Frost, 2006 and references therein) overlying the subducting European slab.

Unlike VVP basanites and basalt, the calc–alkaline and sub–alkaline basic dykes and intrusive rocks from the Periadriatic Central Alps magmatism exhibit flat HREE profile (Bergomi et al. 2015; Fig. 4a, b) more consistent with a spinel-bearing peridotite. This implies a relatively shallower melting depth for the orogenic compared to the intraplate VVP magmas.

	olivine	orthopyroxene	clinopyroxene	spinel	garnet	phlogopite
Garnet lherzolite						
Mode of the source	0.57	0.16	0.14	—	0.13	—
Melting mode	0.03	0.03	0.44	—	0.50	—
Spinel lherzolite						
Mode of the source	0.56	0.22	0.19	0.03	—	—
Melting mode	0.10	0.20	0.68	0.02	—	—
Phlogopite–bearing garnet lherzolite						
Mode of the source	0.60	0.14	0.15	—	0.03	0.08
Melting mode	0.10	0.10	0.30	—	0.34	0.16
Phlogopite–bearing spinel lherzolite						
Mode of the source	0.58	0.15	0.18	0.03	—	0.06
Melting mode	0.10	0.10	0.54	0.10	—	0.16

Table 6. Source and melting mineral phases used in the non-modal batch model. Mineral modes of garnet lherzolite and spinel lherzolite in primitive mantle are taken from McDonough and Rudnick (1998). Mineral modes of phlogopite-bearing garnet lherzolite and phlogopite-bearing spinel are modified from Pfänder et al. (2018 and reference therein). Values are weight fractions.

Figure 8. Dy/Yb *vs.* La/Yb in selected basic–ultrabasic VVP samples (large symbols) and alkaline and tholeiitic Lessini Mts. magmatic products from Beccaluva et al. (2007; small symbols) having MgO > 8 wt.% and mg# > 55. Also shown are non–modal batch partial melting curves for different mantle sources: i) garnet lherzolite (thick continuous line); ii) spinel lherzolite (thin continuous line); iii) phlogopite–bearing garnet lherzolite (thick dashed line); iv) phlogopite–bearing spinel lherzolite (thin dashed line). The partition coefficients are from GERM (http://earthref.org/). The source and melting mineral modes are reported in Table 6. Mineral modes of garnet lherzolite and spinel lherzolite in primitive mantle are taken from McDonough and Rudnick (1998). Mineral modes of phlogopite-bearing garnet lherzolite and phlogopite-bearing spinel are modified from Pfänder et al. (2018 and reference therein). The source compositions for phlogopite–garnet lherzolite and phlogopite–spinel lherzolite are modified from Pfänder et al. (2018); the source compositions for garnet lherzolite and spinel lherzolite are those of the primitive mantle from McDonough and Sun (1995). Numbers on model curves indicate the percentage of melting.

10.2.2 Is phlogopite really the K (Rb)–bearing residual phase in the VVP mantle source?

Although all the selected basic–ultrabasic samples have potassic affinity, on the primitive–mantle normalized multi–element diagram K and Rb are depleted, whereas Ba is enriched with respect to neighboring elements (Fig. 4b). Such features suggest the presence of a residual K (Rb)–bearing phase (i.e, amphibole and/or phlogopite) in the mantle source region (Greenough et al., 1988; Wilson and Downes, 1992). Previously, we inferred that the partial melting of the VVP mantle source took place probably within the garnet stability field (i.e., at pressures higher than 2.5 GPa; Robinson and Wood, 1998). The stability field of amphibole in upper mantle rocks ranges from 0.5 to 4 GPa at temperatures in the range of 970–1170°C (e.g., Konzett et al., 1997; Frost, 2006; Mandler and Grove, 2016), whereas that of phlogopite ranges from 1 to 9 GPa and temperatures in the range of 800–1500°C (*e.g.*, Sato et al., 1997; Konzett and Ulmer, 1999; Conceição and Green, 2004; Sokol et al., 2017). Therefore, both phases are thus stable at the mantle depths where VVP magmas formed. However, the calculated crystallization temperatures, based on the empirical equation of Putirka (2008) for the clinopyroxene/melt equilibrium, range from ~ 1150 to ~ 1220°C for the selected VVP basanites (Table 5), slightly lower than the temperature of ~ 1250°C obtained by Beccaluva et al. (2007) for the same lithotype. The temperatures of crystallization of the VVP clinopyroxenes are generally above than the stability temperature of amphibole. Taking this into account and considering its chemical–physical properties (Zanazzi and Pavese, 2002; Gemmi et al., 2008; Gatta et al., 2011) phlogopite appears to be the most likely potassic residual mantle phase. The hypothesis of amphibole as residual phase in the VVP mantle source is also ruled out by the REE patterns of VVP samples. Calcic amphiboles have affinity for the MREE (Gd to Ho) relative the HREE (Er to Lu; Tiepolo et al., 2007; Meyzen et al., 2016). Therefore, basanitic melts derived from an amphibole–bearing mantle source are fingerprinted by a typical convex–upward pattern in the MREE (Meyzen et al., 2016), which is absent in the VVP samples. Further evidence for the presence of phlogopite as the K-bearing residual phase is the Ba/Rb ratio. Both Rb and Ba are more compatible in phlogopite ($^{phlogopite/melt}D_{Rb}$ = 1.44, $^{phlogopite/melt}D_{Ba}$ = 1.03; LaTourette et al., 1995; Furman and Graham, 1999; Tiepolo et al.,

2007) than in amphibole ($^{amphibole/melt}D_{Rb}$ = 0.15, $^{amphibole/melt}D_{Ba}$ = 0.29; LaTourette et al., 1995; Furman and Graham, 1999; Schmidt et al., 1999). Considering these partition coefficients, residual amphibole would produce melts enriched in Ba/Rb (> 50), the opposite being true for phlogopite (< 20; Furman and Graham, 1999; Tiepolo et al., 2007; Meyzen et al., 2016). The relatively low Ba/Rb (10 to 20) of most VVP basic–ultrabasic products thus supports the presence of residual phlogopite rather than of amphibole within their mantle source.

10.2.3 The origin of the VVP mantle source enrichment

In the spider diagrams (Fig. 4a, b) as well as to the K and Rb depletions, the basic–ultrabasic VVP magmatic products exhibit enrichments also in Ba, Sr, and P. The same positive anomalies have been described in within–plate magmatic suites generated from an enriched mantle source metasomatized by CO_2–rich fluids, which are able to carry Ba, Sr, and P (Yaxley et al., 1991; Ionov et al., 1996; Beccaluva et al., 2007; Dixon et al., 2008). For example, Merle et al. (2017) suggested that basic–ultrabasic magmatic rocks from Cameroon, which are geochemically characterized by enrichments in LREE, Ba, Sr, and P and depletions in Zr, were derived from a mantle source that underwent metasomatism from carbonatitic melts.

In the case of VVP basic–ultrabasic magmatic rocks, CO_2–rich fluids may have been provided by the subduction of the Tethys oceanic slab, which included calcareous metasediments and carbonated metabasics (Malusà et al., 2018). Following the latter authors, this subduction was “cold” allowing for major amounts of subducted carbonates to survive decarbonation and to be delaminated and stored at depths higher than 180 km, generating a long low velocity layer from Central Southalpine to the Eastern Southalpine domains (Malusà et al., 2018). In fact, according to Maierov et al. (2018) in any collision-subduction process, if the subducted sediments detach from the slab at large depth (> 100 km), their exhumation will be hindered by the thick overlying lithosphere and the subducted materials are forced to flow laterally forming a “long sheet” under the upper plate.

Malusà et al. (2018) proposed that after the slab carbonates emplacement under the Adria microplate lithosphere, their breakdown occurred, due to the progressive rise of mantle temperatures at the slab interface. The new generated carbonate-rich melts, characterized by low density and viscosity (Frezzotti et al., 2009, Malusà et al., 2018), upwelled and infiltrated the overlying (garnet-bearing) mantle domain. These processes possibly involved the mantle source of the VVP.

Several authors (*e.g.*, Aulbach et al., 2004; Su et al., 2010; Meyzen et al., 2016; Sokol et al., 2017) invoked metasomatic processes of silicatic and/or carbonatitic melts and/or fluids to explain the presence of phlogopite in mantle sources. Similarly, we can think that the presence of phlogopite in the VVP mantle source could be responsible for the formation and stabilization of the potassic phase.

To summarize, the trace element data seem to indicate that VVP magmas were derived by partial melting of metasomatized phlogopite–bearing garnet lherzolite (basanitic magmas) and anhydrous garnet lherzolite (tholeiitic magmas). The metasomatic processes occurred at depth with carbonatitic melts. Except for an ancient carbonatitic signature recorded in Marosticano mantle (Brombin et al., 2018), the Val d'Adige and Lessini Mts. mantle peridotites show no evidence for carbonatitic metasomatism. Therefore, we have not enough elements to constrain the age of the carbonatitic metasomatism recorded in the VVP magmatic products. However, according to Beccaluva et al. (2007), the VVP melts are characterized also by low $^{87}Sr/^{86}Sr$ and high $^{144}Nd/^{143}Nd$ isotope ratios, as typical of magmas derived from incompatible element depleted mantle sources. Such decoupling of enrichment in trace elements and depletion in isotopic compositions observed for the VVP magmatic products indicates that the carbonatitic metasomatic event must have occurred recently enough to be unable to significantly affect the isotope composition of the VVP magmas. This consideration emphasizes our suggestion that the infiltration of carbonate fluids in the VVP mantle portion could have occurred after the breakdown of carbonates during the subduction of Tethys oceanic slab.

10.3 The temporal evolution of the magmatic activity of the VVP

For basic–ultrabasic rocks older than Quaternary, the dating of mineral separates is preferred over groundmass for which separation of altered from fresh grains is difficult during sample preparation (Jourdan et al., 2007; Verati and Jourdan, 2013). However, due to the lack of relatively abundant and fresh phenocrysts of K-rich minerals in the VVP basanitic and basaltic samples, groundmass dating was carried out. For these samples, slight alteration is suggested by i) the $^{40}Ar/^{36}Ar$ intercepts substantially lower than atmospheric values for VVP whole–rock data (<298.56 ± 0.31; Table 3; Fig. 5a, c, e, g), ii) the absence of proper plateau ages (i.e., <70% ^{39}Ar released; Tables 3, 4; Fig. 5d, f, h, j, x, 6b, c), and iii) convex K/Ca spectra (Figs. 5b, d, f, h, 6b, d). In view of this, all the obtained mini–plateau ages are considered as minimum crystallization ages. However, the geological significance of these minimum ages is reinforced and confirmed by biostratigraphic data, when available. Therefore, we are confident that the reported whole-rock ages approximately constrain the actual crystallization ages, but we are aware that the true eruption age of a rock that yielded a mini-plateau could lie well outside of the 95% confidence level given by the sample uncertainties. Only Marosticano groundmass data did not define any isochron or plateau ages. However, the age spectra indicating a crystallization age of ~ 22–23 Ma (Figs. 5w, x, 6c, d) are confirmed by biostratigraphic data supporting a late Oligocene to early Miocene eruption in this district. Ages for the Euganean samples were all obtained on mineral separates and are thus of higher quality. All Euganean samples yielded statistically robust plateau ages based on > 88% of gas released (Table 3; Fig. 5l, n, p, r, t, v), only the amphibole separate from EU52 yielded a mini–plateau age (defined by 67% of the released gas; Table 3; Fig. 5j).

Based on the new age determinations and considering the available biostratigraphic data, we reconstructed the temporal evolution of the Cenozoic magmatism occurred in the Southeastern Alpine domain (Fig. 2). The VVP magmatic activity was discontinuous and took place with several pulses, covering a time–span of about 30 My (from late Paleocene to early Miocene). The oldest activity was always subaqueous, thus difficult to date by the $^{40}Ar/^{39}Ar$ technique due to the pervasive alteration of the volcanic products. However, biostratigraphic data constrain the Paleocene onset of VVP magmatism in the Val d'Adige and Lessini Mts., as well as a late Eocene onset in the Euganean Hills (Piccoli et al., 1976, 1981; Savelli and Lipparini, 1979; Luciani, 1989; De Vecchi and Sedea, 1995; Bassi et al., 2008). The oldest age here obtained with the $^{40}Ar/^{39}Ar$ method is Lutetian and is recorded by a basaltic lava flow (TER1≥ 45.21 ± 0.11 Ma; Table 3; Figs. 2, 5e, f) from the Lessini Mts. The basanitic neck of the same district records a quite younger age (BOL1≥ 38.73 ± 0.44 Ma; Bartonian; Table 3; Figs. 2, 5g, h) consistent with its stratigraphic position, cutting the lava flow from which TER1 was collected. The Val d'Adige district records $^{40}Ar/^{39}Ar$ ages similar to those obtained for the Lessini Mts. In particular at Monte Baldo the lava flow (BAL1) and the sill (BAL7) record ages of 41.69 ± 0.37 Ma and 41.98 ± 0.20 Ma, respectively while the basanitic neck near Rovereto (BI14) shows an age of 40.73 ± 0.48 Ma (Tables 3, 4; Figs. 5a–d, 6a, b). These ages are consistent with biostratigraphic ages for the interbedded carbonates (Fig. 2).

All analysed basic to acid Euganean Hills samples yielded indistinguishable ages pointing to a main magmatic phase in this district at ~ 32.21 ± 0.09 Ma (average value). In particular, for the basaltic trachyandesite sample (EU52) both amphibole and plagioclase separates were analysed and the resulting plateau ages are similar (32.35 ± 0.09 Ma and 32.16 ± 0.06 Ma, respectively; Table 3; Fig. 5j, l). The slight difference between the two ages for this sample may be tentatively attributed to the different closure temperatures of these two minerals, i.e., ~ 550 °C for hornblende and ~ 300 °C plagioclase. This would suggest a relatively slow cooling rate (≥1.3°C/Ka) for the EU52 sub–intrusive body. This relatively slow cooling rate of the magma is easily understandable if we consider that EU52 intruded other basic intrusive units, which were probably nearly synchronous and thus still hot. These host basic units are geochemically equivalent to the tholeiitic basaltic products of the Euganean Hills, while EU52 is representative of the basic alkaline products of this district. The plateau age of EU52 overlaps that of the other dated Euganean basaltic trachyandesite (EU8B = 32.17 ± 0.32 Ma; Table 3; Fig. 5n). The plateau ages for the latitic, trachytic, and rhyolitic Euganean samples range between 32.09 ± 0.29 and 32.34 ± 0.51 Ma (Table 3; Fig. 5p, r, t, v). Therefore, according to the new geochronological data the peak phase of both basaltic and acidic Euganean magmatism occurred during the Rupelian (lower Oligocene; Fig. 2) in a time–span possibly shorter than 0.3 My.

Finally, both the Marosticano samples, collected in Monte Gloso quarry, point to an Aquitanian (early Miocene; ~ 22 Ma) eruption age (Table 3; Figs. 2, 5w, x, 6c, d). According to biostratigraphic studies and field evidences, no eruptions occurred during the Miocene neither in Val d'Adige nor in Euganean Hills. Therefore, the Miocene magmatic products of the eastern Lessini Mts. indicated by biostratigraphic data (Savelli and Lipparini, 1979; Fig. 2) and those of the Marosticano district represent the most recent known magmatic activity in the VVP.

The evidence for several VVP magmatic pulses reflects the main extensional phases of the southernmost portion of the Eastern Alps, which were intermitted by episodic accretionary events of the Alpine orogen (Rosenbaum and Lister, 2005). The decompressional melting of the upwelling mantle during extension of continental lithosphere is known as viable mechanism for intraplate magmatism (Pedersen and Ro, 1992). In the Paleocene (65–55 Ma) the Adria–Europe convergence stopped after the continental collision in the Eastern Alps and the following reprise of the convergence was slower than the rollback of the subducting European slab (Stampfli et al., 1998, 2002; Rosenbaum et al., 2002; Dézes et al., 2004; Schmid et al., 2004; Rosenbaum and Lister, 2005). The extension in the overriding plate is promoted when slow convergence rates do not exceed the rates of subduction rollback (Pacanovsky et al., 1999; Jolivet and Faccenna, 2000; Rosenbaum et al., 2002; Heuret and Lallemand, 2005; Rosenbaum and Lister, 2005; Brenna et al., 2015). Therefore, from the Paleocene to the middle Eocene, an extensional regime developed in the Southeastern Alps (Ratschbacher et al., 1989), triggering the magmatism in Val d'Adige (Luciani, 1989; De Vecchi and Sedea, 1995) and in Lessini Mts. (Borsi et al., 1969; Savelli and Lipparini, 1979; Luciani, 1989; De Vecchi and Sedea, 1995; Bassi et al., 2008) along the transtensional fault systems of the Alpone–Agno Graben (Zampieri, 1995). From the late Eocene until ~30 Ma an extensional regime developed in the easternmost VVP parts triggering magmatism also in the Euganean Hills (Piccoli et al., 1976, 1981; Zantendeschi et al., 1994; Milani et al., 1999; Bartoli et al., 2014) and Marosticano (Savelli and

Lipparini, 1979). From ~30 Ma to ~23 Ma (Oligocene-Miocene boundary) the extensional processes stopped in the Southeastern Alps (Frisch et al., 2000). The magmatic activity reprised in the early Miocene, but it was quite rare and limited to the easternmost areas. No magmatic activity younger than ~ 20–23 Ma is documented (Savelli and Lipparini, 1979).

10.4 Geodynamic implications of the magmatism in the VVP

According to the new age determinations, the VVP magmatism ranges from 45.21 ± 0.11 Ma (TER1, Lessini Mts. district) to ~ 22 – 23 Ma (LB1 and 25B, Marosticano district). If we consider also the biostratigraphic evidence for early subacqueous activity in Val d'Adige and Lessini Mts., the VVP magmatism probably started from the late Paleocene (Luciani, 1989; De Vecchi and Sedea, 1995; Bassi et al., 2008). Magmatism in the Central Alps started slightly later, in the Eocene along the Periadriatic/Insubric Line, with the emplacement of the Adamello batholith and its feeder dykes at ~ 42 Ma (Bergomi at al., 2015 and reference therein). However, the climax of the Periadriatic Central Alps orogenic magmatism occurred from 34 Ma to 28 Ma (Bergomi at al., 2015 and reference therein), during the Oligocenic extensional phase that characterized both the Central and the Eastern Alpine domains (Ring, 1994; Nievergelt et al., 1996; Challandes et al., 2003; Glodny et al., 2008; Pleuger et al., 2008; Steck, 2008; Beltrando et al. 2010; Ring and Gerdens, 2016; Schmid et al., 2017). Despite the geographic proximity and despite similar emplacement ages, the Periadriatic Central Alps intrusive bodies and the VVP magmatic products are characterized by quite different geochemical signatures. The first one is characterized by sub–alkaline and calc–alkaline affinities, exhibiting trace element features typical of subduction–related magmas (high LILE/HFSE, high LREE/HFSE ratios, and low–Nb contents; Bellieni, 1980; Bergomi et al., 2015). In particular, the enrichments in LILE, Th and U of the least evolved Periadriatic Central Alps calc–alkaline and sub–alkaline dykes (MgO > 6 wt.% and mg# > 60; Fig. 4b), may result from a mantle source contaminated by subducted and recycled continental material, probably the crystalline basement of the Central Southern Alps (Bergomi et al., 2015; Fig. 4b). Contrarily, the VVP magmas span dominant alkaline to rare subalkaline compositions including ultrabasic, basic, intermediate, and acid rocks, with the least evolved magmatic products exhibiting trace element signature typical of intraplate magmas (*e.g.*, high HFSE contents, high LREE/HREE ratios, and relatively low LILE/HFSE ratios). Nb/La ratio when plotted against MgO concentrations, becomes a good proxy to discriminate between arc or intraplate magmatic affinities (Kay et al., 2006b, 2013; Pallares et al., 2016). Low Nb/La can be associated with an arc–magmatism, while high Nb/La reflects intraplate chemical signature. The Periadriatic Central Alps magmatic products show Nb/La values significantly lower than those of VVP magmatic products (0.14–0.45 *vs.* 0.78–2.08, respectively), confirming a mantle source with an arc affinity for the Periadriatic Central Alps magmatism and a mantle source with an intraplate affinity for the Southeastern Alps (Fig. 9).

Despite the clearly different geochemical compositions of the Periadriatic Central Alps and VVP magmatism, both events were explained by the slab break–off model by several authors (*e.g.*, von Blanckenburg and Davies, 1995; Dal Piaz et al., 2003; Macera et al., 2003; Bergomi et al., 2015). According to this model, at ~ 35 Ma, after the Adria–Europe collision in the Western Alps, the subducting oceanic slab detached from the European margin (von Blanckenburg and Davies, 1995; Stampfli et al., 1998, 2002; Dézes et al., 2004). The break–off of the subducting slab allowed asthenospheric upwelling above the supra–subduction hydrated mantle wedge, causing its melting. The occurrence of high seismic velocity anomalies (i.e., "cold" material) observed on tomographic images lying above the mantle transition zone under the Central Alps has been proposed to represent the detached European slab (*e.g.*, Macera et al., 2003; Piromallo and Morelli, 2003; Giacomuzzi et al., 2011; Zhao et al., 2016). According to these tomographic images, such high velocity anomalies are discontinuous, reflecting gaps larger than 100 km (Lippitsch et al., 2003; Piromallo and Morelli, 2003). The low–velocity anomalies (i.e., "hot" material) below the VVP could be interpreted as mantle diapirs sucked into these lithospheric gaps and upwelled towards shallower levels inducing partial melting of the surrounding subcontinental lithospheric material and providing an intraplate geochemical signature to the VVP magmatic products (Macera et al., 2003). However, the biostratigraphic ages suggest that the Cenozoic magmatism started in the late Paleocene and also our new radioisotopic ages confirm that the peak activity in the Val d'Adige and Lessini Mts. was Eocene in age (~ 45–38 Ma), i.e., it was formed well before the supposed slab break–off event. Therefore, only the Oligocene magmatic activity from the Euganean Hills may be related to slab detachment. Macera et al. (2003) justified the early VVP eruptions (Paleocene) as the result of the mantle diapir action. On the contrary, Bergomi et al. (2015) proposed a partial melting of supra–subduction mantle wedge in the VVP area in response to the low–angle Alpine subduction that shifted the magmatism into the foreland.

Recent high–resolution P wave isotropic tomography (Zhao et al., 2016) and the first P wave anisotropic tomography of the Alps performed (Hua et al., 2017), allow reconstructing the complex mantle structure and dynamics of the Alps and adjacent regions. Isotropic tomography simply provides snapshots of the present crust and upper mantle structures beneath the Alps (Zhao et al., 2016; Hua et al., 2017). On the contrary, seismic anisotropy is produced by the preferred orientation of olivine crystals induced by mantle flow (*e.g.*, Savage, 1999; Savage and Sheehan, 2000; Park and Levin, 2002; Lucente et al., 2006; Savage et al., 2016). Therefore, it reveals information on the actual upper mantle flow field (Long and Silver, 2008; Hua et al., 2017). These new images document a continuous European slab beneath the Central Alps without evidence of any gaps down to 450 km in depth, which rules out the hypothesis of the slab break–off as a viable mechanism for the Cenozoic magmatism in the Alps. In particular, the length of the subducted slab in the Central Alps ranges from 450 to 500 km (Hua et al., 2017), which is in accordance with the estimation of the length of a hypothetical continuous subducting slab below the Central Alps and contrasts with the more reduced slab length of 300 km estimated by Piromallo and Faccenna (2004) that was taken as evidence of slab break–off.

Futhermore, Freeburn et al. (2017) showed by numerical modelling that magmatism induced by slab break–off occurs only when the latter is shallower than the base of the overriding lithosphere. Such processes are not common as slab break–off occurs typically deeper than the overriding plate thickness (Duretz et al., 2011; van Hunen and Allen, 2011; Freeburn et al., 2017), too deep to generate any decompressional melting of dry upwelling asthenosphere or sufficient thermal perturbations within the overriding lithosphere. These new results allow reconsidering the mechanism generating the magmatic processes in the VVP. In particular, in the frame of our new geochronological results and source modelling, the tomographic results of Zhao et al. (2016) and Hua et al. (2017) provide elements for also an alternative model to explain the Alpine geodynamics. Since the continental collision in the Eastern Alps (65 Ma), the European slab became not only progressively steeper, but also retreated in response to rollback mechanisms (Stampfli et al., 1998, 2002; Rosenbaum et al., 2002; Dézes et al., 2004; Schmid et al., 2004; Rosenbaum and Lister, 2005; Singer et al., 2014; Bergomi et al., 2015; Schlunegger and Kissling, 2015, Kissling and Schlunegger, 2018).

Laboratory analogue solutions, 3D experiments, and numerical modelling reproducing the retreating slab movements show that the rollback subduction generates a complex mantle circulation pattern characterized by the presence of poloidal and toroidal mantle flows, escaping from beneath the slab and upwelling from the tip and the lateral edges of the sinking plate, respectively (Fig. 10a; Kincaid and Griffiths, 2003; Funiciello et al., 2006; Piromallo et al., 2006; Faccenna et al., 2011, Strak and Schellart, 2014). The poloidal mantle flow can affect areas located far away from the trench, while the toroidal flow produces upwellings located only slightly laterally away from the sub–slab domain (Fig. 10a; Strak and Schellart, 2014). However, the mantle circulation is intermittent: when the slab approaches the upper/lower mantle discontinuity at 660 km, the poloidal circulation reduces significantly, as the slab represents a barrier for material exchange in vertical direction, whereas the toroidal mantle motion is particularly vigorous (Kincaid and Griffiths, 2003; Funiciello et al., 2006; Faccenna et al., 2011; Chen et al., 2016). Irrespective of the dominant component (poloidal or toroidal), the subduction–induced mantle flow i) drives deformation, mainly extensional, in the overriding plate (Chen et al., 2016) and ii) triggers volcanism induced by decompressional melting (Faccenna et al., 2011).

Taking all of this into account, we speculate that within the Alpine geological setting, the progressive retreat of the European slab caused upwelling of a subduction–induced mantle flow (Fig. 10). This was probably mainly poloidal, as the European slab tip is presently at ~ 450 km (Hua et al., 2017), still far from the 660 km discontinuity. The circulation of this mantle flow could be also the cause of the rising temperature at the slab interface, responsible for the breakdown of the subducted carbonates stored at depth higher than 180 km. Then the carbon–rich melts infiltrated and metasomatized the overlying mantle lithosphere or the mantle wedge. The mantle flow upwelling induced also extensional deformation in the overriding plate and decompressional melting of the phlogopite–bearing and anhydrous (i.e., phlogopite and amphibole–free) garnet lherzolite sources metasomatized by CO_2–rich melts. This process triggered magmatism with intraplate signature instead of arc affinity (Fig. 10). The VVP magmatism occurred in the Paleocene–Eocene in the westernmost side (i.e., Val d'Adige–Lessini Mts. domain) and only since the Oligocene in its eastern areas (i.e., Euganean Hills–Marosticano domain). The southeastward migration and rejuvenation of the magmatism can be accounted for considering that Adria microplate underwent counterclockwise rotation of the order of 40–50° since ~ 35 Ma (Lowrie and Alvarez, 1975; Dewey et al., 1989; Rosenbaum et al., 2002; Ring and Gerdens, 2016). Such movement could have controlled the asthenospheric upwelling to affect different portions of the overlying lithosphere.

In this work, we ruled out the need of passive upwelling of mantle flow through slab window(s) to explain the occurrence of the VVP magmatism. Although this was not the aim of this work, in the frame of the geodynamic model we also speculate that the Periadriatic orogenic magmatism in Central Alps is related to the dehydration of the subducting oceanic slab, which triggerred the partial melting of the overlying spinel-bearing mantle wedge (Fig. 10).

Figure 9. MgO (wt.%) *vs.* Nb/La diagram showing arc (grey field) and intraplate (coulored fields) affinities of mantle sources for Val d'Adige, Lessini Mts., Euganean Hills, and Marosticano rocks studied in this work (large symbols) and in previous studies (small symbols delimiting fields). Val d'Adige compositions are from Beccaluva et al., (2007); Lessini Mts. and Marosticano compositions are from Macera et al. (2003) and Beccaluva et al. (2007); Euganean Hills compositions are from Macera et al. (2003) and Milani et al. (1999). **[1 column fitting]**

Figure 10. Schematic model (not in scale) for magmatism in the Central and Southeastern Alpine domains at Eocene/Oligocene. The slab rollback and steepening of the subducted European slab induced the upwelling of a poloidal mantle flow, which causes i) the breakdown of carbonates in calcareous metasediments and carbonated metabasics dragged at depth by the subducting slab (*i.e.* Malusà et al., 2018); ii) extensional deformation within the Adria microplate, and iii) melting of the carbonatitic metasomatized phlogopite–bearing and anhydrous (i.e., phlogopite and amphibole-free) garnet-peridotite sources, which generated the basanitic and the tholeiitic magmas, respectively. In the Central Alps domain, the dehydration of the subducting oceanic slab induced partial melting of the overlying spinel-bearing mantle wedge, which triggered the Periadriatic orogenic magmatism. Inset a) Sketch showing the paths of poloidal and toroidal mantle flows. The poloidal mantle flow escapes from beneath the slab and upwells from its tip, affecting mantle region(s) located far away from the sinking plate; the toroidal flow escapes from the lateral edges of the slab and upwells only in the mantle portion(s) near the slab. **[2 columns fitting]**

11. CONCLUSION

For this work new geochemical and geochronological data are provided to investigate the occurrence of the intraplate magmatism of VVP, which emplaced in an extensional setting (inferred depth Moho: ~ 26 km) at the same time of the Alpine orogeny.

The geothermobarometric and geochemical data of basanitic magmatic products are consistent with ~ 3–4% degree of partial melting of a phlogopite–bearing garnet peridotite mantle source and those of tholeiitic magmatic products are consistent with ~ 5–6% degree of partial melting of an anhydrous (i.e, phlogopite and amphibole-free) garnet peridotite mantle source. All basic–ultrabasic VVP magmatic products exhibit enrichments in Ba, Sr, and P, indicating that the mantle sources could be metasomatized by carbonatitic melts, maybe provided by the breakdown of carbonates in calcareous metasediments and carbonated metabasics dragged at depth by the subducting Tethys slab.

By integrating literature biostratigraphic data with new $^{40}Ar/^{39}Ar$ geochronological data of the VVP magmatic products, we reconstructed the temporal evolution of the magmatic activity of this province. In the Paleocene–Eocene the first magmatic activities occurred in the westernmost VVP domain (i.e., Val d'Adige and Lessini Mts.) when an extensional regime was imposed in the Southeastern Alps by the rollback of the subducted oceanic slab. During the Oligocene–Miocene another extensional phase occurred promoting the magmatic activities also in the easternmost VVP domain (i.e., Euganean Hills and Marosticano districts). According to this reconstruction the first VVP eruptions are pre–Oligocene in age, ruling out the hypothesis that the magmatism was due to the upwelling of mantle diapirs through a slab window after the European slab detachment, which occurrence was dated after ~ 35 Ma. Moreover, in accordance with new tomographic images, the present European slab is continuous and nearly vertical, with a tip at ~ 450 km in depth, as expected for a hypothetical continuous subducting slab in the Central Alps. Therefore, in this study a new geodynamic model is proposed:

the progressive retreatment and steepness of the European slab induced the escape of the sub–slab mantle material and its upwelling mainly from the front the slab. The subduction–induced mantle flow caused the increasing temperature at the slab interface and, by consequence, the generation of the metasomatizing CO_2–rich melts after the breakdown of carbonates dragged at depth by the subducting Tethys. The upwelling of the mantle flow also caused the intraplate magmatism in the Alpine collisional setting driving i) extensional deformation in Adria microplate and ii) decompression melting of the carbonatitic metasomatized mantle wedge beneath the VVP. It is also speculated that the migration and rejuvenation of the magmatism southeastward is an effect of the Adria counterclockwise rotation, which started ~ 35 Ma. Finally, we suggest that the coeval Periadriatic orogenic magmatism occurred in the Central Alps is related to the partial melting of the spinel-bearing mantle wedge induced by dehydration of the subducting slab.

ACKNOWLEDGMENTS

We thank Renzo Tassinari of University of Ferrara and Daria Pasqual of University of Padova for XRF and ICP–MS analyses; Roberto Zorzin for field work and logistical contributions; Adam Frew and Celia Mayers of WAAIF, and Dan Jones of University of Vermont for their assistance during sample preparation and geochronological analyses.

Field and laboratory work for this project were supported by the Museo Civico di Storia Naturale di Verona and Regione Veneto.

FUNDING

V. Brombin was funded by IUSS Mobility Research Programme (VB scholarship for Abroad Mobility for Long Period 04/11/2015) and Young Researcher Grant of the University of Ferrara (Italy) (Pr. No. 101908)

C. Bonadiman and A. Marzoli were funded by the Italian Government PRIN 2015–2016 funds (Pr. No. 20158A9CBM).

REFERENCES

Alagna, K.E., Peccerillo, A., Martin, S., 2010. Tertiary to present evolution of Orogenic magmatism, in Italy. J. Virt. Expl. 36: paper 18, in: Beltrando, M., Peccerillo, A., Mattei, M., Conticelli, S., Doglioni C., (Eds.), The geology of Italy: tectonics and life along plate margins, 2010.

Aldanmaz, E., Köprüba□i, N., Gürer, Ö.F., Kaymakçi, N., Gourgand A., 2006. Geochemical constraints on the Cenozoic, OIB–type alkaline volcanic rocks of NW Turkey: Implications for mantle sources and melting processes. Lithos 86, 50–76. https://doi.org/10.1016/j.lithos.2005.04.003.

Allen, M.B., Kheirkhah, M., Neill, I., Emami, M.H., McLeod, C.L., 2013. Generation of arc and within-plate chemical signatures in collision zone magmatism: Quaternary lavas feom Kurdistan Province, Iran. J. Petrol. 54, 887-911. https://doi.org/10.1093/petrology/egs090.

Ansorge, J., Blundell, D., and Müller, S., 1992. Europe's lithosphere structure, in: Blundell, D., Freeman, R., Müller, S. (Eds.), A Continent Revealed: The European Geotraverse, New York, Cambridge University Press, p. 275.

Aragón, E., Pinotti, L., D'Eramo, F., Castro, A., Rabbia, O., Coniglio, J., Demartis, M., Hernando, I., Cavarozzi, C.E., Aguilera, Y.E., 2013. The Farallon–Aluk ridge collision with South America: implications for the geochemical changes of slab window magmas from fore– to back–arc. Geoscience Frontiers 4, 377–388. https://doi.org/10.1016/j.gsf.2012.12.004.

Aulbach, S., Griffin, W.L., O'Reilly, S.Y., McCandless, T.E., 2004. Genesis and evolution of the lithospheric mantle beneath the Buffalo Head Terrane, Alberta (Canada). Lithos 77, 413–451. https://doi.org/10.1016/j.lithos.2004.04.020.

Baksi, A.K. 2006. Guidelines for assessing the reliability of $^{40}Ar/^{39}Ar$ plateau ages: application to ages relevant to hotspot tracks. http://www.mantleplumes.org/ArAr.html.

Barbieri, G., De Zanche, V., Sedea, R., 1991. Evoluzione del semigraben paleogenico Alpone–Agno (Monti Lessini). Rendiconti della Società Geologica Italiana 14, 5–12.

Barbieri, G., Medizza, F., 1969. Contributo alla conoscenza geologica della regione di Bolca (Monti Lessini). Mem. Ist. Geol. Min. Univ. Pad. 27, 1–36.

Bartoli, O., Meli, S., Bergomi, M.A., Sassi, R., Magaraci, D., Liu, D.Y., 2014. Geochemistry and zircon U–Pb geochronology of magmatic enclaves in trachytes from the Euganean Hills (NE Italy): further constraints on Oligocene magmatism in the eastern Southern Alps. Eur. J. Mineral. 27, 161–174. https://doi.org/10.1127/ejm/2015/0027–2425.

Bassi, D., Bianchini, G., Mietto, P., Nebelsick, J.H., 2008. Southern Alps: Venetian Pre–Alps, in: McCann T. (Eds.), The Geology of Central Europe, 2. Geol. Soc. London, pp.1087–1092.

Beccaluva, L., Bianchini, G., Bonadiman, C., Coltorti, M., 2007. Intraplate lithospheric and sublithospheric components in the Adriatic domain: Nephelinite to tholeiite magma generation in the Paleogene Veneto Volcanic Province, Southern Alps. Geological Society of America 418, 131–152. https://doi.org/10.1130/2007.2418(07).

Beccaluva, L., Bonadiman, C., Coltorti, M., Salvini, L., Siena, F., 2001. Depletion events, nature of metasomatizing agent and timing of enrichment processes in lithospheric mantle xenoliths from the VVP. J. Petrol. 42, 173–187. https://doi.org/10.1093/petrology/42.1.173.0.

Begemann, F., Ludwig, K.R., Lugmair, G.W., Min, K., Nyquisit, L.E., Patchett, P.J., Renne, P.R., Shih, C.Y., Villa, I.M., Walker, R.J., 2001. Call for an improved set of decay constants for geochronological use. Geochim. Cosmochim. Acta 65, 111–121. https://doi.org/10.1016/S0016–7037(00)00512–3.

Bellieni, G., 1980. The Cima di Villa (Zinsnock) massif: geochemical features and comparisons with the Vedrette di Ries (Rieserferner) pluton (Eastern Alps, Italy). Neu. Jb. Mineral., Abh. 138, 244–258.

Beltrando, M., Lister, G.S., Rosenbaum, G., Richards, S., Forster, M.A., 2010. Recognizing episodic lithospheric thinning along a convergent plate margin: the example of the Early Oligocene Alps. Earth Sci. Rev. 103, 81–98. https://doi.org/10.1016/j.earscirev.2010.09.001.

Bergomi, M.A., Zanchetta, S., Tunesi, A., 2015. The Tertiary dike magmaism in the Southern Alps: geochronological data and geodynamic significance. Int. J. Earth Sci. 104, 449–473. https://doi.org/10.1007/s00531–014–1087–5.

Bogaard, P.J.F., Wörner, G., 2003. Petrogenesis of basanitic to tholeiitic volcanic rocks from the Miocene Vogelsberg, Central Germany. J. Petrol. 44, 569–602. https://doi.org/10.1093/petrology/44.3.569.

Borsi, S., Ferrara, G., Piccoli, G., 1969. Determinazioni col metodo K/Ar dell'età delle eruzioni euganee. Rendiconti della Società Italiana di Mineralogia e Petrologia 25, 27–34.

Brack, P., 1981. Structures in the southwestern border of the Adamello intrusion. Swiss Bull. Mineral. Petrol. 61, 37–50. https://doi.org/10.5169/seals–47129.

Brack, P., 1984. Geologie der Intrusiva und Nebengesteine des Südwest–Adamello (Nord–Italien). Ph.D. thesis, Dissertation ETH. Nr. 7612.

Bradley, D.C., Kusky, T., Heaussler, P.J., Goldfarb, R.J., Miller, M.L., Dumuolin, J.A., Nelson, S.W., Karl, S.M., 2003. Geological signature of early Tertiary ridge subduction in Alaska. Geol. Soc. Am. Spec. 371, 19–49. https://doi.org/10.1130/0–8137–2371–X.19.

Brenna, M., Cronin, S.J., Kereszturi, G., Sohn, Y.K., Smith, I.E.M., Wijbrans, J., 2015. Intraplate volcanism influenced by distal subduction tectonics at Jeju Island, Republic of Korea. Bull. Volcanol. 77, 1–16. https://doi.org/10.1007/s00445–014–0896–5.

Briggs, R.M., McDonough, W.F., 1990. Contemporaneous convergent margin and intraplate magmatism, North island, New Zealand. J. Petrol. 31, 813–851. https://doi.org/10.1093/petrology/31.4.813.

Brombin, V., Bonadiman, C., Coltorti, M., Fahnestock, M.F., Bryce, J.G., Marzoli, A., 2018. Refertilized mantle keel below the Southern Alps domain (North–East Italy): Evidence from Marosticano refractory mantle peridotites. Lithos 300–301, 72–85. https://doi.org/10.1016/j.lithos.2017.11.032.

Callegari, E., Brack, P., 2002. Geological map of the Tertiary Adamello batholith (Northern Italy). Explanatory notes and legend. Memorie Scienze Geologiche 54, 19–49.

Carminati, E., Doglioni, C., 2012. Alps vs. Appennines: the paradigm of a tectonically asymmetric

Earth. Earth Sci. Rev. 112, 67–96. https://doi.org/10.1016/j.earscirev.2012.02.004.

Challandes, N., Marquer, D., Villa, I.M., 2003. Dating the evolution of C–S microstructures: A combined $^{40}Ar/^{39}Ar$ step–heating and UV laserprobe analysis of the Alpine Roffna shear zone. Chem. Geol., 197, 3–19. https://doi.org/10.1016/S0009–2541(02)00354–6.

Chen, Z., Schellart, W.P., Strak, V., Duarte, J.C., 2016. Does subduction–induced mantle flow drive back–arc subduction? Earth Planet. Sci. Lett. 441, 200–210. https://doi.org/10.1016/j.epsl.2016.02.027.

Conceição, R.V., Green, D.H., 2004. Derivation of potassic (shoshonitic) magmas by decompression melting of phlogopite + pargasite lherzolite. Lithos 72, 209–229. https://doi.org/10.1016/j.lithos.2003.09.003.

Conticelli, S., Guarnieri, L., Farinelli, A., Mattei, M., Avanzinelli, R., Bianchini, G., Boari, E., Tommasini, S., Tiepolo, M., Prelevic, D., Venturelli, G., 2009. Trace–elements and Sr–Nd–Pb isotopes of K–rich, shoshonitic, and calc–alkaline magmatism of the Western Mediterranean region: genesis of ultrapotassic to calcalkaline magmatic association in a post–collisional geodynamic setting. Lithos 107, 69–92. https://doi.org/10.1016/j.lithos.2008.07.016.

Cook, C., Briggs, R.M., Smith, I.E.M., Maas, R., 2005. Petrology and geochemistry of intraplate basalts in the South Auckland Volcanic Filed, New Zealand: evidence for two coeval magma suites from distinct sources. J. Petrol. 46, 473–503. https://doi.org/10.1093/petrology/egh084.

Dal Piaz, G.V., Bistacchi, A., Massironi, M., 2003. Geological outline of the Alps. Episodes 26, 175–181.

de Boer, J.Z., Defant, M.J., Stewart, R.H., Restrepo, J.P., Clark, L.F., Ramirez, A.H., 1988. Quaternary calc–alkaline volcanism in western panama: regional variation and implication for the plate tectonic framework. Journal of South American Earth Sciences 1, 275–293. https://doi.org/10.1016/0895–9811(88)90006–5.

De Vecchi, G., Gregnanin, A., Piccirillo, E.M., 1976. Aspetti petrogenetici del vulcanesimo terziario Veneto. Mem. Ist. Geol. Min. Univ. Pad. 30, 1–63.

De Vecchi, G., Sedea, R., 1995. The Paleogene basalts of the Veneto region (NE Italy). Memorie di Scienze Geologiche 47, 253–374.

Dewey, J.F., Helman, M.L., Turco, E., Hutton, D.H.W., Knott, S.D., 1989. Kinematics of the western Mediterranean, in Alpine Tectonics. Geol. Soc. Spec. Publ. London 45, 265–283. https://doi.org/10.1144/GSL.SP.1989.045.01.15.

Dézes, P., Schmid, S.M., Ziegler, P.A., 2004. Evolution of the European Cenozoic Rift System: interaction of the Alpine and Pyrenean orogenes with their foreland lithosphere. Tectonophysics 389, 1–33. https://doi.org/10.1016/j.tecto.2004.06.011.

Dixon, J., Clague, D.A., Cousens, B., Monsalve, M.L., Uhl, J., 2008. Carbonatite and silicate melt metasomatism of the mantle surrounding the Hawaiian plume: evidence from volatiles, trace elements, and radiogenic isotopes in rejuvenated–stage lavas from Niihau, Hawaii. Geochem. Geophys. 9. https://doi.org/10.1029/2008GC002076.

Duretz, T., Gerya, T.V., May, D.A, 2011. Numerical modelling of spontaneous slab breakoff and subsequent topographic response. Tectonophysics 502, 244–256. https://doi.org/10.1016/j.tecto.2010.05.024.

Faccenna, C., Molin, P., Orecchio, B., Olivetti, V., Bellier, O., Funiciello, F., Minelli, L., Piromallo, C., Billi, A., 2011. Topography of the Calabria subduction zone (southern Italy): clues for the origin of Mt. Etna. Tectonics 30, TC1003. https://doi.org/10.1029/2010TC002694

Faccini, B., Coltorti, M., Bonadiman, C., 2018. Contemporaneous emission of calcalkaline and alkaline magmas in subductive geodynamic settings: a mantle xenolith perspective. Book of Abstracts, 3rd European Mantle Workshop – Pavia, 43.

Ferrari, L., 2004. Slab detachment control on mafic volcanic pulse and mantle heterogeneity in central Mexico. Geology 32, 77–80. https://doi.org/10.1130/G19887.1.

Ferrari, L., Petrone, C.M., Francalanci, L., 2001. Generation of oceanic–island basalt–type volcanism in the western Trans–Mexican volcanic belt by slab rollback, asthenosphere infiltration, and variable flux melting. Geology 29, 507–510. https://doi.org/10.1130/0091–7613(2001)029<0507: GOOIBT>2.0.CO;2.

Frascari Ritondale Spano, F., 1969. Serie Paleogeniche nell'area pedemontana a Sud dell'Altopiano di Asiago (Vicenza, Italia) Mémoires du Bureau des Recherches géologiques et Minières 69, 173–182.

Frascari Ritondale Spano, F., Bassani, P., 1973. Ricerche geologiche nei dintorni di Bassano del Grappa (Vicenza). Memorie Museo Trid. Scienze Naturali 19, 65–112.

Freeburn, R., Bouilhol, P., Maunder, B., Magni, V., van Hunen, J., 2017. Numerical models of the magmatic processes induced by slab breakoff. Earth Planet. Sci. Lett. 478, 203–213. https://doi.org/10.1016/j.epsl.2017.09.008.

Frezzotti, M.L., Peccerillo, A., Panza G., 2009. Carbonate metasomatism and CO_2 lithosphere–asthenosphere degassing beneath the Western Mediterranean: an integrated model arising from petrological and geophysical data. Chem. Geol. 262, 108–120. https://doi.org/10.1016/j.chemgeo.2009.02.015.

Frisch, W., Dunkl, I., Kuhlemann, J., 2000. Post–collisional orogen–parallel large–scale extension in the Eastern Alps. Tectnophysics 327, 239–265. https://doi.org/10.1016/S0040–1951(00)00204–3.

Frost, D.J., 2006. The stability of hydrous mantle phases. Rev. Mineral. Geochem. 62, 243–271. https://doi.org/10.2138/rmg.2006.62.11.

Frost, D.J., 2008. The upper mantle and transition zone. Elements 4, 171–176. https://doi.org/10.2113/GSELEMENTS.4.3.171.

Funiciello, F., Moroni, M., Piromallo, C., Faccenna, C., Cenedese, C., Bui, H.A., 2006. Mapping mantle flow during retreating subduction: Laboratory models analysed by feature tracking. J. Geophys. Res. 111, B03402. https://doi.org/10.1029/2005JB003792.

Furman, T., Graham, D., 1999. Erosion of lithospheric mantle beneath the East African Rift system: geochemical evidence from the Kivu volcanic province. Lithos 48, 237–262. https://doi.org/10.1016/S0024–4937(99)00031–6.

Fytikas, M., Innocenti, F., Manetti, P., Peccerillo, A., Mazzuoli, R., Villari, L., 1984. Tertiary to Quaternary evolution of volcanism in the Aegean region. Geol. Soc. Spec. Publ. London 17, 687–699. https://doi.org/10.1144/GSL.SP.1984.017.01.55.

Gasperini, D., Bosch, D., Braga, R., Bondi, M., Macera, P., Morten, L., 2006. Ultramafic xenoliths from the Veneto Volcanic Province (Italy): Petrological and geochemical evidence for multiple metasomatism of the SE Alps mantle lithospere. Geochem. J. 40, 377–404. https://doi.org/10.2343/geochemj.40.377.

Gatta, G.D, McIntyre, G.J., Sassi, R., Rotiroti, N., Pavese, A., 2011. Hydrogen-bond and cation partitioning in muscovite: A single-crystal neutron-diffraction study at 295 and 20 K. Am. Mineral. 96, 34–41. https://doi.org/10.2138/am.2011.3595.

Gavioli, G., 1972. Ricerche stratigrafiche e tettoniche nei dintorni di Malo (Vicenza). Tesi di laurea, Istituto di Geologia Università di Bologna.

Gemmi, M., Merlini, M., Pavese, A., Curetti, N., 2008. Thermal expansion and dehydroxylation of phengite micas. Phys. Chem. Minerals 35, 367–379. https://doi.org/10.1007/s00269-008-0230-x.

Giacomuzzi, G., Chiarabbia, C., De Gori, P., 2011. Linking the Alps and Apennines subduction systems: New constraints revealed by high–resolution teleseismic tomography. Earth Planet. Sci. Lett. 301, 531–543. https://doi.org/10.1016/j.epsl.2010.11.033.

Giese, P., Buness, H., 1992, Moho depth, atlas map 2, in Blundell, D., Freeman, R., and Müller, S. (Eds.), A Continent Revealed: The European Geotraverse: New York, Cambridge University Press, p. 275, scale 1:2,500,000.

Giusberti, L., Del Favero, L., Roghi, G., 2014. The Purga di Bolca–Vegroni sites, in: Papazzoni C.A., Giusberti, L., Carnevale, G., Roghi, G., Bassi, D., Zorzin R. (Eds.), The Bolca Fossil–Lagerstätten: A window into the Eocene World. Rendiconti della Società Paleontologica Italiana 4, pp. 95–103.

Glodny, J., Ring, U., Kühn, A., 2008. High–pressure metamorphism, thrusting, strike–slip and extensional shearing in the Tauern Window, Eastern Alps: All starting at the same time? Tectonics, 27, TC4004. https://doi.org/10.1029/2007TC002193.

Grad, M., Tiira, T., ESC Working Group, 2009. The Moho depth map of the European Plate. Geophys. J. Int. 176, 279–292. https://doi.org/10.1111/j.1365–246X.2008.03919.x.

Green, D.H., Blundy, J.D., Adam, J., Yaxley, G.M., 2000. SIMS determination of trace element partition coefficients between garnet, clinopyroxene and hydrous basaltic liquids at 2–7.5 GPa and 1020–1200°C. Lithos 53, 165–187. https://doi.org/10.1016/S0024–4937(00)00023–2.

Green, D.H., Ringwood, A.E., 1970. Mineralogy of peridotitic compositions under upper mantle conditions. Phys. Earth Planet. Inter. 3, 359–371. https://doi.org/10.1016/0031–9201(70)90076–2.

Greenough J. D., Hayatsu A., Papezik V. S., 1988. Mineralogy, petrology and geochemistry of the alkaline Malpeque Bay sill, Prince Edward Island. Canad. Mineral. 26, 97–108.

Harangi, S., Downes, H., Seghedi, I., 2006. Tertiary–Quaternary subduction processes and related magmatism in the Alpine–Mediterranean region. Geol. Soc. London, Memoirs 32, 167–190. https://doi.org/10.1144/GSL.MEM.2006.032.01.10.

Hellebrand, E., Snow, J.E., Hoppe, P., Hofmann, A.W., 2002. Garnet–field melting and late–stage refertilization in “residual” abyssal peridotites from the Central Indian Ridge. J. Petrol. 43, 2305–2338. https://doi.org/10.1093/petrology/43.12.2305.

Heuret, A., Lallemand, S., 2005. Plate motions, slab dynamics and back–arc deformation. Phys. Earth Planet. Inter. 149, 31–51. https://doi.org/10.1016/j.pepi.2004.08.022.

Hua, Y., Zhao, D., Xu, Y., 2017. P wave anisotropic tomography of the Alps. J. Geophys. Res.: Solid Earth 122, 4509–4528. https://doi.org/10.1002/2016JB013831.

Ionov, D. A., O’Reilly, S. Y., Kopylova, M. G., Genshaft, Y. S., 1996. Carbonate–bearing mantle peridotite xenoliths from Spitsbergen: phase relationships, mineral compositions and trace element residence. Contrib. Mineral. Petrol. 125, 375–392. https://doi.org/10.1007/s004100050229.

Irvine, T.N., Baragar, W.R.A., 1971. A guide to the chemical classification of the common volcanic rocks. Can. J. Earth. Sci. 8, 523–548. https://doi.org/10.1139/e71–055.

Jolivet, L., Faccenna, C., 2000. Mediterranean extension and the Africa– Eurasia collision. Tectonics 19, 1095–1106. https://doi.org/10.1029/2000TC900018.

Jourdan, F., Féraud, G., Bertrand, H., Watkeys, M.K., 2007. From flood basalts to the onset of oceanization: Example from the $^{40}Ar/^{39}Ar$ high–resolution picture of the Karoo large igneous province. Geochem. Geophys. 8, Q02002. https://doi.org/10.1029/2006GC001392.

Kagami, H., Ulmer, P., Hansmann, W., Dietrich, V., Steiger, R.H., 1991. Nd–Sr isotopic and geochemical characteristics of the southern Adamello (Northern Italy) intrusives: implications for crustal versus mantle origin. J. Geophys. Res. 96, 14331–14346. https://doi.org/10.1029/91JB01197.

Kay, S.M., Ardolino, A.A., Gorring, M., Ramos, V., 2007. The Somuncura Large igneous province in Patagônia: interaction of a transient mantle thermal anomaly with a subducting slab. J. Petrol. 48, 43–77. https://doi.org/10.1093/petrology/egl053.

Kay, S.M., Jones, H.A., Kay, R.W., 2013. Origin of Tertiary to Recent EM – and subduction – like chemical and isotopic signatures in Auca Mahuida region (37°–38°S) and other Patagonian plateau lavas. Contrib. Mineral. Petrol. 166, 165–192. http://dx.doi.org/10.1007/s00410–013–0870–9.

Kay, S.M., Mancilla, O., Copeland, P., 2006b. Evolution of the backarc Chachahuén volcanic complex at 37°S latitude over a transient Miocene shallow subduction zone under the Neuquén Basin. Geological Society of America, Special Paper 407, 215–246. https://doi.org/10.1130/2006.2407(10).

Kincaid, C., Griffiths, R.W., 2003. Laboratory models of the thermal evolution of the mantle during rollback subduction. Nature 425, 58–62. https://doi.org/10.1038/nature01923.

Kissling, E., Schlunegger, F., 2018. Rollback ororgeny model for the evolution of the Swiss Alps. Tectonics 37, 1097–1115. https://doi.org/10.1002/2017TC004762.

Konzett, J., Sweeney, R.J., Thompson, A.B., Ulmer, P., 1997. Potassium amphibole stability in the upper mantle: an experimental study in a peralkaline KNCMASH system to 8.5 GPa. J. Petrol. 38, 537–568. https://doi.org/10.1093/petroj/38.5.537.

Konzett, J., Ulmer, P., 1999. The stability of hydrous potassic phases in lherzolitic mantle. An experimental study to 9.5 GPa in simplified and natural bulk compositions. J. Petrol. 40, 629–652. https://doi.org/10.1093/petroj/40.4.629.

LaTourette, T., Hervig, R.L., Holloway, J.R., 1995. Trace element partitioning between amphibole, phlogopite, and basanite melt. Earth Planet. Sci. Lett. 135, 13–30. https://doi.org/10.1016/0012–821X(95)00146–4.

Le Maitre, R.W., Streckeisen, A., Zanettin, B., Le Bas, M.J., Bonin, B., Bateman, P. Bellieni, G., Dudek, A., Efremova, S., Keller, J., Lamere, J., Sabine, P.A., Schmid, R., Sorensen, H., Woolley, A.R. 2002. Igneous Rocks: A Classification and Glossary of Terms, Recommendation s of the International Union of Geological Sciences Subcommission of the Systematics of Igneous Rocks, ed. Cambridge University Press, UK.

Lee, J.Y., Marti, K., Severinghaus, J.P., Kawamura, K., Yoo, H.–S., Lee, J.B., Kim, J.S., 2006. A redetermination of the isotopic abundance of atmospheric Ar. Geochim. Cosmochim. Acta 70, 4507–4512. https://doi.org/10.1016/j.gca.2006.06.1563.

Lippitsch, R., Kissling, E., Ansorge, J., 2003. Upper mantle structure beneath the Alpine orogen from high–resolution teleseismic tomography. J. Geophys. Res. 108(B8), 2376. https://doi.org/10.1029/2002JB002016.

Long, M.D., Silver, P.G. 2008. The subduction zone flow field from seismic anisotropy: A global view. Science 319, 315–318. https://doi.org/10.1126/science.1150809.

Lowrie, W., Alvarez, W., 1975. Paleomagnetic evidence for rotation of the Italian Peninsula. J. Geophys. Res. 80, 1579–1592. https://doi.org/10.1029/JB080i011p01579.

Lucente, F.P., Margheriti, L., Piromallo, C., Barruol, G., 2006. Seismic anisotropy reveals the long route of the slab through the western–central Mediterranean mantle. Earth Planet. Sci. Lett. 241, 517–529. https://doi.org/10.1016/j.epsl.2005.10.041.

Luciani, V., 1989. Stratigrafia sequenziale del Terziario nella Catena del Monte Baldo (Provincie di Verona e Trento). Memorie di Scienze Geologiche 41, 263–351.

Macera, P., Gasperini, D., Piromallo, C., Blichert–Toft, J., Bosch, D., Del Moro, A., Martin, S., 2003. Geodynamic implications of deep mantle upwelling in the source of Tertiary volcanics from the Veneto region (Southern–Eastern Alps). J. Geodyn. 36, 563–590. https://doi.org/10.1016/j.jog.2003.08.004.

Macera, P., Gasperini, D., Ranalli, G., Mahatsente, R., 2008. Slab detachment and mantle plume upwelling in subduction zones: an example from the Italian South–Eastern Alps. J. Geodyn. 45, 32–48. https://doi.org/10.1016/j.jog.2007.03.004.

Maierov, P., Schulmann, K., Gerya, T., 2018. Relamination styles in collisional orogenes. Tectonics 37, 224–250. https://doi.org/10.1002/2017TC004677.

Malusà, G.M., Frezzotti, M.L., Ferrando, S., Brandmayr, E., Romanelli, F., Panza, G.F., 2018. Active carbon sequestration in the Alpine mantle wedge and implications for long–term climate trends. Sci. Rep. 8, 1–8. https://doi.org/10.1038/s41598–018–22877–7.

Mandler, B.E., Grove, T.L., 2016. Controls on the stability and composition of amphibole in the Earth's mantle. Contrib. Mineral. Petrol., 171 (8–9). https://doi.org/10.1007/s00410–016–1281–5.

Manzotti, P., Ballèvre, M., Zucali, M., Robyr, M., Engi, M., 2014. The tectonometamorphic evolution of the Sesia–Dent Blanche nappes (internal Western Alps): review and synthesis. Swiss J. Geosci. 107, 309–336. https://doi.org/10.1007/s00015–014–0172–x.

McDonough, W.F., Rudnick, R.L, 1998. Mineralogy and composition of the upper mantle. Rev. Mineral. Geochem. 37, 139-164.

McDonough, W.F., Sun, S.S, 1995. The composition of the Earth. Chem. Geol. 120, 223–253. https://doi.org/10.1016/0009–2541(94)00140–4.

McDougall, I., Harrison, TM. 1999. Geochronology and Thermochronology by the $^{40}Ar/^{39}Ar$ method. Oxford University Press, New York.

Medizza, F., 1980. Il giacimento della Purga di Bolca (Verona), in: I vertebrati fossili italiani. Catalogo della Mostra, Verona, pp. 147–148.

Merle, R., Marzoli, A., Aka, F.T., Chiaradia, J.M., Reisberg, L., Castorina, F., Jourdan, F., Renne, P.R., N'ni, J., Nyobe, J.B., 2017. Mt. Bambouto Volcano, Cameroon Line: Mantle source and Differentiation of Within–plate Alkaline Rocks. J. Petrol. 58, 933–962. https://doi.org/10.1093/petrology/egx041.

Meyzen C.M., Marzoli A., Bellieni G., Levresse G., 2016. Magmatic activity on a motionless plate: the case of East Island, Crozet Archipelago (Indian Ocean). J. Petrol. 57, 1409–1436. https://doi.org/10.1093/petrology/egw045.

Milani, L., Beccaluva, L., Coltorti, M., 1999. Petrogenesis and evolution of the Euganean magmatic complex, north eastern Italy. Eur. J. Mineral. 11, 379–399. https://doi.org/10.1127/ejm/11/2/0379.

Mollo, S., Blundy, J.D., Giacomoni, P.P., Nazzari, M., Coltorti, M., Langone, A., Andronico, D., 2017. Clinopyroxene-melt element partitioning during interaction between trachybasaltic magma and siliceous crust: clues from quarzites enclaves at Mt. Etna volcano. Lithos 284-285, 447-461. http://dx.doi.org/10.1016/j.lithos.2017.05.003.

Mollo, S., Putirka, K., Misiti, V., Soligo, M., Scarlato, P., 2013. A new test for equilibrium based on clinopyroxene-melt pairs: clues on the solidification temperatures of Etnean alkaline melts at post-eruptive conditions. Chem. Geol. 352, 92–100. http://dx.doi.org/10.1016/j.chemgeo.2013.05.026.

Morten, L., Taylor, L.A., Durazzo, A., 1989. Spinel in harzburgite and lherzolite inclusions from the San Giovanni Ilarione Quarry, Lessini Mountains, Veneto Region, Italy. Mineral. Petrol. 40, 73–89. https://doi.org/10.1007/BF01162470.

Neave, D.A., Putirka, K., 2017. Clinopyroxene–liquid barometry revisited: magma storage pressures under Icelandic rift zones. Am. Mineral. 102, 777–794. http://dx.doi.org/10.2138/am–2017–5968.

Neumann, F., Vásquez–Serrano, A., Tolson, G., Negrete–Aranda, R., Contreras, J., 2016. Toroidal, counter–toroidal, and upwelling flow in the mantle wedge of the Rivera and Cocos plates:

implications for IOB geochemistry in the Trans–Mexican Volcanic Belt. Pure Appl. Geophys. 176 , 3395–3417. https://doi.org/10.1007/978–3–319–51529–8_11.

Nievergelt, P., Liniger, M., Froitzheim, N., Mählmann, R., 1996. Early to mid Tertiary crustal extension in the central Alps: The Turba mylonite zone (eastern Switzerland). Tectonics 15, 329–340. https://doi.org/10.1029/93TC02312.

Niu, Y., Wilson, M., Humphreys, E.R., O'Hara, M.J., 2011. The origin of intra–plate ocean island basalts (OIB): the lid effect and its geodynamic implications. J. Petrol. 52, 1443–1468. https://doi.org/10.1093/petrology/egr030.

Oberli, F., Meier, M., Berger, A., Rosenberg. C.L., Gieré, R., 2004. U–Th–Pb and ^{230}Th/^{238}U disequilibrium isotope systematics: precise accessory mineral chronology and melt evolution tracing in the Alpine Bergell intrusion. Geochim. Cosmochim. Acta 68, 2543–2560. https://doi.org/10.1016/j.gca.2003.10.017.

Oostingh, K.F., Jourdan, F., Matchan, E.L., Phillips, D., 2017. Ar/Ar geochronology reveals rapid change from plume–assisted to stress–dependent volcanism in the Newer Volcanic Province, SE Australia. Geochem. Geophys. 18, 1–25. https://doi.org/10.1002/2016GC006601.

Pacanovsky, K.M., Davis, D.M., Richardson R.M., Coblentz, D.D., 1999. Intraplate stresses and plate–driving forces in the Philippine Sea plate. J. Geophys. Res. 104, 1095–1110. https://doi.org/10.1029/98JB02845.

Pallares, C., Quidelleur, X., Gillot, P.Y., Kluska, J.M., Tchilinguirian, P., Sarda, P., 2016. The temporal evolution of back–arc magmas from the Auca Mahuida shield volcano (Payenia Volcanic

Province, Argentina). J. Volcanol. Geotherm. Res. 323, 19–37. https://doi.org/10.1016/j.jvolgeores.2016.04.043.

Panza, G.F., Suhadolc, P., 1990. Properties of the lithosphere in collisional belts in the Mediterranean–A review. Tectonophysics 182, 39–46. https://doi.org/10.1016/0040–1951(90)90340–E.

Papazzoni, C.A., Giusberti, L., Carnevale, G., Roghi, G., Bassi, D., Zorzin, R., 2014. The Bolca Fossil–Lagerstätten: A window into the Eocene World, ed. Rendiconti della Società Paleontologica Italiana 4.

Park, J., Levin, V., 2002. Seismic anisotropy: Tracing plate dynamics in the mantle. Science 296, 485–489. https://doi.org/10.1126/science.1067319.

Pedersen, T., Ro, H.E., 1992. Finite extension and decompression melting. Earth Planet. Sci. Lett. 113, 15–22. https://doi.org/10.1016/0012–821X(92)90208–D.

Pfänder, J.A., Jung, S., Klügel, A., Münker, C., Romer, R.L., Sperner, B., Rohrmüller, J., 2018. Recurrent local melting of metasomatised lithospheric mantle in response to continental rifting: constraints from basanites and nephelinites/melilitites from SE Germany. J. Petrol. 59, 667–694. https://doi.org/10.1093/petrology/egy041.

Piccoli, G., Bellati, R., Binotti, C., Di Lallo, E., Sedea, R., Dal Prà, A., Cataldi, R., Gatto, G.O., Ghezzi, G., Marchetti, N., Bulgarelli, G., Schiesaro, G., Panichi, C., Tongiorgi, E., Baldi, P., Ferrara, G.C., Massari, F., Medizza, F., Iliceto, V., Norinelli, A., De Vecchi, G., Gregnanin, A., Piccirillo, E.M., Sbettega, G., 1976. Il sistema idrotermale euganeo–berico e la geologia dei Colli Euganei. Mem. Ist. Geol. Min. Univ. Pad., 30, 266 pp.

Piccoli, G., Sedea, R., Bellati, R., Di Lallo, E., Medizza, F., Girardi, A., De Pieri, R., De Vecchi, Gp., Gregnanin, A., Piccirillo, E.M., Norinelli, A., Dal Prà, A., 1981. Note illustrative della carta geologica dei Colli Euganei alla scala 1: 25.000. Memorie di Scienze geologiche 34, 523–546.

Piromallo, C., Becker, T.W., Funiciello, F., Faccenna, C., 2006. Three-dimensional instantaneous mantle flow induced by subduction. Geophys. Res. Lett. 33, L08304– https://doi.org/10.1029/2005GL025390.

Piromallo, C., Faccenna, C., 2004. How deep can we find the traces of Alpine subduction?, Geophys. Res. Lett. 31, L06605. https://doi.org/10.1029/2003GL019288.

Piromallo, C., Morelli, A., 2003. P wave tomography of the mantle under the Alpine-Mediterranean area. J. Geophys. Res. 108 (B2), 2065. https://doi.org/10.1029/2002JB001757.

Pleuger, J., Nagel, T.J., Walter, J.M., Jansen, E., Froitzheim, N., 2008. On the role and importance of orogen–parallel and –perpendicular extension, transcurrent shearing, and backthrusting in the Monte Rosa nappe and the Southern Steep Belt of the Alps (Penninic zone, Switzerland and Italy), in: Siegesmund, S., Fügenschuh B., Froitzheim, N. (Eds.). Tectonic aspects of the Alpine–Dinaride–Carpathian System. Geol. Soc. Spec. Publ. London 298, pp. 251–280.

Putirka, K., 2008. Thermometers and Barometers for Volcanic Systems, in: Putirka, K., Tepley, F. (Eds.), Minerals, Inclusions and Volcanic Processes, Rev. Mineral. Geochem., Mineral. Soc. Am., 69, pp. 61–120.

Putirka, K., Kuntz, M., Unruh, D., Vaid, N., 2009. Magma evolution and ascent at the Craters of the Moon and neighboring volcanic fields, southern ID, USA: implications for the evolution of polygenetic and monogenetic fields. J.Petrol., 50, 1639–1665. https://doi.org/10.1093/petrology/egp045.

Putirka, K., Ryerson, F. J., Mikaelian, H., 2003. New igneous thermobarometers for mafic and evolved lava compositions, based on clinopyroxene + liquid equilibria. Am. Mineral., 88, 1542–1554.

Ratschbacher, L., Frisch, W., Linzer, H.G., Merle, O., 1991. Lateral extrusion in the Eastern Alps, Part 2: Structural analysis, Tectonics 10, 257–271. https://doi.org/10.1029/90TC02623.

Ratschbacher, L., Frisch, W., Neubauer, F., Schmid, S.M., Neugebauer, J., 1989. Extension in compressional orogenic belts: the eastern Alps. Geology 17, 404–407. https://doi.org/10.1130/0091–7613(1989)017<0404:EICOBT>2.3.CO;2.

Ring, U., 1994. The kinematics of the late Alpine Muretto fault and its relation to eastward extension and to displacement at the Engadine and Periadriatic lines. Eclog. Geol. Helv. 87, 811–831.

Ring, U., Gerdens, A., 2016. Kinematics of the Alpenrhein–Bodensee graben system in the Central Alps: Oligocene/Miocene transtension due to formation of the Western Alps arc. Tectonics 35, 1367–1391. https://doi.org/10.1002/2015TC004085.

Robinson, J.A.C., Wood, B.J., 1998. The depth of the spinel to garnet transition at the peridotite solidus. Earth Planet. Sci. Lett. 164, 277–284. https://doi.org/10.1016/S0012–821X(98)00213–1.

Rosenbaum, G., Lister, G.S., 2005. The Western Alps from the Jurassic to Oligocene: spatio–

temporal constraints and evolutionary reconstructions. Earth Sci. Rev. 69, 281–306. https://doi.org/10.1016/j.earscirev.2004.10.001.

Rosenbaum, G., Lister, G.S., Duboz, C., 2002. Relative motions of Africa, Iberia and Europe during Alpine orogeny. Tectonophysics 359, 117–129. https://doi.org/10.1016/S0040–1951(02)00442–0.

Rosenberg, C.L., 2004. Shear zones and magma ascent: a model based on a review of the Tertiary magmatism in the Alps. Tectonics 23, TC3002. doi:10.1029/2003TC001526.

Rubatto, D., Gebauer, D., Fanning, M., 1998. Jurassic formation and Eocene subduction of the Zermatt–Saas–Fee ophiolites: implications for the geodynamic evolution of the Central and Western Alps. Contrib. Mineral. Petrol. 132, 269–287. https://doi.org/10.1007/s004100050421.

Sato, K., Katsura, T., Ito, E., 1997. Phase relations of phlogopite with and without enstatite up to 8 GPa: implication to potassic magmatism and mantle metasomatism. Earth Planet. Sci. Lett. 146, 511–526. https://doi.org/10.1016/S0012–821X(96)00246–4.

Savage, M.K., 1999. Seismic anisotropy and mantle deformation: What have we learned from shear wave splitting?, Rev. Geophys. 37, 65–106. https://doi.org/10.1029/98RG02075.

Savage, M.K., Aoki, Y., Unglert, K., Ohkura, T., Umakoshi, K., Shimizu, H., Iguchi, M., Tameguri, T., Ohminato, T., Mori, J., 2016. Stress, strain rate and anisotropy in Kyushu, Japan. Earth Planet. Sci. Lett. 439, 129–142. https://doi.org/10.1016/j.epsl.2016.01.005.

Savage, M.K., Sheehan, A.F., 2000. Seismic anisotropy and mantle flow from the Great Basin to the Great Plains, western United States. J. Geophys. Res., 105, 715–734 https://doi.org/10.1029/2000JB900021.

Savelli, C., Lipparini, E. 1979. Età K/Ar di basalti del vicentino e la scala dei tempi del Paleogene. Bollettino della Società Geologica Italiana 98, 375–385.

Schaltegger, U., Brack, P., Ovtcharova, M., Peytcheva, I., Schoene, B., Stracke, A., Marocchi, M., Bargossi, G.M., 2009. Zircon and titanite recording 1.5 million years of magma accretion, crystallization and initial cooling in a composite pluton (southern Adamello batholith, northern Italy). Earth Planet. Sci. Lett. 286, 208–218. https://doi.org/10.1016/j.epsl.2009.06.028.

Schlunegger, F., Kissling, E. 2015. Slab rollback orogeny in the Alps and evolution of the Swiss Molasse basin. Nat. Commun. 6, 8605, 1–10. https://doi.org/10.1038/ncomms9605.

Schmid, S.M., Fügenschuch, B., Kissling, E., Schuster, R., 2004. Tectonic map and overall architecture of the Alpine orogen. Eclogae Geol. Helv. 97, 93–117. https://doi.org/10.1007/s00015–004–1113–x.

Schmid, S.M., Kissiling E., Diehl, T., van Hinsbergen D.J.J, Molli, G., 2017. Ivrea mantle wedge, arc of the Western Alps, and kinematic evolution of the Alps–Apennines orogenic system. Swiss J. Geosci. 110, 581–612. https://doi.org/10.1007/s00015–016–0237–0.

Schmidt, K.H., Bottazzi, P., Vannucci, R., Mengel, K., 1999. Trace element partitioning between phlogopite, clinopyroxene and leucite lamproite melt. Earth Planet. Sci. Lett. 168, 287–299. https://doi.org/10.1016/S0012–821X(99)00056–4.

Schmitz, M.D., Bowring, S.A., Ludwig, K.R., Renne, P.R., 2003. Comment on “Precise K–Ar, ^{40}Ar–^{39}Ar, Rb–Sr and U–Pb mineral ages from the 27.5 Fish Canyon Tuff reference standard” by M.A. Lanphere and H. Baadsgaard. Chem. Geol. 199, 277–280. https://doi.org./10.1016/S0009–2541(03)00078–0.

Schoene, B., Schaltegger, U., Brack, P., Latkoczy, C., Stracke, A., Günther, D., 2012. Rates of magma differentiation and emplacement in a ballooning pluton recorded by U–Pb TIMS–TEA, Adamello batholith, Italy. Earth Planet. Sci. Lett. 355, 162–173. https://doi.org/10.1016/j.epsl.2012.08.019.

Seghedi I., Mațenco L., Downes H., Mason P.R.D., Szakács A., Pécskay Z., 2011. Tectonic significance of changes in post-subduction Pliocene–Quaternary magmatism in the south east part of the Carpathian–Pannonian Region. Tectonophysics 502, 146–157. https://doi.org/10.1016/j.tecto.2009.12.003.

Shaw, D.M., 1970. Trace element fractionation during anatexis. Geochim. Cosmochim. Acta 34, 237–243. https://doi.org/10.1016/0016–7037(70)90009–8.

Siena, F., Coltorti, M., 1989. Lithospheric mantle evolution: evidences from ultramafic xenoliths in the Lessinean volcanics (Northern Itlay). Chem. Geol. 77, 347–364.

Siena, F., Coltorti, M., 1993. Thermobarometric evolution and metasomatic processes of upper mantle in different tectonic settings: evidence from spinel peridotite xenoliths. Eur. J. Mineral. 5, 1073–1090.

Singer, J., Diehl, T., Hunsen, S., Kissiling, E., Duretz, T., 2014. Alpine lithophere slab rollback causing lower crustal seismicity in northern foreland. Earth Planet. Sci. Lett. 397, 42–56. https://doi.org/10.1016/j.epsl.2014.04.002.

Sokol, A.G., Kruk, A.N., Palyanov, Y.N., Sobolev, N.V., 2017. Stability of phlogopite in ultrapotassic kimberlite–like systems at 5.5–7.5 GPa. Contrib. Mineral., Petrol. 172, 21. https://doi.org/10.1007/s00410–017–1341–5.

Sorbini, L., 1989. I fossili di Bolca. Museo Civico di Storia Naturale di Verona, Verona.

Stampfli, G.M., Borel, G.D., Marchant, R., Mosar J., 2002. Western Alps geological constraints on western Tethyan reconstruction, in: Rosenbaum, G., Lister, G., S., 2002. Reconstruction of the evolution of the Alpine–Himalayan Orogen. J. Virt. Expl. 7, 75–104.

Stampfli, G.M., Mosar, J., Marquer, D., Marchant, R., Baudin, T., Borel, G., 1998. Subduction and obduction processes in the Swiss Alps. Tectonophysics 296, 159–204. https://doi.org/10.1016/S0040–1951(98)00142–5

Steck, A., 2008. Tectonics of the Simplon massif and Lepontine gneiss dome: Deformation structures due to collision between the underthrusting European plate and the Adriatic indenter. Swiss J. Geosci. 101, 515–546. https://doi.org/10.1007/s00015–008–1283–z.

Strak, V., Schellart, W.P., 2014. Evolution of 3–D subduction–induced mantle flow around lateral slab edges in analogue models of free subduction analysed by stereoscopic particle image velocimetry technique. Earth Planet. Sci. Lett. 403, 368–379. . https://doi.org/10.1016/j.epsl.2014.07.007.

Su, B.–X., Zhang, H.–F., Sakyi, P.A., Ying, J.–F., Tang, Y.–J., Yang, Y.–H., Qin, K.–Z., Xiao, Y., Zhao, X.–M., 2010. Compositionally stratified lithosphere and carbonatite metasomatism recorded in mantle xenoliths from Western Qinling (Central China). Lithos 116, 111–128. https://doi.org/10.1016/j.lithos.2010.01.004.

Sun, S.S., McDonough, W.F., 1989. Chemical and isotopic systematics of oceanic basalts: implications for mantle composition and processes, in: Saunders, A.D, Norry, M.J. (Eds)., Magmatism in the Oceanic Basins. Geol. Soc. Spec. Publ. London 42, pp. 313–346.

Thirlwall, M.F., Upton, B.G.J., Jenkins, C., 1994. Interaction between continental lithosphere and the Iceland plume.Sr–Nd–Pb isotope chemistry of Tertiary basalts, NE Greenland. J. Petrol. 35, 839–897. https://doi.org/10.1093/petrology/35.3.839.

Tiepolo, M., Oberti, R., Zanetti, A., Vannucci, R., Foley, S.F., 2007. Trace–element partitioning between amphibole and silicate melt. Rev. Mineral. Geochem. 67, 417–452. https://doi.org/10.2138/rmg.2007.67.11.

van Hunen, J., Allen, M.B., 2011. Continental collision and slab breakoff: a comparison of 3–D numerical models with observations. Earth Planet. Sci. Lett. 302, 27–37. https://doi.org/10.1016/j.epsl.2010.11.035.

van Westrenen, W., Blundy, J.D., Wood, B.J., 2001. High field strength element/rare element fractionation during partial melting in the presence of garnet: implications for identification of mantle heterogeneities. Geochem. Geophys., 2000GC000133. https://doi.org/10.1029/2000GC000133.

Verati, C., Jourdan, F., 2013. Modelling effect of sericitization of plagioclase on the ^{40}K/40Ar and

^{40}K/^{39}Ar chronometers: Implication for dating basaltic rocks and mineral deposits, in: Jourdan, F., Mark, D.F., Verati, C. (Eds.), Advances in ^{40}Ar/^{39}Ar dating: from archaeology to planetary sciences. Geol. Soc. Spec. Publ. London 378, pp. 155–174. https://doi.org/10.1144/SP378.24.

Verma, S.P., 2002. Absence of Cocos plate subduction related basic volcanism in southern Mexico: A unique case on Earth?. Geology 30, 1095–1098. https://doi.org/10.1130/0091–7613(2002)030<1095:AOCPSR>2.0.CO;2.

Visonà, D., Caironi, V., Carraro, A., Dallai, L., Fioretti, A.M., Fanning, M., 2007. Zircon megacrysts from basalts of the Venetian Volcanic Province (NE Italy): U–Pb, oxygen isotopes and REE data. Lithos 94, 168–180. https://doi.org/10.1016/j.lithos.2006.06.007.

von Blanckenburg, F., 1992. Combined high–precision chronometry and geochemical tracing using accessory minerals: applied to the Central-Alpine Bergell intrusion (central Europe). Chem. Geol. 100, 19–40. https://doi.org/10.1016/0009-2541(92)90100-J.

von Blanckenburg, F., Davies, J.H., 1995. Slab breakoff: a model for syncollisional magmatism and tectonics in the Alps. Tectonics 14, 120–131. https://doi.org/10.1029/94TC02051.

Wilson, M., Downes, H., 1992. Mafic alkaline magmatism in the European Cenozoic rift system. Tectonophysics 208, 173–182. https://doi.org/10.1016/0040-1951(92)90343-5.

Winterer, E.L., Bosellini, A., 1981. Subsidence and sedimentation on a Jurassic passive continental margin (Southern Alps, Italy). Bulletin American Association of Petroleum Geologists 65, 394–421.

Yaxley, G.M., Crawford, A.J., Green, D.H., 1991. Evidence for carbonatite metasomatism in spinel peridotite xenoliths from western Victoria, Australia. Earth Planet. Sci. Lett. 107, 305–317.

https://doi.org/10.1016/0012–821X(91)90078–V.

Zampieri, D., 1995. Tertiary extension in the southern Trento Platform, Southern Alps, Italy. Tectonics 14, 645–657. https://doi.org/10.1029/94TC03093.

Zanazzi, P.F., Pavese, A., 2002. Behavior of micas at high pressure and high temperature. Rev. Mineral. Geochem. 46, 98–116. https://doi.org/10.2138/rmg.2002.46.02

Zantendeschi, C., 1994. New Rb–Sr radiometric data from Colli Euganei (North Eastern Italy). Mem. Ist. Geol. Min. Univ. Pad. 46, 17–22.

Zhao, L., Paul, A., Malusà, M.G., Xiaobing, X., Zheng, T., Solarino, S., Guillot, S., Schwartz, S., Dumont, T., Salimbeni, S., Aubert, A., Pondrelli, S., Wang, Q., Zhu, R., 2016. Continuity of the Alpine slab unraveled by high–resolution P wave tomography. J. Geophys. Res.: Solid Earth 121, 8720–8737. https://doi.org/10.1002/2016JB013310.

Ziberna, L., Klemme, S., Nimis, P., 2013. Garnet and spinel in fertile and depleted mantle: insights from thermodynamic modelling. Contri. Mineral. Petrol. 166, 411–421. https://doi.org/10.1007/s00410–013–0882–5.

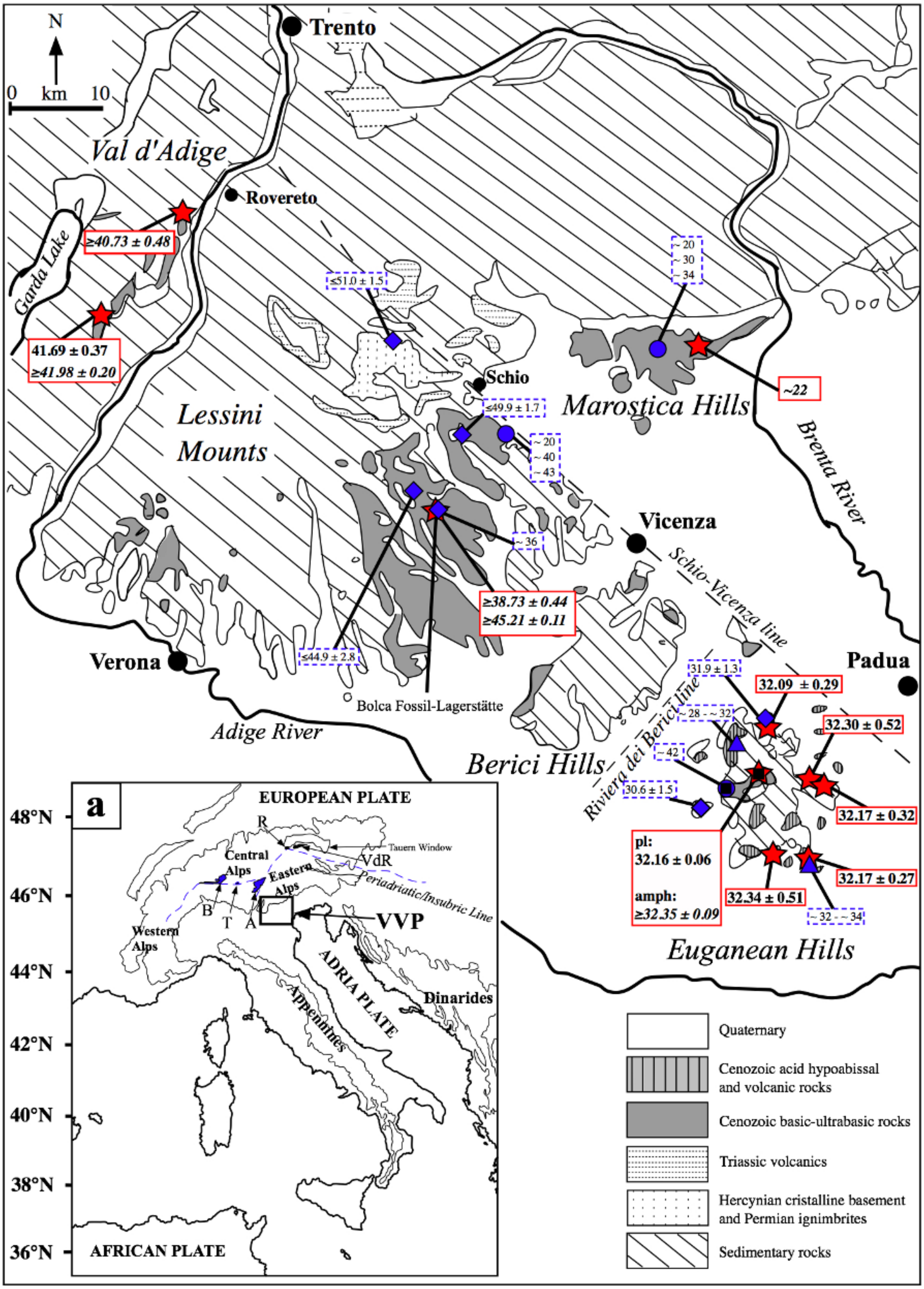

N
0 km 10
Trento
Val d'Adige
Rovereto
Garda Lake
≥40.73 ± 0.48
41.69 ± 0.37
≥41.98 ± 0.20
≤51.0 ± 1.5
Schio
Lessini Mounts
≤49.9 ± 1.7
~ 20
~ 40
~ 43
~ 20
~ 30
~ 34
Marostica Hills
~22
Brenta River
Vicenza
~ 36
≥38.73 ± 0.44
≥45.21 ± 0.11
Schio-Vicenza line
≤44.9 ± 2.8
Verona
Bolca Fossil-Lagerstätte
Adige River
Berici Hills
Padua
31.9 ± 1.3
32.09 ± 0.29
32.30 ± 0.52
~ 28 - ~ 32
~ 42
Riviera dei Berici line
30.6 ± 1.5
32.17 ± 0.32
pl:
32.16 ± 0.06
amph:
≥32.35 ± 0.09
32.34 ± 0.51
32.17 ± 0.27
~ 32 - ~ 34
Euganean Hills
a
EUROPEAN PLATE
R
Tauern Window
VdR
Central Alps
Eastern Alps
Periadriatic/Insubric Line
B
T
A
VVP
Western Alps
ADRIA PLATE
Appennines
Dinarides
AFRICAN PLATE
48°N
46°N
44°N
42°N
40°N
38°N
36°N
Quaternary
Cenozoic acid hypoabissal and volcanic rocks
Cenozoic basic-ultrabasic rocks
Triassic volcanics
Hercynian cristalline basement and Permian ignimbrites
Sedimentary rocks

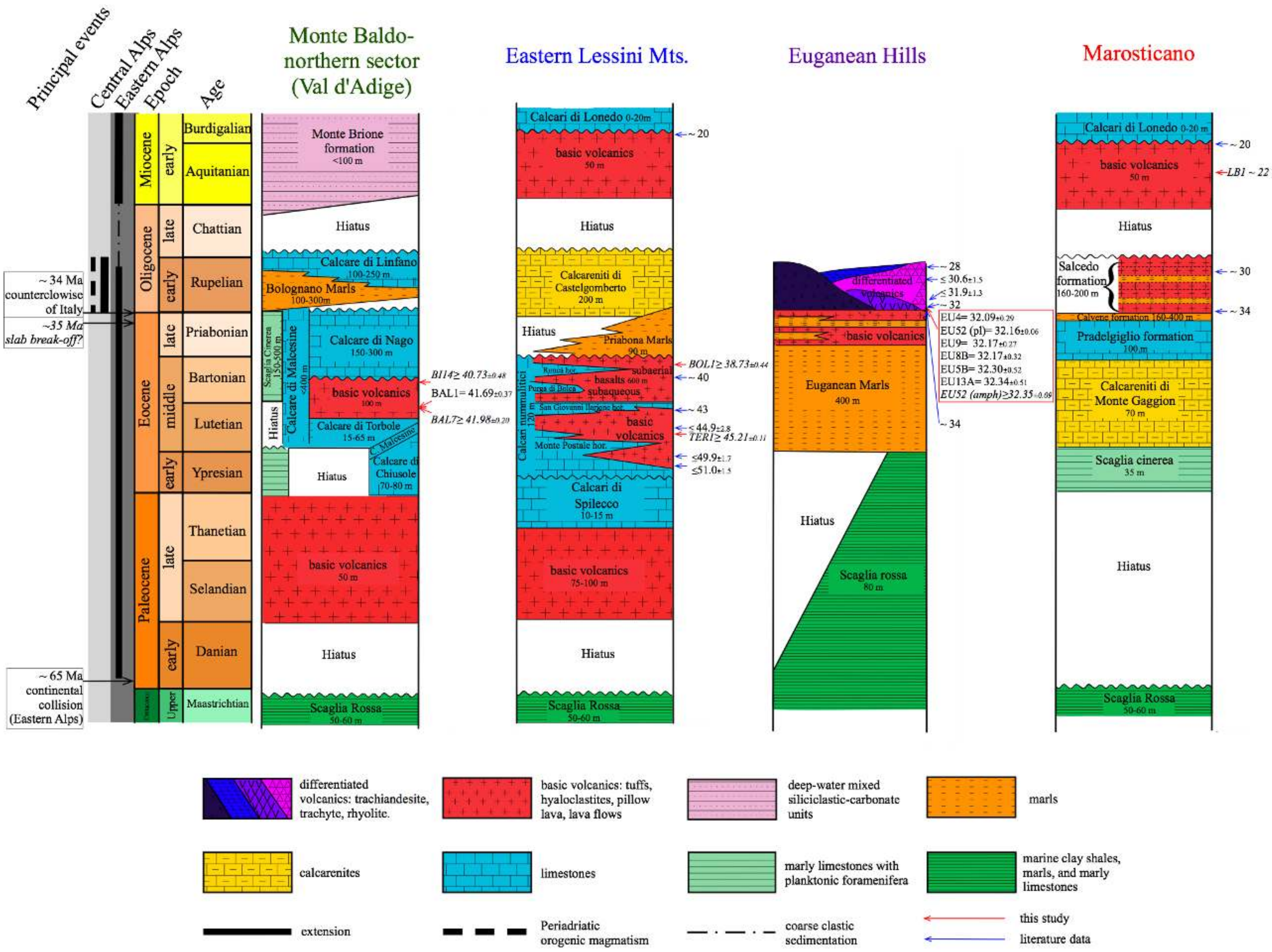

Principal events
Central Alps
Eastern Alps
Epoch
Age
Monte Baldo-northern sector (Val d'Adige)
Eastern Lessini Mts.
Euganean Hills
Marosticano
Miocene
Oligocene
Eocene
Paleocene
early
late
middle
Upper
Burdigalian
Aquitanian
Chattian
Rupelian
Priabonian
Bartonian
Lutetian
Ypresian
Thanetian
Selandian
Danian
Maastrichtian
~ 34 Ma counterclowise of Italy
~35 Ma slab break-off?
~ 65 Ma continental collision (Eastern Alps)
Monte Brione formation <100 m
Hiatus
Calcare di Linfano 100-250 m
Bolognano Marls 100-300m
Scaglia Cinerea 150-500 m
Calcare di Malcesine <400 m
Calcare di Nago 150-300 m
basic volcanics 100 m
Calcare di Torbole 15-65 m
C. Malcesine
Calcare di Chiusole 70-80 m
basic volcanics 50 m
Scaglia Rossa 50-60 m
BI14≥ 40.73±0.48
BAL1= 41.69±0.37
BAL7≥ 41.98±0.20
Calcari di Lonedo 0-20m
basic volcanics 50 m
Calcareniti di Castelgomberto 200 m
Priabona Marls 90 m
Calcari nummulitici 120 m
subaerial basalts 600 m subaqueous
Purga di Bolca
San Giovanni Ilarione hor.
basic volcanics
Monte Postale hor.
Calcari di Spilecco 10-15 m
basic volcanics 75-100 m
Scaglia Rossa 50-60 m
~ 20
BOL1≥ 38.73±0.44
~ 40
~ 43
≤ 44.9±2.8
TER1≥ 45.21±0.11
≤49.9±1.7
≤51.0±1.5
differentiated volcanics
basic volcanics
Euganean Marls 400 m
Scaglia rossa 80 m
~ 28
≤ 30.6±1.5
≤ 31.9±1.3
~ 32
~ 34
EU4= 32.09±0.29
EU52 (pl)= 32.16±0.06
EU9= 32.17±0.27
EU8B= 32.17±0.32
EU5B= 32.30±0.52
EU13A= 32.34±0.51
EU52 (amph)≥32.35±0.09
Calcari di Lonedo 0-20 m
basic volcanics 50 m
Salcedo formation 160-200 m
Calvene formation 160-400 m
Pradelgiglio formation 100 m
Calcareniti di Monte Gaggion 70 m
Scaglia cinerea 35 m
Scaglia Rossa 50-60 m
~ 20
LB1 ~ 22
~ 30
~ 34
differentiated volcanics: trachiandesite, trachyte, rhyolite.
basic volcanics: tuffs, hyaloclastites, pillow lava, lava flows
deep-water mixed siliciclastic-carbonate units
marls
calcarenites
limestones
marly limestones with planktonic foramenifera
marine clay shales, marls, and marly limestones
extension
Periadriatic orogenic magmatism
coarse clastic sedimentation
this study
literature data

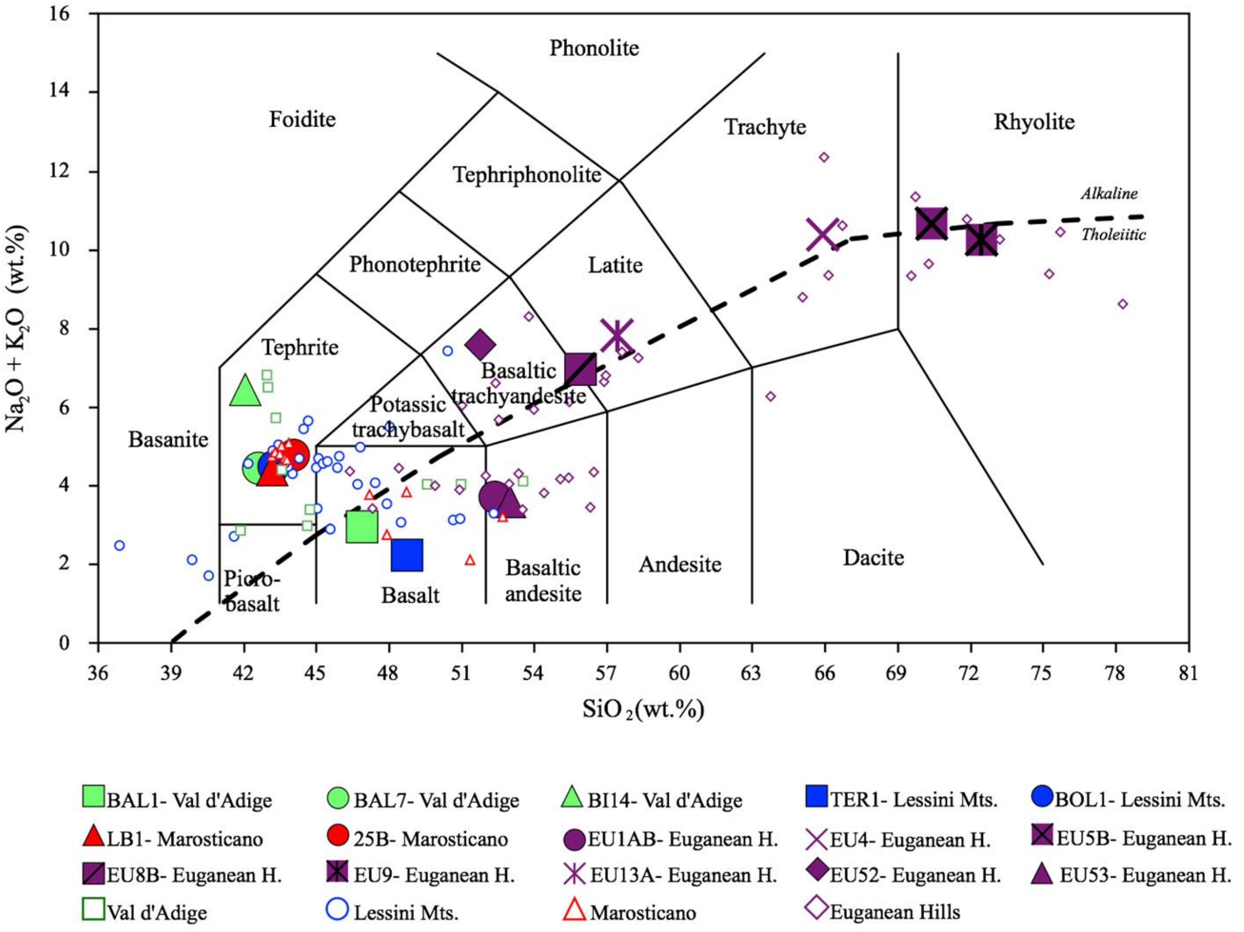

Phonolite
Foidite
Trachyte
Rhyolite
Tephriphonolite
Phonotephrite
Latite
Tephrite
Basaltic trachyandesite
Potassic trachybasalt
Basanite
Picro-basalt
Basalt
Basaltic andesite
Andesite
Dacite
Alkaline
Tholeiitic
$Na_2O + K_2O$ (wt.%)
SiO_2(wt.%)
BAL1- Val d'Adige
BAL7- Val d'Adige
BI14- Val d'Adige
TER1- Lessini Mts.
BOL1- Lessini Mts.
LB1- Marosticano
25B- Marosticano
EU1AB- Euganean H.
EU4- Euganean H.
EU5B- Euganean H.
EU8B- Euganean H.
EU9- Euganean H.
EU13A- Euganean H.
EU52- Euganean H.
EU53- Euganean H.
Val d'Adige
Lessini Mts.
Marosticano
Euganean Hills

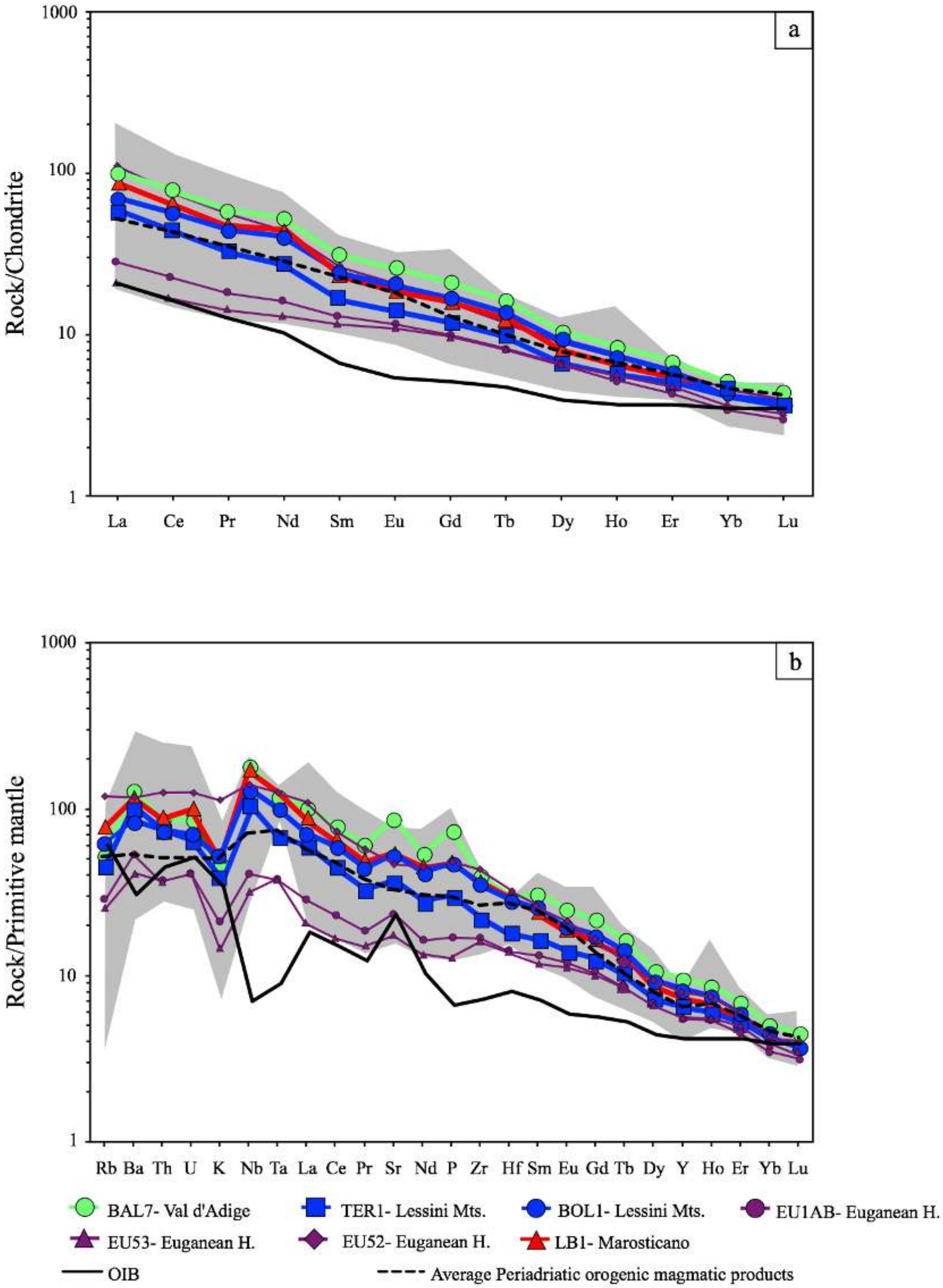

a
Rock/Chondrite
1000
100
10
1
La
Ce
Pr
Nd
Sm
Eu
Gd
Tb
Dy
Ho
Er
Yb
Lu
b
Rock/Primitive mantle
1000
100
10
1
Rb Ba Th U K Nb Ta La Ce Pr Sr Nd P Zr Hf Sm Eu Gd Tb Dy Y Ho Er Yb Lu
BAL7- Val d'Adige
TER1- Lessini Mts.
BOL1- Lessini Mts.
EU1AB- Euganean H.
EU53- Euganean H.
EU52- Euganean H.
LB1- Marosticano
OIB
Average Periadriatic orogenic magmatic products

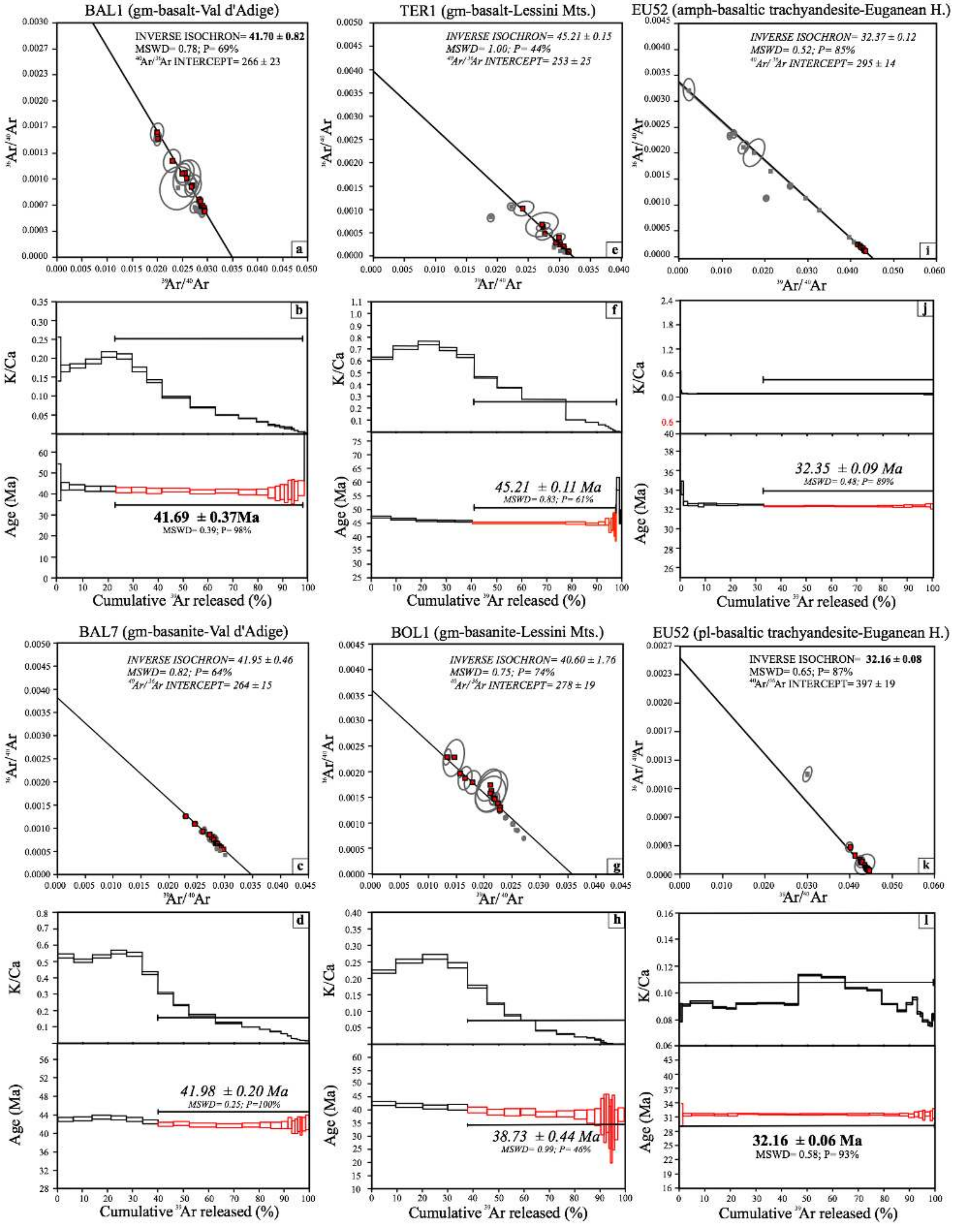
BAL1 (gm-basalt-Val d'Adige)
INVERSE ISOCHRON= 41.70 ± 0.82
MSWD= 0.78; P= 69%
^{40}Ar/^{36}Ar INTERCEPT= 266 ± 23
TER1 (gm-basalt-Lessini Mts.)
INVERSE ISOCHRON= 45.21 ± 0.15
MSWD= 1.00; P= 44%
^{40}Ar/^{36}Ar INTERCEPT= 253 ± 25
EU52 (amph-basaltic trachyandesite-Euganean H.)
INVERSE ISOCHRON= 32.37 ± 0.12
MSWD= 0.52; P= 85%
^{40}Ar/^{36}Ar INTERCEPT= 295 ± 14
^{36}Ar/^{40}Ar
^{39}Ar/^{40}Ar
a
e
i
K/Ca
Age (Ma)
b
f
j
41.69 ± 0.37Ma
MSWD= 0.39; P= 98%
45.21 ± 0.11 Ma
MSWD= 0.83; P= 61%
32.35 ± 0.09 Ma
MSWD= 0.48; P= 89%
Cumulative ^{39}Ar released (%)
BAL7 (gm-basanite-Val d'Adige)
INVERSE ISOCHRON= 41.95 ± 0.46
MSWD= 0.82; P= 64%
^{40}Ar/^{36}Ar INTERCEPT= 264 ± 15
BOL1 (gm-basanite-Lessini Mts.)
INVERSE ISOCHRON= 40.60 ± 1.76
MSWD= 0.75; P= 74%
^{40}Ar/^{36}Ar INTERCEPT= 278 ± 19
EU52 (pl-basaltic trachyandesite-Euganean H.)
INVERSE ISOCHRON= 32.16 ± 0.08
MSWD= 0.65; P= 87%
^{40}Ar/^{36}Ar INTERCEPT= 397 ± 19
c
g
k
d
h
l
41.98 ± 0.20 Ma
MSWD= 0.25; P=100%
38.73 ± 0.44 Ma
MSWD= 0.99; P= 46%
32.16 ± 0.06 Ma
MSWD= 0.58; P= 93%

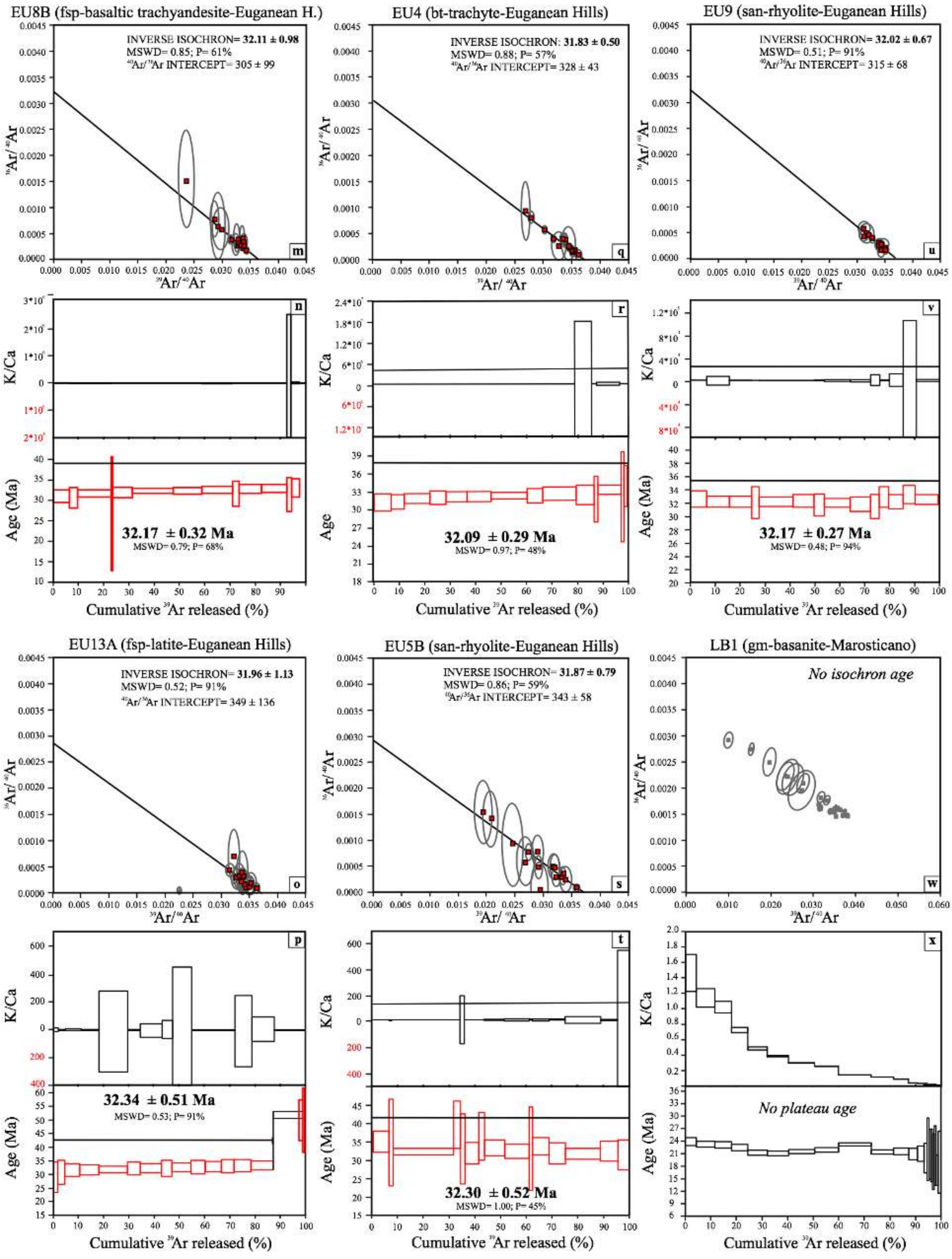
EU8B (fsp-basaltic trachyandesite-Euganean H.)
INVERSE ISOCHRON= 32.11 ± 0.98
MSWD= 0.85; P= 61%
40Ar/36Ar INTERCEPT= 305 ± 99
m
n
32.17 ± 0.32 Ma
MSWD= 0.79; P= 68%
EU4 (bt-trachyte-Euganean Hills)
INVERSE ISOCHRON: 31.83 ± 0.50
MSWD= 0.88; P= 57%
40Ar/36Ar INTERCEPT= 328 ± 43
q
r
32.09 ± 0.29 Ma
MSWD= 0.97; P= 48%
EU9 (san-rhyolite-Euganean Hills)
INVERSE ISOCHRON= 32.02 ± 0.67
MSWD= 0.51; P= 91%
40Ar/36Ar INTERCEPT= 315 ± 68
u
v
32.17 ± 0.27 Ma
MSWD= 0.48; P= 94%
EU13A (fsp-latite-Euganean Hills)
INVERSE ISOCHRON= 31.96 ± 1.13
MSWD= 0.52; P= 91%
40Ar/36Ar INTERCEPT= 349 ± 136
o
p
32.34 ± 0.51 Ma
MSWD= 0.53; P= 91%
EU5B (san-rhyolite-Euganean Hills)
INVERSE ISOCHRON= 31.87 ± 0.79
MSWD= 0.86; P= 59%
40Ar/36Ar INTERCEPT= 343 ± 58
s
t
32.30 ± 0.52 Ma
MSWD= 1.00; P= 45%
LB1 (gm-basanite-Marosticano)
No isochron age
w
x
No plateau age
36Ar/40Ar
39Ar/40Ar
K/Ca
Age (Ma)
Age
Cumulative 39Ar released (%)

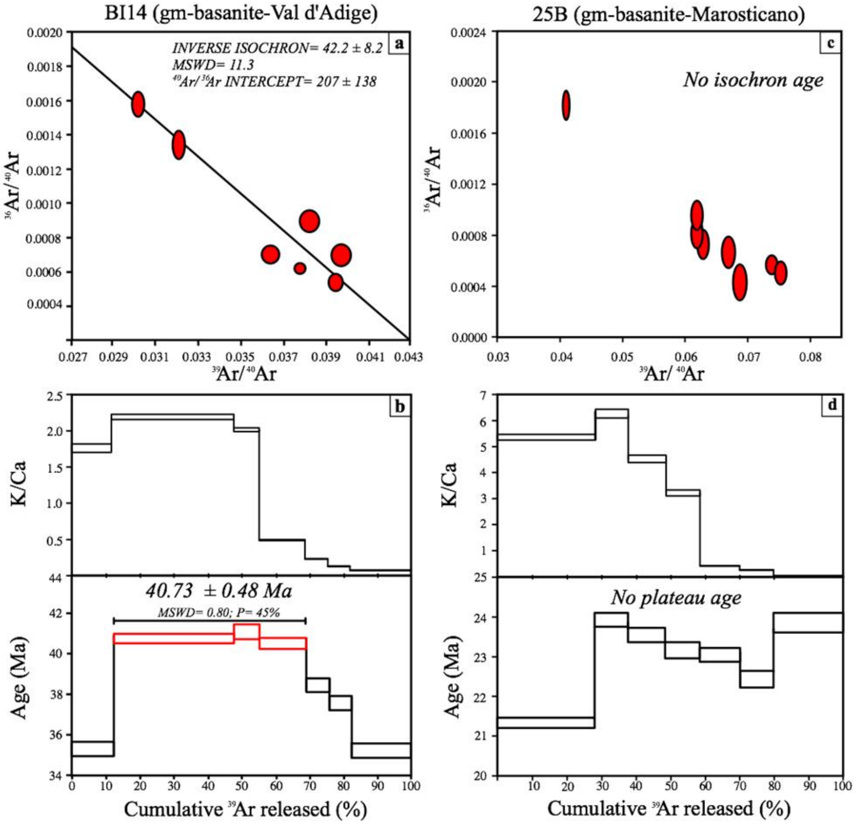

BI14 (gm-basanite-Val d'Adige)
INVERSE ISOCHRON= 42.2 ± 8.2
MSWD= 11.3
40Ar/36Ar INTERCEPT= 207 ± 138
a
36Ar/40Ar
39Ar/40Ar
b
K/Ca
40.73 ± 0.48 Ma
MSWD= 0.80; P= 45%
Age (Ma)
Cumulative 39Ar released (%)
25B (gm-basanite-Marosticano)
c
No isochron age
36Ar/40Ar
39Ar/40Ar
d
K/Ca
No plateau age
Age (Ma)
Cumulative 39Ar released (%)

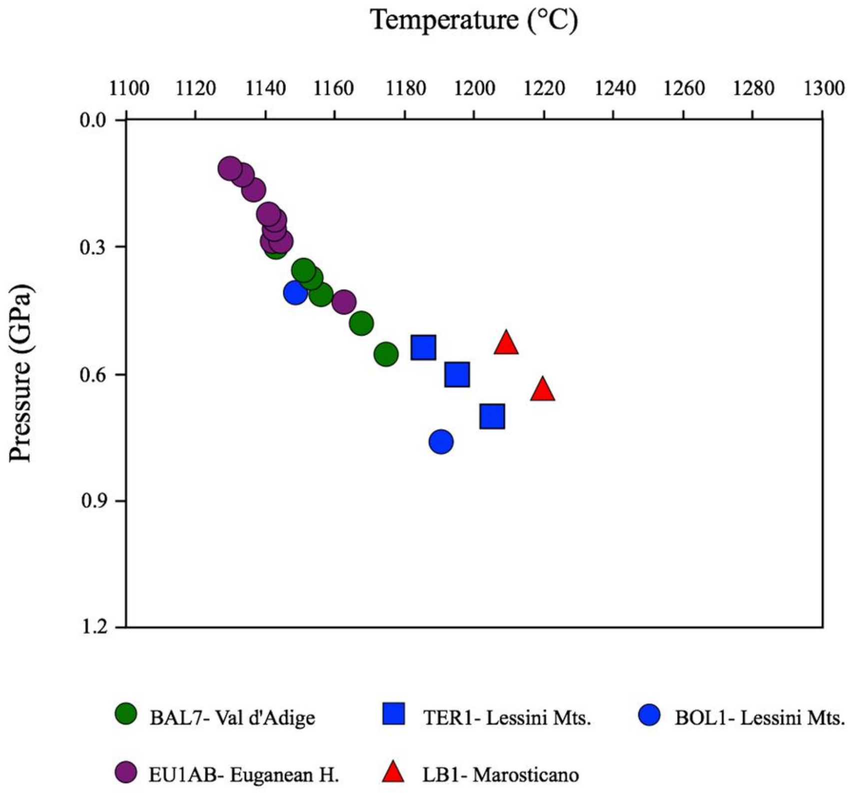

Temperature (°C)
1100
1120
1140
1160
1180
1200
1220
1240
1260
1280
1300
Pressure (GPa)
0.0
0.3
0.6
0.9
1.2
BAL7- Val d'Adige
TER1- Lessini Mts.
BOL1- Lessini Mts.
EU1AB- Euganean H.
LB1- Marosticano

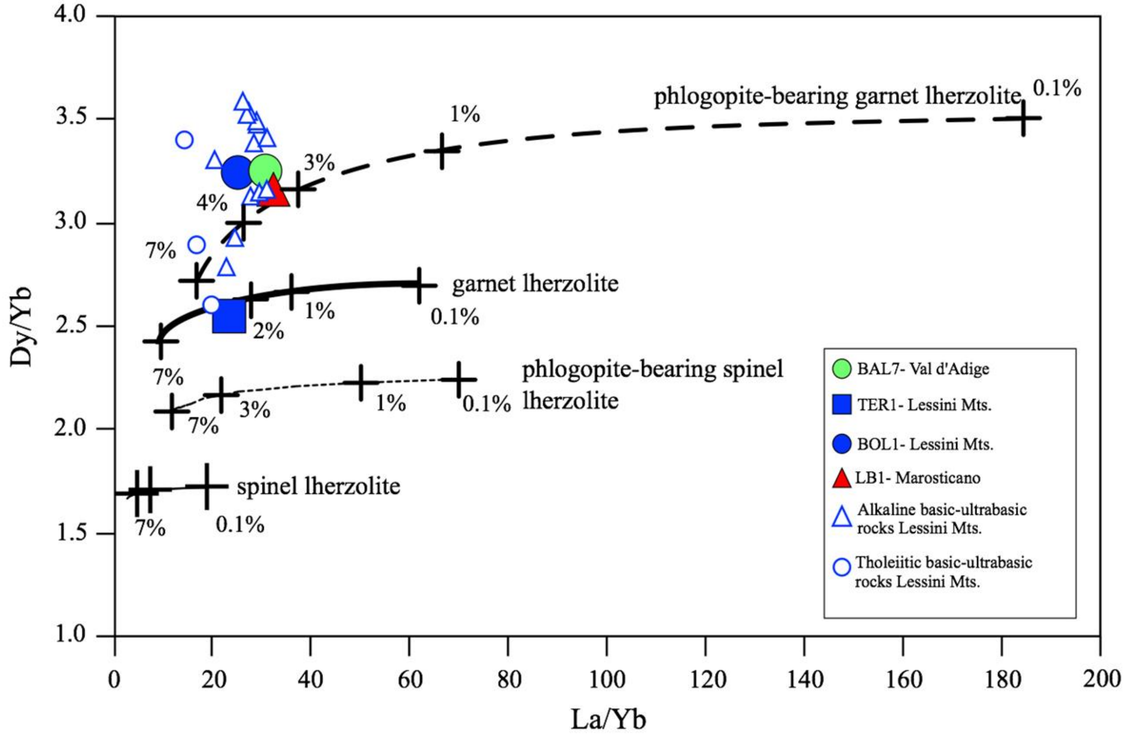

4.0
3.5
3.0
2.5
2.0
1.5
1.0
Dy/Yb
0
20
40
60
80
100
120
140
160
180
200
La/Yb
phlogopite-bearing garnet lherzolite
0.1%
1%
3%
4%
7%
garnet lherzolite
1%
2%
0.1%
7%
phlogopite-bearing spinel lherzolite
7%
3%
1%
0.1%
spinel lherzolite
7%
0.1%
BAL7- Val d'Adige
TER1- Lessini Mts.
BOL1- Lessini Mts.
LB1- Marosticano
Alkaline basic-ultrabasic rocks Lessini Mts.
Tholeiitic basic-ultrabasic rocks Lessini Mts.

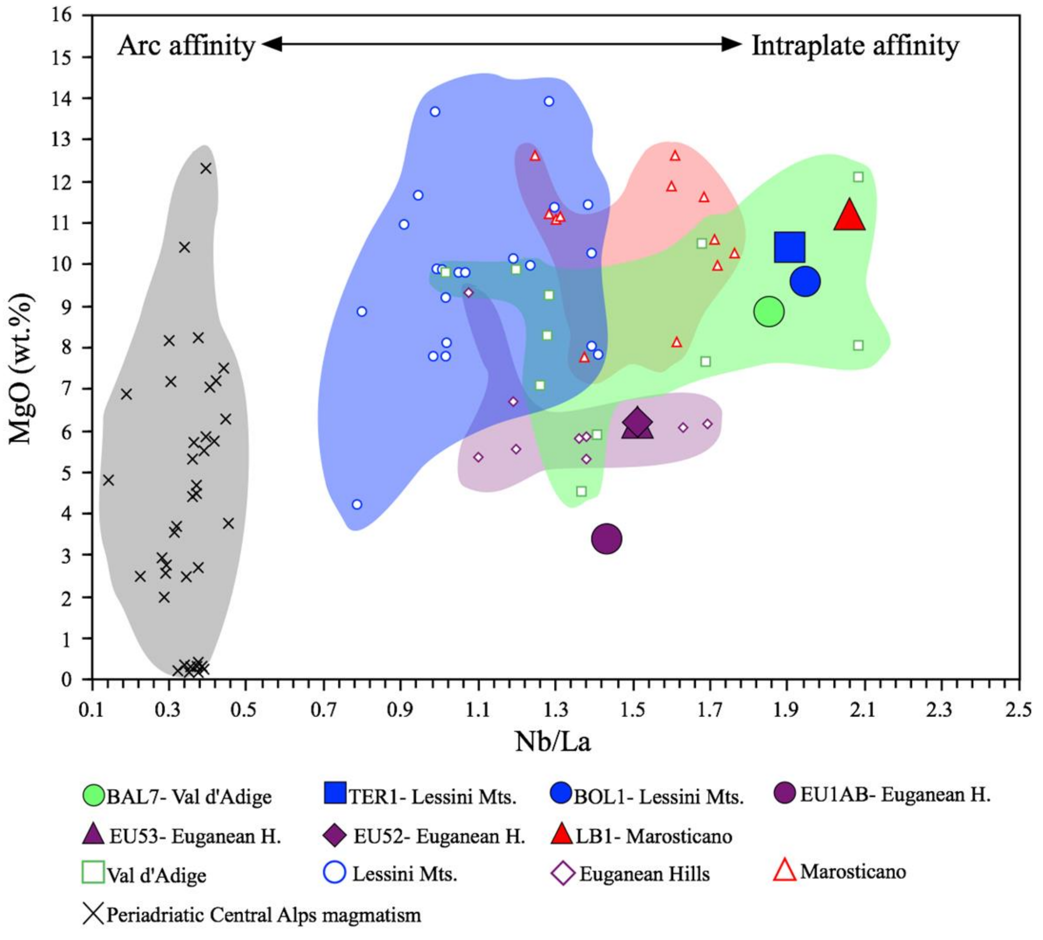

Arc affinity
Intraplate affinity
MgO (wt.%)
Nb/La
BAL7- Val d'Adige
TER1- Lessini Mts.
BOL1- Lessini Mts.
EU1AB- Euganean H.
EU53- Euganean H.
EU52- Euganean H.
LB1- Marosticano
Val d'Adige
Lessini Mts.
Euganean Hills
Marosticano
Periadriatic Central Alps magmatism

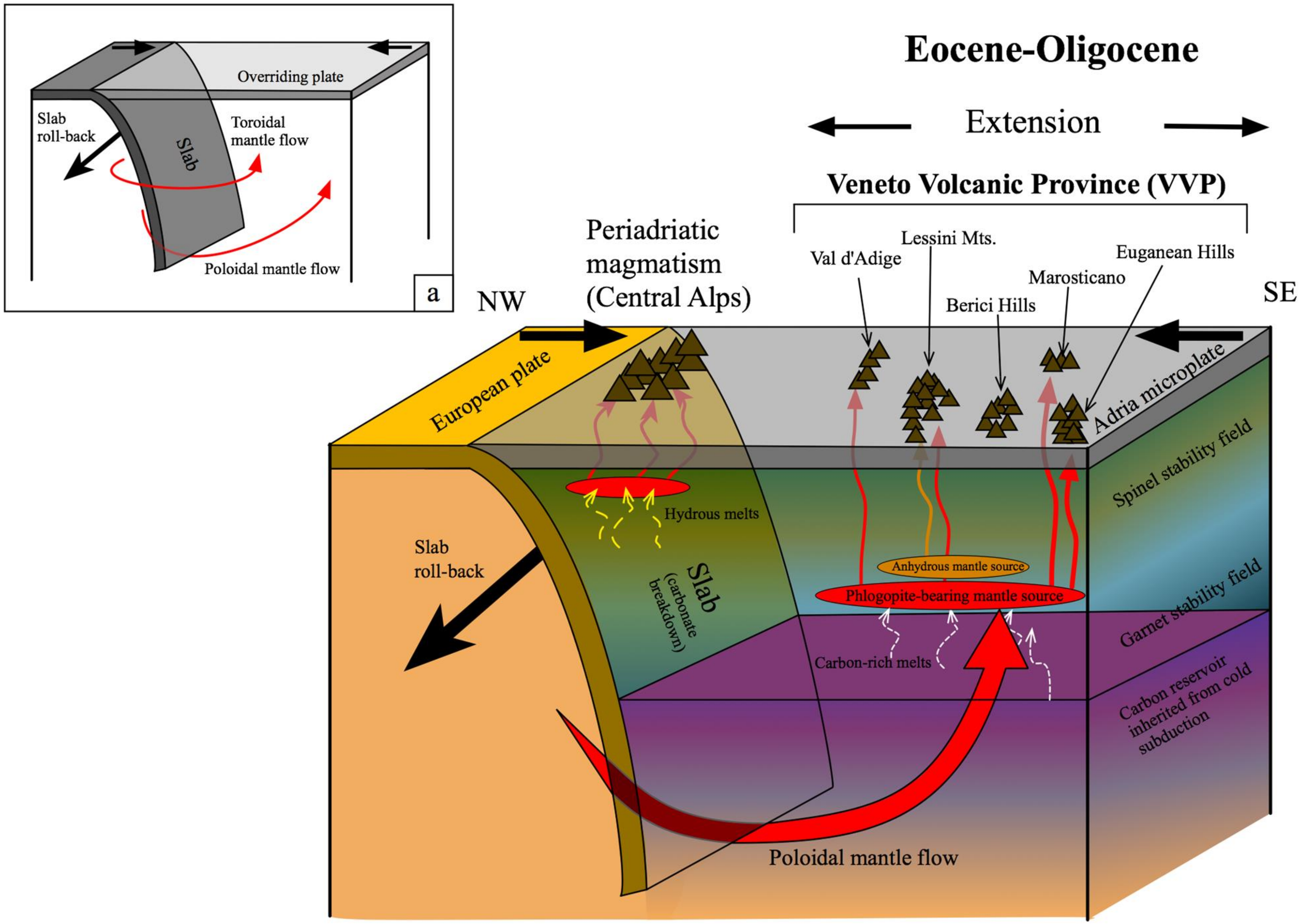

Overriding plate
Slab roll-back
Toroidal mantle flow
Slab
Poloidal mantle flow
a
Eocene-Oligocene
Extension
Veneto Volcanic Province (VVP)
Periadriatic magmatism (Central Alps)
Lessini Mts.
Val d'Adige
Euganean Hills
Marosticano
Berici Hills
NW
SE
European plate
Adria microplate
Hydrous melts
Slab roll-back
Slab (carbonate breakdown)
Spinel stability field
Anhydrous mantle source
Phlogopite-bearing mantle source
Garnet stability field
Carbon-rich melts
Carbon reservoir inherited from cold subduction
Poloidal mantle flow

SUPPLEMENTARY MATERIAL

Intraplate magmatism at a convergent plate boundary, the case of the Cenozoic northern Adria magmatism

Valentina Brombin[a], Costanza Bonadiman[a]*, Fred Jourdan[b], Guido Roghi[c], Massimo Coltorti[a], Laura E. Webb[d], Sara Callegaro[e], Giuliano Bellieni[f], Giampaolo De Vecchi[f], Roberto Sedea[f] Andrea Marzoli[c,f]

[a] *Dipartimento di Fisica e Scienze della Terra, Università di Ferrara, Italy*

[b] *Western Australian Argon Isotope Facility, School of Earth and Planetary Sciences & JdL Centre, Curtin University, Perth, Western Australia, Australia;*

[c] *Istituto di Geoscienze e Georisorse, CNR, Padova, Italy*

[d] *Department of Geology, University of Vermont, Vermont, USA;*

[e] *Centre for Earth Evolution and Dynamics, University of Oslo, Norway;*

[f] *Dipartimento di Geoscienze, Università di Padova, Italy*

S1. ANALYTICAL METHODS

S1.1. Major and trace elements

Whole-rock major and trace elements of samples BAL1, BAL7, BI14, TER1, BOL1, LB1, and 25B were determined by Wavelength Dispersive X-Ray Fluorescence Spectrometry (WDXRF) on pressed powder pellets at the Department of Physics and Earth Sciences, University of Ferrara (Italy), using an ARL Advant-XP spectrometer, following the full matrix correction method proposed by Lachance and Traill (1966). Accuracy is generally lower than 2% for major oxides and less than 5% for trace element determinations, whereas the detection limits for trace elements range from 1 to 2 ppm. Volatile contents were determined as loss on ignition (LOI) at 1000 °C.

Whole-rock major and trace elements of samples EU1AB, EU53, EU52, EU8B, EU13A, EU4, EU5B, and EU9, were determined by X-Ray Fluorescence Spectrometry (XRF) on glass bead samples at the Department of Geosciences, University of Padova (Italy), using Phillips PW1404. Analytical uncertainty ranges from 1 to 2% for major elements and from 10 to 15% for trace elements. LOI was measured at 1000 °C. In addition, Rb, Sr, Y, Zr, Nb, Hf, Ta, Th, U, and Rare Earth elements (REEs) of samples BAL7, TER1, BOL1 and LB1 were determined by Inductively Coupled Plasma–Mass Spectrometry (ICP-MS) using a Thermo Series X-I spectrometer at Department of Physics and Earth Sciences, University of Ferrara. Accuracy and detection limits were determined using several international reference standards, as well as internal standards run as unknowns. Same analyses for samples EU4, EU9, EU8B, EU13A, and EU52 were performed using a Thermo Element2 HR-ICP-MS at University of Bretagne Occidentale, Brest (France), after a repeated HF-$HClO_4$ digestion and HNO_3 dilutions (see Li and Lee, 2006 for details). The repeated analysis of the international standards BCR-2 and BIR-1 demonstrated an external reproducibility better than 5–10 % depending on the element and concentration.

Clinopyroxene compositions of samples BAL7, TER1, BOL1, EU1AB, and LB1 were determined *in-situ* by means of a CAMECA SX50 electron microprobe (EMP) at the IGG–CNR of Padova. using ZAF on-line data reduction and matrix correction procedures.

S1.2. Analytical procedure for $^{40}Ar/^{39}Ar$ radio-isotopic dating

Basanitic and basaltic samples from Val d'Adige, Lessini Mts., and Marosticano districts (BAL1, BAL7, BOL1, TER1, LB1, BI14, and 25B) lack K-rich minerals suitable for geochronology, therefore $^{40}Ar/^{39}Ar$ analyses were performed on groundmass. The sample fraction (30-40 g) was crushed with a rigorously cleaned steel hydraulic press, sieved to a size fraction of 90-250 μm and rinsed in distilled H_2O to remove any dust or powder. In order to collect only the sample grains constituted by the groundmass, the sample fraction was handpicked under a binocular microscope to remove any phenocrysts (pyroxene and olivine). However, due to the dark color of these grains it was impossible to clearly observe if inclusions were present, and therefore exclude the possibility of alteration. The grains were leached in dilute HF in order to remove at least the alteration phases along the surface and cracks. Samples were then rinsed in distilled H_2O in an ultrasonic cleaner.

As basaltic trachyandesites (EU52, EU8B), latite (EU13A), trachyte (EU4), and rhyolites (EU5B, EU9) from the Euganean district are characterized by phenocrysts that are good candidates for $^{40}Ar/^{39}Ar$ dating, *i.e.*, plagioclase and amphibole in the most basic sample, and biotite, sanidine, or feldspar in the more acid samples, $^{40}Ar/^{39}Ar$ analyses were performed on mineral separates. The sample fraction (>1kg) was crushed with a rigorously cleaned steel hydraulic press, sieved to size fractions of 150-215 μm and 215-315 μm, and rinsed in distilled H_2O to remove any dust or powder. Phenocrysts were separated from these fractions using a Frantz isodynamic magnetic separator and were hand-picked grain-by-grain under the binocular stereomicroscope. Mineralic separates were further leached using diluted HF (2N) for 5 minutes to remove any potential adhering alteration product within superficial cracks that were not removed during hand picking (Jourdan et al., 2009b) and then were rinsed in distilled H_2O in an ultrasonic cleaner.

The Ar isotopic ratios were measured through laser step-heating with i) ARGUS VI (samples BAL1, BAL7, BOL1, TER1, EU52, and EU52) and ii) MAP 215–50 (samples EU4, EU5B, EU8B, and EU13A) mass spectrometers at Curtin University within the Western Australian Argon Isotope Facility (WAAIF) of the John de Laeter Centre and iii) Nu Instruments Noblesse magnetic sector noble gas mass spectrometer (samples BI14 and 25B) at the Noble Gas Lab of the University of Vermont. Irrespective to the instrument used for the analyses, our criteria for the determination of plateau are as follows. Plateaus must include at least 70% of ^{39}Ar. The plateau should be distributed over a minimum of 3 consecutive steps agreeing at 95% confidence level and satisfying a probability of fit (P) of at least 0.05. Plateau ages at the 2σ. All the plateau ages are calculated using the mean of all the plateau steps, each weighted by the inverse variance of their individual analytical error. Mini-plateaus are defined similarly except that they include between 50% and 70% of ^{39}Ar. Inverse isochrons include the maximum number of steps with a probability of fit ≥ 0.05. All sources of uncertainties are included in the calculation.

The sample irradiations and the analytical procedures performed are reported in detail below.

S1.3. Sample irradiation and analyses for samples analysed with ARGUS VI mass spectrometer

The cleaned groundmass (BAL1, BAL7, TER1, BOL1, LB1) and mineral separates (EU52) were loaded into several 1.9 cm in diameter by 0.3 cm depth aluminum discs. The discs were then stacked together and placed in quartz tubes. The discs hosting the groundmass included also GA1550 biotite, while the discs hosting plagioclase and amphibole included FCs. GA1550 and FCs were used as neutron fluence monitors, adopting an age of 99.738 ± 0.100 Ma and 28.294 ± 0.036 Ma (1σ), respectively (Renne et al., 2011). The discs were Cd-shielded (to minimize undesirable nuclear interference reactions) and irradiated for 3 hours at the TRIGA Reactor at Oregon State University (USA) The mean J-values computed from standard grains within the small pits range from 0.0008098 (± 0.07%) to 0.0008121 (± 0.11%) for groundmass sample and yielded values of 0.0008098 (± 0.07%) and 0.0008121 (± 0.13%) for the plagioclase and hornblende samples, respectively. For all the samples, the mass discrimination was monitored regularly through the analysis using an automated air pipette and provided the mean value is 0.993485 (±0.02%) per dalton (atomic mass unit) relative to an air ratio of 298.56 ± 0.31 (Lee et al., 2006). The correction factors for interfering isotopes were $(^{39}Ar/^{37}Ar)_{Ca} = 6.95 \times 10^{-4}$ (± 1.3 %), $(^{36}Ar/^{37}Ar)_{Ca} = 2.65 \times 10^{-4}$ (± 0.84 %) and $(^{40}Ar/^{39}Ar)_{K} = 7.30 \times 10^{-4}$ (± 12.4 % ; Renne et al., 2013). At the WAAIF plagioclase, amphibole crystal and groundmass populations were step-heated using a continuous 100 W PhotonMachine© CO_2 (IR, 10.4 µm) laser fired on the crystals during 60 seconds. Each of the standard crystals was fused in a single step.

The gas was purified in an extra low-volume stainless steel extraction line of 240cc and using one SAES AP10 and one GP50 getter. Ar isotopes were measured in static mode using a low volume (600 cc) ARGUS VI mass spectrometer from Thermofisher© set with a permanent resolution of ~200.

Measurements were carried out in multi-collection mode using four faradays to measure mass 40 to 37 and a 0-background compact discrete dynode ion counter to measure mass 36. We measured the relative abundance of each mass simultaneously using 10 cycles of peak-hopping and 33 seconds of integration time for each mass. Detectors were calibrated to each other electronically and using Air shot beam signals. The raw data were processed using the ArArCALC software (Koppers, 2002) and the ages have been calculated using the decay constants recommended by Renne et al. (2011). Blanks were monitored every 2 steps.

S1.4. Sample irradiation and analyses for samples analysed with MAP 215-50 mass spectrometer

Euganean mineral separates (EU8B, EU13A, EU4, EU5B, EU9) were loaded into five large wells of two 1.9 cm diameter by 0.3 cm depth aluminum discs. In one disc the wells were bracketed by small pits that included GA1550 biotite, while in the other disc, the wells were bracketed by seven pits that included Fish Canyon sanidine (FCs). GA1550 and FCs were used as neutron fluence monitors, adopting an age of 99.738 ± 0.100 Ma and 28.294 ± 0.036 Ma (1σ), respectively (Renne et al., 2011). The discs were Cadmium-shielded (to minimize undesirable nuclear interference reactions) and irradiated for 3 hours in the US Geological Survey nuclear reactor (Denver, USA) in central position. The mean J-values computed from standard grains within the small pits is 0.000661 ± 0.00000099 (0.15%) determined as the average and standard deviation of J-values of the small wells for each irradiation disc. Mass discrimination was monitored using an automated air pipette and provided a mean value ranging from 1.006254 ± 0.00030188 (0.03%) to 1.006589 ± 0.00030198 (0.03%) per dalton (atomic mass unit) relative to an air ratio of 298.56 ± 0.31 (Lee et al., 2006). The correction factors for interfering isotopes were $(^{39}Ar/^{37}Ar)_{Ca} = 7.30 \times 10^{-4}$ (± 11%), $(^{36}Ar/^{37}Ar)_{Ca} = 2.82 \times 10^{-4}$ (± 1%), and $(^{40}Ar/^{39}Ar)_{K} = 6.76 \times 10^{-4}$ (± 32%). At the WAAIF the samples were step-heated using a 110 W Spectron Laser Systems, with a continuous Nd-YAG (IR; 1064 nm) laser rastered over the sample during 1 minute to ensure an homogenously distributed temperature. The gas was purified in a stainless steel extraction line using two SAES AP10 getters, a GP50 getter and a liquid nitrogen condensation trap. Ar isotopes were measured in static mode using a MAP 215-50 mass spectrometer (resolution of ~500; sensitivity of $4x10^{-14}$ mol/V) with a Balzers SEV 217 electron multiplier mostly using 9 to 10 cycles of peak-hopping. The data acquisition was performed with the Argus program written by M.O. McWilliams and ran under a LabView environment. The raw data were processed using the ArArCALC software (Koppers, 2002) and the ages have been calculated using the decay constants recommended by Renne et al. (2010). Blanks were monitored every 3 to 4 steps and typical ^{40}Ar blanks range from 1×10^{-16} to 2×10^{-16} mol.

S1.5. Sample irradiation and analyses for samples analysed with Nu Instruments Noblesse magnetic sector noble gas mass spectrometer

The cleaned groundmass were loaded into aluminum foil packets, arranged in suprasil vial, and placed in an aluminum canister for irradiation. Samples were irradiated with multigrain aliquots of FCs to act as a flux monitor (age: 28.03 Ma; Renne et al., 1998) to monitor the neutron dose, and CaF_2 and KSO_4 were also irradiated to determine corrections for interfering nuclear reactions. Samples were irradiated for four hours at the Cd-Lined In-Core Irradiation Tube (CLICIT) reactor of Oregon State University, USA. Correction factors used to account for interfering nuclear reactions for the irradiated samples are: $(^{40}Ar/^{39}Ar)_K = 8.87 \times 10^{-3} \pm 5.30 \times 10^{-3}$, $(^{36}Ar/^{37}Ar)_{Ca} = 2.7 \times 10^{-4} \pm 0.2 \times 10^{-4}$, $(^{39}Ar/^{37}Ar)_{Ca} = 6.7 x 10^{-4} \pm 0.2 \times 10^{-4}$. At the Noble Gas Lab of the University of Vermont, laser step heating for $^{40}Ar/^{39}Ar$ dating was conducted with a Santa Cruz Laser Microfurnace 75 W diode laser system. Flux monitors were loaded into degassed Nb foil packets before being loaded in the wells of the copper planchette sample holder. The volcanic samples were loaded directly into wells of the copper planchette. The gas released during heating was purified with SAES getters and argon isotopes were analysed on a Nu Instruments Noblesse magnetic sector noble gas mass spectrometer during step-heating analyses. Data from samples and flux monitors were corrected for blanks, mass discrimination, atmospheric argon, neutron-induced interfering isotopes, and the decay of ^{37}Ar and

^{39}Ar. Mass discrimination was calculated by analyzing known aliquots of atmospheric argon for which the measured $^{40}Ar/^{36}Ar$ was compared with an assumed atmospheric value of 298.56 ± 0.31 (Lee et al., 2006). A linear interpolation was used to calculate J factors for samples based on sample position between flux monitor packets in the irradiation tube. All ages were calculated using the isotope decay constants recommended by Steiger and Jäger (1977). The age calculations for inverse isochron and apparent age data were achieved using both an in-house data reduction program and Isoplot 3.0 (Ludwig, 2003).

S2. RESULTS FROM $^{40}Ar/^{39}Ar$ GEOCHRONOLOGICAL ANALYSES

All ages obtained and here reported correspond to plateau ages corrected for deviations from the atmospheric $^{40}Ar/^{36}Ar$ ratio of 298.56 ± 0.31 (Lee et al., 2006). For most samples, the $^{40}Ar/^{36}Ar$ ratios are above or below the atmospheric values. Supra-atmospheric values can be explained by the presence of excess ^{40}Ar (*e.g.*, Oostingh et al., 2017), whereas the sub-atmospheric values are indicative of fluid circulation and alteration. In fact ^{36}Ar concentrations are extremely low in mantle derived magmas and fluids, therefore $^{40}Ar/^{36}Ar$ ratio of a predominantly magmatic fluid is sensitive to trace additions of hydrothermal fluids (Burnard and Polya, 2004). For these reasons, in this study ages from samples with low $^{40}Ar/^{36}Ar$ ratios have been considered as only minimum ages.

The basalt BAL1 from Val d'Adige shows an inverse isochron age of 41.70 ± 0.82 Ma [mean square weighted deviation (MSWD) = 0.78; probability (P) = 69%; Table 3; Fig. 5a]. The measured intercept of the inverse isochron indicates an initial $^{40}Ar/^{36}Ar$ value of 266 ± 23, which is slightly below the atmospheric value (298.56 ± 0.31; Lee et al., 2006). Using the $^{40}Ar/^{36}Ar$ intercept value, we calculated a plateau age of 41.69 ± 0.37 Ma (MSWD = 0.39; P = 98%; Table 3; Fig. 5b) based on 75% of the total gas. From the same district, the basanite BAL7 yielded an inverse isochron age of 41.95 ± 0.46 Ma (MSWD = 0.82; P = 64; Table 3; Fig. 5c). Like the previous sample, the $^{40}Ar/^{36}Ar$ intercept value is sub-atmospheric (264 ± 15 Ma); this allows calculate a mini-plateau age of 41.98 ± 0.20 Ma (MSWD = 0.25; P = 100%), including 60% of the released ^{39}Ar (Table 3; Fig. 5d). Both in BAL1 and

BAL7, the K/Ca spectra show typical trends observed for basaltic rock fragments with relatively high values (0.20-0.55) at the low temperature steps that decrease steadily (0.10 to 0.00) towards higher temperature steps, indicating that the K-rich phases degassed predominantly at lower temperatures and high Ca/K-phases dominate at higher temperatures (Fig. 5b, d). TER1 and BOL1 are a basalt and a basanite, respectively, analysed for the Lessini Mts. district and yielded different ages. TER 1 yielded an inverse isochron age of 45.21 ± 0.15 Ma (MSWD = 1.00; P = 44%; Table 3; Fig. 5e). The sub-atmospheric $^{40}Ar/^{36}Ar$ (253± 25) defines a mini-plateau age of 45.21 ± 0.11 Ma (MSWD = 0.83; P = 61%) including 57% of the released ^{39}Ar (Table 3; Fig. 5f). In general the K/Ca ratio decrease from 0.75 to 0.01. BOL1 yielded an inverse isochron age of 40.60 ± 1.76 Ma (MSWD = 0.75; P = 74%; Table 3; Fig. 5g). The $^{40}Ar/^{36}Ar$ intercept is 278 ± 19, close to the atmospheric $^{40}Ar/^{36}Ar$ ratio. This sample yielded a mini-plateau age of 38.73 ± 0.44 Ma (MSWD = 0.99; P = 46%) based on 62% of the total gas (Table 3; Fig. 5h). The basanite BOL1 shows the lowest K/Ca (0.27 to 0.007) of all analysed samples (Fig. 5h).

The amphibole separate of basaltic trachyandesite EU52 yielded an inverse isochron age of 32.37 ± 0.12 Ma (MSWD = 0.52; P = 85%; Table 3; Fig. 5i), with $^{40}Ar/^{36}Ar$ intercept (295 ± 14) indistinguishable from atmosphere and yielded a mini-plateau age of 32.35 ± 0.09 Ma (MSWD = 0.48; P = 89%) based on 67% of ^{39}Ar (Table 3; Fig. 5j). The K/Ca spectrum is flat and the values (0.098 to 0.104) are low, as expected for amphibole (Fig. 5j). The plagioclase inverse isochron age of EU52 is 32.16 ± 0.08 Ma (MSWD = 0.65; P = 87%; Table 3; Fig. 5k). The $^{40}Ar/^{36}Ar$ intercept value is 397 ± 19 and may indicate presence of excess ^{40}Ar. Using the latter value we obtained a plateau age of 32.16 ± 0.06 Ma (MSWD = 0.58; P = 93%), based on 99.5% of the gas (Table 3; Fig. 5l). It should however be considered that the low K/Ca makes all steps cluster at very low $^{40}Ar/^{36}Ar$ intercepts. The K/Ca values range from 0.079 to 0.114, consistent with the plagioclase separate analysed (Fig. 5l). The alkali-feldspar separate of basaltic trachyandesite EU8B shows an inverse isochron age of 32.11 ± 0.98 Ma (MSWD = 0.85; P = 61%; Table 3; Fig. 5m). Using its $^{40}Ar/^{36}Ar$ intercept value (305 ± 99) we obtained a plateau age of 32.17 ± 0.32 Ma (MSWD = 0.79; P = 68%;

Table 3; Fig. 5n), defined by 100% of the released ^{39}Ar. The high K/Ca values (10-5478) are consistent with the mineral phase analysed (Fig. 5n). For the feldspar separate of the latite EU13A we obtained an inverse isochron age of 31.96 ± 1.13 (MSWD = 0.52; P = 91%; Table 3; Fig. 5o). The $^{40}Ar/^{36}Ar$ intercept is 349 ± 136 and defines a plateau age of 32.34 ± 0.51 Ma (MSWD = 0.53; P = 91%) that includes 88% of the total ^{39}Ar (Table 3; Fig. 5p). Despite their large uncertainties, the K/Ca values (0.58-12.50) are consistent with the low-Ca plagioclase phase analysed (Fig. 5p). The inverse age for the biotite separate of trachyte EU4 is 31.83 ± 0.50 Ma (MSWD = 0.88; P = 57%; Table 3; Fig. 5q). The $^{40}Ar/^{36}Ar$ intercept is 328 ± 43 and defines a plateau age of 32.09 ± 0.29 Ma (MSWD = 0.97; P = 48%) based on 100% of the total released gas (Table 3; Fig. 5r). The K/Ca spectrum is flat and the high ratios (157-3762) are consistent with the mineral phase analysed (Fig. 5r). The sanidine separate of rhyolite EU5B yielded an inverse isochron age of 31.87± 0.79 Ma (MSWD = 0.86; P = 59%; Table 3; Fig. 5s) with $^{40}Ar/^{36}Ar$ intercept slightly supra-atmospheric (343 ± 58; Fig. 5s). The calculated plateau age is 32.30 ± 0.52 Ma (MSWD = 1.00; P = 45%) defined by 100% of the released ^{39}Ar (Table 3; Fig. 5t). The K/Ca spectrum is flat with typical ratios for sanidine (0.02-2.48) (Fig. 5t). The sanidine separate of rhyolite EU9 shows inverse isochron ages of 32.02 ± 0.67 Ma (MSWD = 0.51; P = 91%; Table 3; Fig. 5u). With the $^{40}Ar/^{36}Ar$ intercept value (315 ± 68) indistinguishable from atmosphere, the calculated plateau age is 32.17 ± 0.27 Ma (MSWD = 0.48; P = 94%; Table 3; Fig. 5v), defined by 100% of the gas released. The K/Ca spectrum is flat and exhibits typical values for the mineral phase analysed (42-2233; Fig. 5v). It is clear that irrespective to the lithology all analysed Euganean samples yielded nearly indistinguishable ages, which allow us to calculate a mean weighted age of 32.21 ± 0.09 Ma.

The basanite from Marosticano district, LB1, it is the most recent aged VVP sample analysed at WAAIF using the ARGUS VI mass spectrometer. It did not return isochron and plateau ages, but almost all the steps indicate apparent ages between 20.5 and 23.2 Ma (Table 3; Fig. 5w, x). The K/Ca diagram shows a monotonically decreasing plot from 1.69 to 0.003 (Fig. 5x).

The samples BI14 and 25B, two basanites from Val d'Adige and Marosticano, respectively, were analysed at the Noble Gas Geochronology Laboratory of the University of Vermont using the Nu Instruments Noblesse magnetic sector noble gas mass spectrometer with the purpose to expand the VVP geochronological dataset. Despite the poor fit of the measured inverse isochrons, the results from these samples are concordant with the Val d'Adige and Marosticano samples analysed at the WAAIF. For the sample BI14 the $^{40}Ar/^{36}Ar$ intercept of the inverse isochron is 207 ± 138 (Table 4; Fig. 6a) defining a mini-plateau age (40.73 ± 0.48 Ma; MSWD = 0.80; Table 4; Fig. 6b) based on 57% of the released ^{39}Ar. The calculated age is similar to BAL1 and BAL7 ages. In the first three steps the K/Ca ranges from 1.8 to 2.3, while in the last steps it decrease from 0.5 to 0.1 (Fig. 6b). As the LB1, also the sample 25B did not provide isochron and plateau ages and the K/Ca decreases (0.06-6.27; Table 4; Fig. 6c, d). In fact, for both Marosticano samples, almost all the steps indicate apparent ages of ~ 22 - 23 Ma.

REFERENCES

Burnard, P.G., Polya, D.A. 2004. Importance of mantle derived fluids during granite associated hydrothermal circulation: He and Ar isotopes of ore minerals from Panasqueira. Geochim. Cosmochim. Acta 68, 1607-1615. https://doi.org/10.1016/j.gca.2003.10.008.

Jourdan, F., Marzoli, A., Bertrand, H., Cirilli, S., Tanner, L.H., Kontak, D.J., McHone, G., Renne, P.R., Bellieni, G., 2009b. $^{40}Ar/^{39}Ar$ ages of CAMP in North America: Implications for the Triassic–Jurassic boundary and the ^{40}K decay constant bias. Lithos 110, 167-18. https://doi.org/10.1016/j.lithos.2008.12.011.

Koppers, A.A.P., 2002. ArArCALC-software for $^{40}Ar/^{39}Ar$ age calculations. Comput. and Geosci. 28, 605–619. https://doi.org/10.1016/S0098-3004(01)00095-4.

Lachance, G.R., Traill, R.J., 1966. Practical solution to the matrix problem in X-ray analysis. Can. J. Spectros. 11, 43-48.

Lee, J.-Y., Marti, K., Severinghaus, J.P., Kawamura, K., Yoo, H.-S., Lee, J.B., Kim, J.S., 2006. A redetermination of the isotopic abundance of atmospheric Ar. Geochim. Cosmochim. Acta 70, 4507-4512. https://doi.org/10.1016/j.gca.2006.06.1563.

Li, Z.-X. A., Lee, C.-T. A., 2006. Geochemical investigation of serpentinized oceanic lithospheric mantle in the Feather River Ophiolite, California: Implications for the re-cycling rate of water by subduction, Chem. Geol. 235, 161–185. https://doi.org/10.1016/j.chemgeo.2006.06.011.

Ludwig, K.R., 2003. Isoplot/EX, rev. 3.00, a Geochronological Toolkit for Microsoft Excel. Berkeley Geochronology Center Special Publication 4, 71 pp.

Oostingh, K.F., Jourdan, F., Matchan, E.L., Phillips, D., 2017. Ar/Ar geochronology reveals rapid change from plume-assisted to stress-dependent volcanism in the Newer Volcanic Province, SE Australia. Geochem. Geophys. 18, 1-25. https://doi.org/10.1002/2016GC006601.

Renne, P. R., Deino, A. L., Hilgen, F. J., Kuiper, K. F., Mark, D. F., Mitchell, W. S., Morgan, L. E., Mundil, R., Smit, J., 2013. Time scales of critical events around the Cretaceous-Paleogene boundary. Science 339, 684-687. https://doi.org/10.1126/science.1230492.

Renne, P.R. Mundil, R. Balco, G., Min, K., Ludwig, K.R., 2010. Joint determination of ^{40}K decay constants and ^{40}Ar*/^{40}K for the Fish Canyon sanidine standard, and improved accuracy for ^{40}Ar/^{39}Ar geochronology. Geochim. Cosmochim. Acta 74, 5349–5367. https://doi.org/10.1016/j.gca.2010.06.017.

Renne, P.R., Balco, G., Ludwig, K.R., Mundil, R., Min, K., 2011. Response to the comment by W.H. Schwarz et al. on "Joint determination of K-40 decay constants and Ar-40*/K-40 for the Fish Canyon sanidine standard, and improved accuracy for Ar-40/Ar-39 geochronology" by PR Renne et al. (2010). Geochim. Cosmochim. Acta 75, 5097-5100. https://doi.org/10.1016/j.gca.2011.06.021.

Renne, P.R., Swisher, C.C., Deino, A.L., Karner, D.,B., Owens, T.L., Depaolo, D.J., 1998. Intercalibration of standards, absolute ages and uncertainties in $^{40}Ar/^{39}Ar$ dating. Chem. Geol. 145, 117–152. https://doi.org/10.1016/S0009-2541(97)00159-9.

Steiger, R.H., Jäger, E. 1977. Subcommission on geochronology: Convention on the use of decay constants in geo- and cosmochronology. Earth Planet. Sci. Lett. 36, 359-362. https://doi.org/10.1016/0012-821X(77)90060-7.